



# Free-Standing Single-Atom Catalyst-Based Electrodes for CO<sub>2</sub> Reduction

M. Nur Hossain<sup>1</sup> · Lei Zhang<sup>1</sup> · Roberto Neagu<sup>1</sup> · Enoch Rassachack<sup>1</sup>

Received: 17 October 2022 / Revised: 29 March 2023 / Accepted: 12 June 2023  
© The Author(s) 2024

## Abstract

Electrochemical CO<sub>2</sub> reduction technology could solve the CO<sub>2</sub>-induced climate warming by electrochemically converting atmospheric CO<sub>2</sub> back into fuel, essentially recycling it and building a low carbon emission economy. However, the electrochemical CO<sub>2</sub> reduction reaction (CO<sub>2</sub>RR) poses a significant challenge due to the highly stable and linear CO<sub>2</sub> molecules, in addition to a proton-coupled multi-electron transfer process. Thus, highly active catalysts, placed on activity bolstering materials, and permeable electrodes are crucial for CO<sub>2</sub>RR. Single-atom catalysts (SACs) have recently garnered increasing interest in the electrocatalysis community due to their potentially high mass efficiency and cost benefits (every atom is an active center, resulting in nearly 100% utilization) and adjustable selectivity (higher uniformity of the active sites compared to nanoparticles). However, preserving the accessibility and activity of the SACs inside the electrode poses major materials development and electrode design challenges. A conventional layered structure SAC electrode typically consists of a gas diffusion layer (GDL), a microporous layer (MPL) and a SAC catalyst layer (SACCL), fabricated by using a powder bonding process. However, this process usually encounters issues such as delamination and instability of SACs due to the weak binder-catalyst-support interface. Conversely, the free-standing SAC electrode design has the potential to overcome these issues by eliminating the GDL, MPL, and need of a binder, in contrast to the powder bonding process. This work first reviews the latest developments in experimental and modeling studies of powdered SAC electrode by the traditional powder bonding process. Next, it examines the development towards the free-standing SAC electrode for high-performance electrochemical reduction of CO<sub>2</sub>. The synthesis-structure-fabrication-performance relationships of SAC-based materials and associated electrodes are analyzed. Furthermore, the article presents future challenges and perspectives for high-performance SAC electrodes for CO<sub>2</sub>RR.

**Keywords** Single-atom catalyst · Free-standing electrodes · Carbon dioxide · Electrochemical reduction

## 1 Introduction

In the context of climate change, CO<sub>2</sub> pollution is global, and electrochemical CO<sub>2</sub> reduction technology offers a promising route for sustainable energy economy and low or zero carbon emissions. Significant technical progress has been made in recent years, demonstrating the commercial feasibility of the technology [1–5]. However, their large-scale application for the production of fuels has been seriously hindered by the lack of efficient and inexpensive electrocatalysts [6]. In just a decade, a new class of catalysts—the

single-atom catalysts (SACs)—have seen an increasing interest in the electrocatalysis community due to the potentially high mass efficiency and cost benefits (every atom is an active center, thus nearly 100% utilization) and the higher uniformity of the active sites based on single atoms compared to nanoparticles. SAC possesses a well-defined and specific atomic structure that can offer high selectivity toward the adsorption/desorption of certain intermediates during the electrochemical reduction of CO<sub>2</sub> [6–10]. Similar to molecular catalysts, SAC builds a conceptual bridge between heterogeneous and homogeneous catalysis and offers an opportunity to design and understand heterogeneous catalysis from a molecular perspective [11, 12]. The superior performance of SAC has been demonstrated for iron, cobalt and nickel atoms isolated as single atoms on nitrogen-doped carbons for oxygen reduction, hydrogen

✉ Lei Zhang  
lei.zhang@nrc-cnrc.gc.ca

<sup>1</sup> Energy, Mining and Environment, National Research Council of Canada, Vancouver, BC V6T 1W5, Canada

evolution and CO<sub>2</sub> reduction reaction [13–15]. Concerning the development of the controlled synthesis design of SACs, significant progress has been made specifically in the development of strategies to achieve ultra-high metal loadings and to precisely control the atomically dispersed species [16, 17]. Table 1 shows recently developed SACs with their synthesis methods and the primary product of CO<sub>2</sub> reduction with their stability. Recently, some research work has shown a greater focus on scalable routes to accelerate commercialization [18, 19]. Tool development for the characterization of SACs has led to state-of-the-art techniques such as aberration-corrected transmission electron microscopy imaging and X-ray absorption fine structure analysis [20, 21], which enable the verification and visualization of the presence of the single-atom as well as the local coordination environment. In addition, the difficulty in experimentally verifying the structures has also generated computational methods mainly based on density functional theory to support hypotheses for the observed reactivity.

While attention has been devoted so far to synthesis design, atomic-level structural and functional studies, little is understood about the relation between the SACs and the macroscopic setting (electrode structure and morphology) [7–9, 22, 23]. Electrodes in the system play a crucial role since CO<sub>2</sub>RR occurs on the gas-liquid-solid triple-phase boundaries on the surface of an electrode where the CO<sub>2</sub> gas, the proton from the aqueous electrolyte solution and the solid catalyst may coexist. Therefore, it is critical to achieving high performance by controlling the structure and morphology of the electrode for high CO<sub>2</sub> mass transfer, boosting high electronic and H<sup>+</sup> conductivity and enabling large active surface area of the atomically dispersed species by architecture engineering designs. A conventional layered structure SAC electrode typically consists of a gas diffusion layer (GDL), a microporous layer (MPL) and a SAC catalyst layer (CL) [24]. The SAC layered structure electrode is usually fabricated by the powder bonding process which increases potential failures of delamination and instability of catalysts due to the weak binder-catalyst-support interface [25]. For example, most attempts to produce SACs have used powder or particle-like carbon supports; hence, polymer binders, such as Nafion, were employed to incorporate them into the catalyst layer. The binder and inactive support particles will, inevitably, cover a fraction of the catalysts' active sites, rendering them inactive. The free-standing electrode design has the potential to overcome these issues, which is one of the motivations for writing this review paper. Here we define the free-standing electrodes as electrodes with an independent, separate component that can be detached from the assembly and still retains its structural integrity and mechanical strength. Therefore, the free-standing electrodes do not need additional GDLs and MPLs, which increase electrode performance and stability by avoiding additional

interfaces, reducing the interface resistance and time-consuming fabrication processes. The free-standing electrode design will increase the overall efficiency by simply exposing more catalytic active sites, facilitating mass transport, charge transfer and electrical conductivity due to the interconnectedness of the structure, and enhancing mechanical stability due to the absence of a weak binder-catalyst-support interface. The challenge, however, is to devise free-standing designs that can efficiently maintain structural integrity and electrical continuity of the electrodes. Currently, the development of free-standing SACs electrodes is still in the early stages for electrochemical reduction of CO<sub>2</sub> [26–29]. Preserving the accessibility and activity of the SACs inside the electrode remains the major materials development and electrode design challenges for the overall device performance improvement. The techniques considered for the development of free-standing SAC electrodes should generate high form factor nano-sized materials with very good control of morphology, continuous porous structure and high utilization, thus opening a path for producing and investigating free-standing electrodes designs. A successful technology should provide a technically simple, scalable and continuous process toward large-scale production of electrodes using SAC, not only for electrochemical CO<sub>2</sub> reduction applications but also for a wide range of electrochemical energy storage and conversion applications—a technical gap also recognized by Mitchell et al. [8]. Figure 1 shows the specific activity of different-sized particles and catalytic performance of various electrodes for CO<sub>2</sub> reduction.

This work reviews the most recent work in the areas of using SACs and their associated electrodes for electrochemical CO<sub>2</sub> reduction applications, namely (1) approaches and strategies to the areas of design, synthesis and structure characterization of SACs; (2) powdered SAC electrode for electrochemical reduction of CO<sub>2</sub>, which includes the fabrication and structure characterization, structure-property relationship and DFT studies of electrochemical reduction of CO<sub>2</sub>; (3) electrode architecture engineering of the free-standing SAC electrode to improve the exposure of the active metal moieties and the mass transfer performance of the electrode. Specifically, this section provides a comprehensive review and analysis of the free-standing SAC synthesis method, support production, electrode chemistry, fabrication and manufacturing process.

## 2 Design, Synthesis and Structure Characterization of SACs

Many nanostructured catalysts have been used for the electrochemical reduction of CO<sub>2</sub>. Their size, shape, surface morphology and surface area play essential roles in catalytic activity, product selectivity and stability [59–64]. Studies

**Table 1** Table of synthesis methods and stability of SAC for the electrochemical reduction of CO<sub>2</sub>. Data are extracted from different sources and thus are with different significant digits

Synthesis approach	Catalyst	Primary precursor to synthesize the catalyst	Primary product	Stability (h)	References
Wet chemistry, pyrolysis	Ag <sub>1</sub> /MnO <sub>2</sub>	MnO <sub>2</sub>	CO	> 9	[30]
Wet chemistry, pyrolysis	Ag <sub>1</sub> /Graphene	[Ag(phen) <sub>2</sub> ]NO <sub>3</sub>	CO	-	[31]
	Ag <sub>2</sub> /Graphene*	{[Ag(NO <sub>3</sub> -O)(phtz- <i>N</i> )] <sub>2</sub> (μ-phtz- <i>N,N'</i> ) <sub>2</sub> }	CO	> 36	
Freeze-drying, pyrolysis	Ni/NG	Ni(NO <sub>3</sub> ) <sub>2</sub> /Graphene Oxide	CO	> 20 (H-cell) > 8 (MEA)	[32]
MOF precursor, wet chemistry, pyrolysis	Ni/NC	Co/Zn bimetallic ZIFs	CO	> 60	[10]
Wet chemistry, pyrolysis	Ni/NCNT	2-methylimidazole	CO	> 30	[33]
MOF precursor, wet chemistry, pyrolysis	Co-N <sub>2</sub>	Co/Zn bimetallic ZIFs	CO	> 60	[34]
Wet chemistry, pyrolysis, etching	Co-N <sub>5</sub> /HNPCS	HNPCS	CO	> 10	[35]
Wet chemistry, pyrolysis	Zn <sup>δ+</sup> -NC	Zn-BTC	CO	> 12	[36]
Wet chemistry	Cu <sub>3</sub> (HHTQ) <sub>2</sub>	HHTQ	CH <sub>3</sub> OH	> 10	[37]
Wet chemistry, pyrolysis, metal etching	Ni@NiNCM	o-phenyldiamine	CO	> 10	[38]
Wet chemistry, pyrolysis	ZnN <sub>x</sub> /C	Zn/Carbon Black mixed powder	CO	> 75	[39]
Wet chemistry, pyrolysis, silica etching	Ni-SA-NC	EMIM-DCA	CO	> 9	[40]
Wet chemistry, pyrolysis	Ni-NCB	Ni/Carbon Black mixed powder	CO	> 20	[41]
Wet chemistry, pyrolysis	Ni-SAC (Pc)	NiPc-CN	CO	> 16	[42]
MOF precursor, wet chemistry, freeze-drying, pyrolysis	Ni(NC)-1	Ni MOFs	CO	> 20	[43]
MOF precursor, wet chemistry, electrospinning, pyrolysis, metal etching	CoSA/HCNFs	Co/Zn bimetallic ZIF-8 in polyacrylonitrile	CO	> 50	[28]
MOF precursor, wet chemistry, electrospinning, pyrolysis, metal etching	CuSA/TCNFs	Cu/Zn bimetallic ZIF-8 in polyacrylonitrile	CH <sub>4</sub> CO	> 50	[44]
Wet chemistry, pyrolysis, metal etching	FeN <sub>5</sub>	Hemin, melamine	CO	> 24	[45]
MOF precursor, wet chemistry, electrospinning, pyrolysis	NiSA/PCFM	Ni/Zn bimetallic ZIF-8 in polyacrylonitrile	CO	> 120	[46]
Wet chemistry, pyrolysis	Ni-N <sub>3</sub> -V	Ni in DPT and cyanuric acid	CO	> 14	[47]
Acid activation, pyrolysis	ACP/S-N-Ni	Activated carbon paper	CO	> 14	[48]
Wet chemistry, pyrolysis, metal etching	Ni H-CPs	Melamine ink	CO	> 40	[49]
MOF precursor, wet chemistry, pyrolysis, chemical vapor deposition	In <sup>δ+</sup> -N <sub>4</sub>	In(acac) <sub>3</sub> @ZIF-8	HCOOH	> 60	[50]
Freeze-drying, metal etching, pyrolysis	Cu-S <sub>1</sub> N <sub>3</sub> /Cu <sub>x</sub>	Cu-N <sub>4</sub>	CO	> 30	[51]
Ball-milling	CdN <sub>4</sub> S <sub>1</sub> /CN	Melamine	CO	> 24	[52]
Wet chemistry, pyrolysis	SA-Zn/MNC	Carbonized Zn acetate dihydrate	CH <sub>4</sub>	> 35	[53]
Wet chemistry	Ag <sub>1</sub> -N <sub>3</sub> /PCNC	Silver trifluoroacetate	CO	> 40	[54]
Wet chemistry, plasma treatment	PA-CuDBC-1	CuDBC	CH <sub>4</sub>	> 50	[55]
Wet chemistry, pyrolysis	NiSA-NGA-900	Melamine, Graphene Oxide	CO	> 6	[56]
Wet chemistry, pyrolysis	Ni-N <sub>4</sub> /C-NH <sub>2</sub>	Ni-doped ZIF-8	CO	> 10	[57]
Wet Chemistry, pyrolysis	Fe-N-G-p	Porous graphene oxide	CO	> 9	[58]

\*Dual-atom catalyst is more efficient in this case, so the single-atom catalyst was not tested for durability

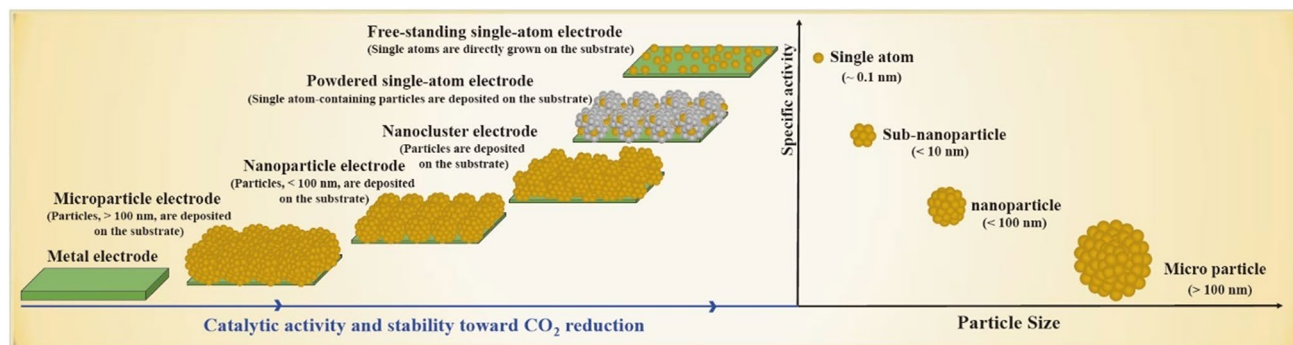


**Fig. 1** Scheme describes the specific activity of different-sized particles and the catalytic performance of various electrodes for CO<sub>2</sub> reduction

show that the active sites of these nanostructured materials ultimately dominate the catalytic performance [64–67]. When the size of the nanostructured catalysts further reduces to the atomic level and disperses on the support surface, it must have a large surface area because of the full catalyst atom utilization, and each atom can act as an active site; hence their catalytic activity and selectivity could dramatically increase [68–70]. Many studies have focused on the development of SACs for the electrolysis of CO<sub>2</sub> in the last decade. Among these, metal catalysts such as Fe, Mn, Ni, Co, Cu, Zn, Ag, Pd and Sn atoms dispersed on carbon support or embedded on metal foil/foam have widely been studied as SACs for electroreduction of CO<sub>2</sub> [49, 71–75]. However, stabilizing the single atom on the substrate surface still remains a challenge because of the formation of atom clusters or nanoclusters by aggregation while further decreasing the size of nanoparticles [21, 76]. The metal single atoms are stabilized by different approaches to obtain active SACs, e.g., pyrolysis of well-mixed metal salts, nitrogen sources and carbon sources at high temperature, deriving metal-organic framework and anchoring metal ions on the defective carbon frame such as graphene [77]. Therefore, different methods have been used for the synthesis of SACs, including physical deposition, electrodeposition, chemical vapor deposition, mechanical ball-milling, photochemical reduction and thermal treatment [20, 78–80].

Transition metal-based nanostructured catalysts, such as Fe, Ni, Co and Cu, have been widely studied for the electrochemical reduction of CO<sub>2</sub> due to their abundance and low cost [81–83]. Recent development has focused on transition metal-based SACs development as they are found to be highly efficient electrocatalysts for CO<sub>2</sub> reduction [70, 77, 84]. Nitrogen-coordinated metal SACs have gained the most attention due to their stable M–N–C bond, and great effort has been employed in the development of such effective nitrogen-coordinated metal SACs [75, 84, 85]. Figure 2 shows various schemes of the synthesis of various metal SACs supported on the carbon matrix. Many useful strategies, including various types of heteroatoms or defects on

carbon substrates, such as pyridine-type N, pyrrole-type N, edge and vacancy defects have been reported as useful anchor sites to stabilize metal single atoms [86–91]. The structure and nature of the carbon matrix play a crucial role in constructing the electronic structure of metal centers, leading to tunable catalytic activity. The fabrication of MN<sub>x</sub>C<sub>y</sub> usually requires a high-temperature treatment process of complex metal and nitrogen precursors as well as carbon-containing precursors such as metal-organic frameworks, functional carbon particles, carbon nanotubes and graphene. A zeolite imidazole framework (ZIF-8) is commonly used as a self-template to synthesize the MN<sub>x</sub>C<sub>y</sub> catalyst with homogeneous dispersion of M atoms in the carbon matrix [87, 92–95]. For example, Fig. 2A shows the synthesis of C-Zn<sub>x</sub>Ni<sub>y</sub> ZIF-8, which is a coordinately unsaturated Ni–N site embedded within porous carbon. The Zn and Ni precursor solutions were mixed with 2-methyl imidazole (2-MeIm) to form Zn<sub>x</sub>Ni<sub>y</sub> ZIF-8, followed by pyrolyzed at 900 to 1 000 °C under Ar to obtain the C-Zn<sub>x</sub>Ni<sub>y</sub> ZIF-8. A wet impregnation process followed by pyrolysis was used to fabricate In SAC in a N-doped carbon matrix (In-SAs/NC) as shown in Fig. 2B. A mixture of a solution containing 2-MeIm, Zn(NO<sub>3</sub>)<sub>2</sub> and In(acac)<sub>3</sub> was used to prepare the In(acac)<sub>3</sub>@ZIF-8, which was heated at 950 °C for 3 h in an inert environment to form the In-SAs/NC. The ZIF-8 precursor was used to encapsulate and prevent the aggregation of In ions, which also provides the platform to form In<sup>δ+</sup>-N<sub>4</sub> atomic interface sites. Figure 2C describes the formation of a F–N–C SAC catalyst with a uniform dispersion of Fe atoms into the carbon phase. The process involves the synthesis of Fe-doped ZnO and growing ZIF-8 crystal simultaneously, followed by pyrolysis at a high temperature in an inert environment. The heat treatment sublimates the ZnO, and Zn acts as spacers to disperse Fe during the pyrolysis process, creating Fe–N–C. The scheme of Fig. 2D illustrates the synthetic process for this Ni SAC catalyst. Activated carbon blacks were homogeneously dispersed in water, followed by the addition of Ni<sup>2+</sup> solution and stirred overnight. Subsequently, it was mixed with a certain amount of urea



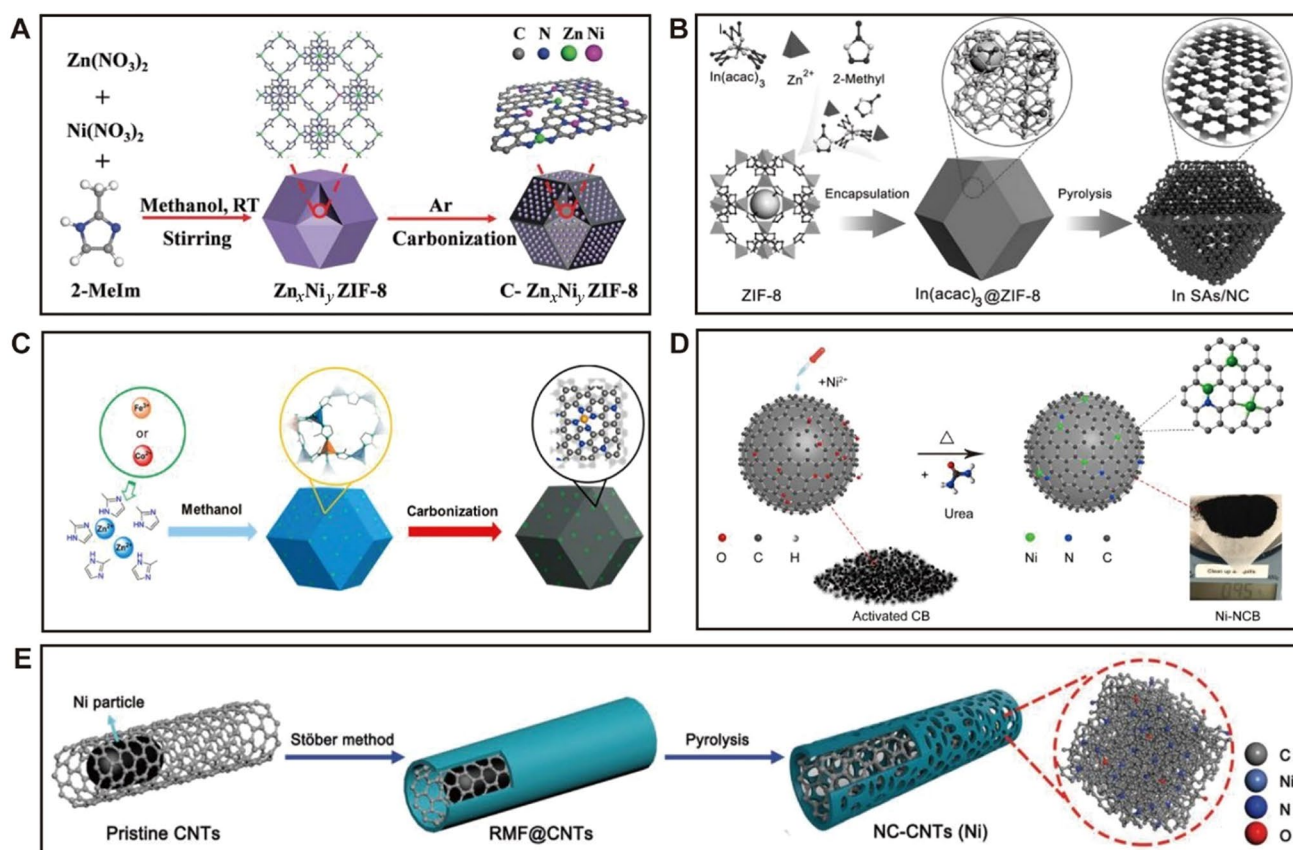


**Fig. 2** The synthesis of different SACs is illustrated schematically as follows: **A** The synthesis of C-Zn<sub>x</sub>Ni<sub>y</sub> ZIF-8 is shown. Reproduced with permission from Ref. [86]. Copyright 2018, Royal Society of Chemistry. **B** The synthesis of In-SAs/NC is demonstrated. Reproduced with permission from Ref. [50]. Copyright 2020, Wiley-VCH. **C** Fe/Co-N-C is illustrated as another SAC. Reproduced with permis-

sion from Ref. [87]. Copyright 2018, American Chemical Society. **D** Ni-NCB is shown as a representative SAC. Reproduced with permission from Ref. [41]. Copyright 2019, Cell Press Publishing group. **E** NC-CNTs is also included in the schematic illustration. Reproduced with permission from Ref. [106]. Copyright 2020, Wiley-VCH

as the N source and annealed at 800 °C in Ar. The activated carbon black has a high adsorption capacity to metal ions due to its large surface area and the presence of defects as well as O-containing functional groups on the surface. Figure 2E shows the synthesis steps of the Ni SAC growing on CNTs. Typically, commercial MWCNTs containing Ni particles were homogeneously dispersed in water and coated with a layer of resorcinol, melamine and formaldehyde. Subsequently, the obtained dried powder was heated at 800 °C for 2 h in an Ar environment.

Structure, morphology, surface area, material density and active sites play critical roles in electrochemical properties. However, the single atoms (SAs) are isolated atoms and their electrochemical properties rely on the distribution throughout the support surface and also on the structure of that support material. Therefore, it is significantly important with the identification of isolated single atoms and confirmation of their distribution. Determining the structure and properties of SACs and identifying their active sites

require many sophisticated characterization tools, such as aberration-corrected high-angle annular dark-field scanning transmission electron microscopy (HAADF-STEM), scanning tunneling microscopy (STM), X-ray absorption spectroscopy (XAS), X-ray absorption near-edge spectroscopy (XANES) and X-ray absorption fine structure spectroscopy (XAFS). Moreover, X-ray photoelectron spectroscopy (XPS) and infrared spectroscopy (IR) are also used to support these sophisticated techniques to characterize SACs. Moreover, the density functional theory (DFT) calculation provides deep insight into the active sites and understanding of the reaction mechanisms. Direct imaging SACs on the support surface using both bright field high-resolution transmission electron microscopy (HR-TEM) and HAADF-STEM modes can be used to verify the formation of isolated atoms [96]. For instance, Pan et al. synthesized Fe-SACs using the Fe-doped ZIF precursor for the electrochemical reduction of CO<sub>2</sub> and identified the isolated catalytic site of Fe-N<sub>4</sub> using HAADF-STEM (Fig. 3A) [87]. The Fe-N<sub>4</sub>

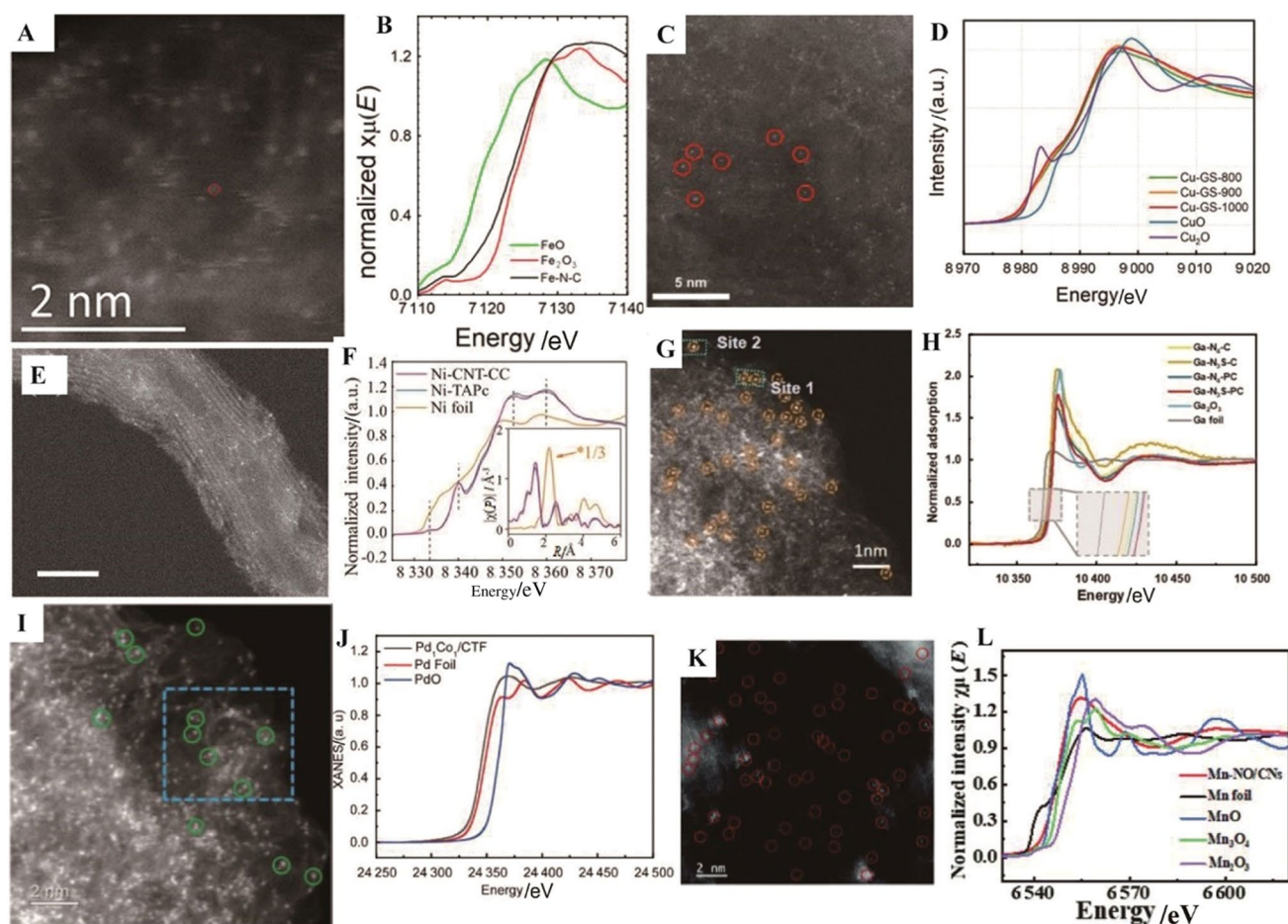


**Fig. 3** Characterization of various metal SACs. Fe-N<sub>4</sub>-C SAC: **A** HAADF-STEM image and **B** X-ray absorption near-edge spectroscopy (XANES) at the Fe K-edge. Reproduced with permission from Ref. [87]. Copyright 2018, American Chemical Society. Cu SAC: **C** HAADF-STEM image and **D** XANES spectra at Cu K-edge for as-synthesized Cu SACs. Reproduced with permission from Ref. [80]. Copyright 2022, Wiley-VCH. Ni-CNT-CC SAC: **E** HAADF-STEM imaging (with a scale bar of 5 nm) and **F** XANES at the Ni K-edge. The inset in (**F**) displays a Fourier transform of the EXAFS spectra.

sites were found to be homogeneously dispersed and embedded throughout the carbon matrix located at the edge sites. Similarly, HAADF-STEM analysis revealed the absence of Cu nanoparticles and the presence of Cu single atoms in a CuN<sub>4-x</sub>-C<sub>x</sub> SAC. The bright spots observed throughout the carbon matrix in Fig. 3C provide evidence for the formation of Cu single atoms [80]. In another study, the formation of Ni SAC on CNTs, developed by Liu and his coworkers for electrochemical reduction of CO<sub>2</sub>, was also initially identified through HAADF-STEM analysis which revealed homogeneously dispersed Ni single atoms with a mean size of 0.2 nm on CNTs (Fig. 3E) [97]. The presence of Ga atoms on Ga SACs was also confirmed by using aberration-corrected HAADF-STEM, which obtained an atomic phase image and

Reproduced with permission from Ref. [97]. Copyright 2020, Wiley-VCH. Ga-N<sub>3</sub>S-PC: **G** Atomic phase image and **H** Ga K-edge XANES spectra (the inset shows the absorption edges for Ga species). Reproduced with permission from Ref. [71]. Copyright 2023, Wiley-VCH. Pd<sub>1</sub>-Co<sub>1</sub>/CTF: **I** AC-STEM image and **J** Pd K-edge XANES spectra. Reproduced with permission from Ref. [72]. Copyright 2023, American Chemical Society. Mn-NO/CNs: **K** HAADF-STEM and **L** Mn K-edge XANES spectra. Reproduced with permission from Ref. [73]. Copyright 2022, Royal Society of Chemistry

highlighted the bright dots corresponding to single-dispersed gallium atoms on the catalyst (Fig. 3G) [71]. The uniform dispersion of Pd and Co atoms on the 2,6-DCP-CTF support at high concentrations in Pd-Co bimetallic SACs was demonstrated through aberration-corrected STEM analysis, which also revealed numerous neighboring dual-dots (Fig. 3I) [72]. Additionally, the presence of a large number of atomically dispersed Mn species in the Mn-NO/CNs catalyst was confirmed through aberration-corrected HAADF-STEM imaging, which displayed numerous isolated bright spots (Fig. 3K) [73]. The local atomic structure and coordination environment of the SACs can be determined by using the XAFS tool as its spectrum is very sensitive to the electronic structure and thereby has been widely used in both

ex situ and in situ atomic structure and coordination environment analysis [28]. To determine the electronic and chemical structure of central metal SACs and quantify electron vacancy, XANES is utilized by analyzing the energy shift and peak intensity of the main X-ray absorption edge [98]. As demonstrated in Fig. 3B, the Fe K-edge XANES spectra verify the bonds of the Fe-SAC, revealing that the oxidation state of Fe-N-C is between +2 and +3, which is comparable to FeO and Fe<sub>2</sub>O<sub>3</sub> standards. The local coordination number further can be determined by analyzing the L-edge XANES. The presence of a splitting peak at 708 eV indicates the octahedral structure of FeO<sub>6</sub> and the absence of splitting peak suggests possible FeN<sub>4</sub> coordination (Fig. 3B). The coordination structure of the Cu SAC was determined through XANES spectra analysis (Fig. 3D), which displayed similar spectra to Cu-N<sub>4</sub>, indicating a coordination number of four for the developed Cu SAC [80]. The Ni K-edge XANES spectra of the Ni SAC embedded on CNTs are presented in Fig. 3F, showing a similarity to that of Ni-TAPc, indicating that Ni has a +2 oxidation state and D4h symmetry structure. Figure 3H displays the XANES spectra of Ga K-edge, which provides information about the oxidation state and coordination environment of the gallium atoms. The inset magnified image in Fig. 3H highlights that the adsorption edge of Ga elements in SACs is close to Ga<sub>2</sub>O<sub>3</sub> with a +3 valence state, pointing out that the oxidation state of the gallium atoms in the SACs is around +3 [71]. Figure 3J shows the Pd K-edge XANES spectra of Pd<sub>1</sub>-Co<sub>1</sub>/CTF, along with corresponding references. The adsorption intensity of Pd in dual-atom Pd<sub>1</sub>-Co<sub>1</sub> was higher than that of Pd foil and similar to that of PdO, demonstrating an average valence state of Pd close to Pd<sup>2+</sup>. The absorption edge position of Co in Pd<sub>1</sub>-Co<sub>1</sub>/CTF was located between CoO and Co<sub>3</sub>O<sub>4</sub>, suggesting that the valence state of Co species ranged between Co<sup>2+</sup> and Co<sup>3+</sup> [72]. XAFS analysis was conducted on Mn-NO/CNs to obtain insights into its coordination environment. The Mn K-edge XANES diagram of Mn-NO/CNs showed a distinct difference from the oxide diagrams of Mn<sub>x</sub>O<sub>y</sub> and Mn foil (Fig. 3L), suggesting that the valence state of Mn in Mn-NO/CNs was greater than zero [73]. Operando XAFS can be used to investigate the dynamic structure of the SACs during the electrochemical reaction and provides a deep understanding of the reaction and working mechanism of active centers [99]. For example, Liu et al. synthesized Ni SAC for CO<sub>2</sub> reduction and performed in situ XAFS during the electrochemical reaction [15]. The CO<sub>2</sub>-saturated KHCO<sub>3</sub> solution shows 0.4 eV higher energy for Ni K-edge of low-valent Ni SACs (A-Ni-NG) compared to Ar-saturated KHCO<sub>3</sub> solution at the open-circuit voltage and it went down to lower energy during the CO<sub>2</sub> electrolysis, indicating the recovery of low-oxidation-state of Ni sites. However, the main peak in FT-EXAFS for Ni-N became longer during CO<sub>2</sub> reduction at the applied potentials of −0.7 V (vs.

RHE), suggesting the larger and distorted Ni–N bond while adsorbing CO<sub>2</sub> on Ni SA sites. According to their operando XAFS and theoretical calculations, the Ni (I) atomic center is monovalent with a d<sup>9</sup> electronic configuration and determined as active sites for the activation of CO<sub>2</sub> molecule and electrochemical reduction.

### 3 Powder-Based SAC Electrode for Electrochemical Reduction of CO<sub>2</sub>

Various materials have been explored as electrodes for CO<sub>2</sub> reduction, e.g., metals, oxides, alloys, metal complexes and carbon-based materials. Their nanostructured materials exhibit higher catalytic performance as they have a large surface area and more active sites. Recently, SACs have drawn wide attention to CO<sub>2</sub> electrolysis and exhibited excellent electrocatalytic performances due to their maximum atomic utilization and having a special electronic structure. Most of these catalysts are in powder form and need to bind to support surfaces to make working electrodes [10, 15, 100]. Various polymer binders, such as nafion, polyvinylidene fluoride, styrene butadiene rubber, sodium carboxymethyl cellulose and others, have been used as binders to attach catalyst powders onto the electrode support surface.

#### 3.1 Fabrication and Structure Characterization of Powder-Based SAC Electrode

Recently, many transition metal-based SACs have been explored as electrocatalysts for CO<sub>2</sub> reduction [70, 77, 84]. Among these developed SACs, nitrogen-anchored metal atom sites (e.g., Fe, Co, Ni etc.) have been found as outstanding catalysts. Various effective methods have been employed for the preparation of these highly efficient SACs-based electrodes. For example, ZIF-8 is commonly used as a self-template to synthesize the F-N-C catalyst with homogeneous dispersion of Fe atoms in the carbon matrix [87, 92–95]. The synthesis process needs the Fe-doped ZnO preparation and growing ZIF-8 crystal simultaneously. Then pyrolysis occurred at a high temperature in the Ar environment, where ZnO sublimed and created Fe-N-C. In another work, Gu et al. have synthesized Fe-SAC with dispersed single-atom Fe sites in ZIF-8 through the pyrolysis of Fe-doped Zn-ZIF-8 at 900 °C under the N<sub>2</sub> environment [92]. The prepared Fe-SAC was porous with an electrochemical double-layer surface area of 554 m<sup>2</sup> g<sup>−1</sup> and a Brunauer-Emmett-Teller surface area of 772 m<sup>2</sup> g<sup>−1</sup>. Its porosity was determined by employing high-angle annular dark-field scanning transmission electron microscopy (HAADF-STEM), as shown in Fig. 4A. The corresponding energy-dispersive X-ray spectroscopy (EDS) and EDS mapping showed the presence of Fe and homogeneous distributions of Fe and N



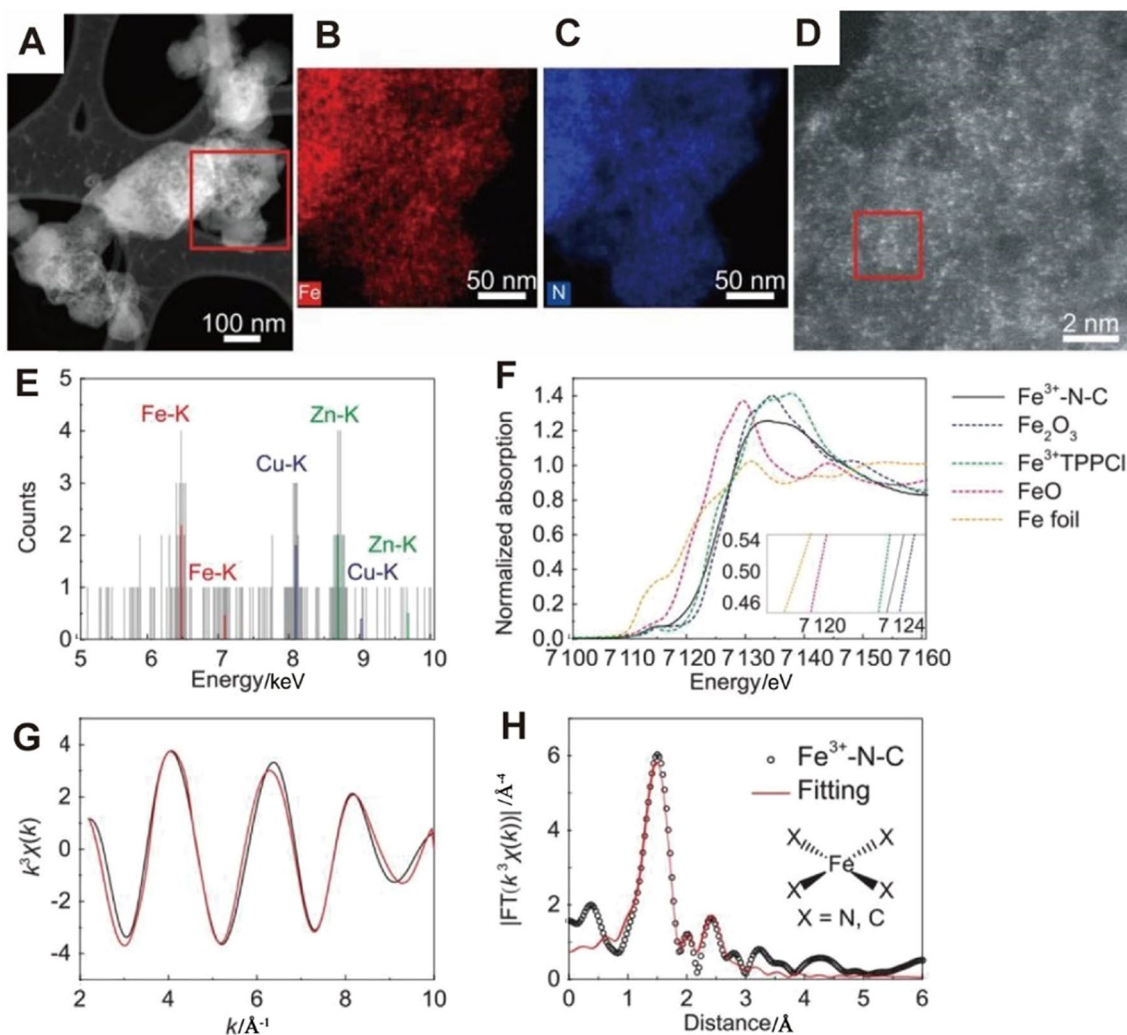


**Fig. 4** Structural characterization of Fe-SAC using various techniques. **A** HAADF-STEM image. **B** and **C** Corresponding EDS mappings of Fe and N in the red square region, respectively. **D** Aberration-corrected HAADF-STEM image. **E** EDS spectrum of the region enclosed by the red square. **F** Fe K-edge XANES spectra of Fe<sup>3+</sup>-N-C (black), Fe<sub>2</sub>O<sub>3</sub> (blue), Fe<sup>3+</sup>TPPCI (green), FeO (pink) and Fe foil

(orange); inset shows the enlargement of the main edges. **G** the  $k$  space Fe K-edge EXAFS spectra. **H** the  $R$  space Fe K-edge EXAFS spectra. The experimental data are shown in black, while the fitting curves are shown in red. Reproduced with permission from Ref. [92]. Copyright 2019, Science Publishing Group

atoms in the carbon matrix, respectively (Fig. 4B, C and E). The aberration-corrected HAADF-STEM image shows the bright spots with the size of  $\sim 0.2$  nm and is uniformly dispersed in the carbon phase corresponding to Fe and Zn sites (Fig. 4D). As seen in Fig. 4F, the binding and edge energies are close to Fe<sub>2</sub>O<sub>3</sub> and Fe<sup>3+</sup>-tetraphenylporphyrin-Cl (Fe<sup>3+</sup>TPPCI) determined by the Fe K-edge X-ray absorption near-edge structure spectrum, suggesting that the Fe ion was in the +3 oxidation state in the synthesized Fe<sup>3+</sup>-N-C. Thus, Fe<sup>3+</sup> was oxidized to Fe<sup>3+</sup> during the pyrolysis and protons, or residual oxygens might be the oxidants that oxidized the carbon backbone of the ZIF-8 precursor. The  $k$  space and  $R$  space Fe K-edge extended X-ray absorption (EXAFS) fine structure confirmed the atomic dispersion of Fe sites

in Fe<sup>3+</sup>-N-C, and the fitting of the spectrum suggested that the Fe center obtains a planar Fe-X<sub>4</sub> (X=N or C) structure (Fig. 4, G and H). Nitrogen-coordinated Fe sites as Fe-N<sub>4</sub> moieties in carbon-containing bulk- and edge-hosted coordination were also fabricated by using a similar synthesis approach reported by Shao's group [95]. In their work, the atomic structure of Fe single atoms and their homogeneous dispersion were determined by using STEM-HAADF. X-ray absorption spectroscopic studies revealed that each Fe atom was coordinated with four N atoms, and the catalyst reserved its original shape. X-ray diffraction patterns revealed that it is partially graphitized carbon, and no metallic phases are observed. Moreover, Raman spectroscopy showed a disordered structure of the carbon phase for the



synthesized Fe-N-C catalyst, which is similar to the N-C catalyst [87]. ZIF was also used as a precursor with other carbon materials, such as porous carbon, carbon nanotubes, graphene and graphene oxide, to synthesize Fe-N-C catalysts for CO<sub>2</sub> reduction [93, 95, 101–103]. Wei and his coworkers developed Fe-N/P-C SAC supported on activated carbon black, showing that the Fe atom coordinated with both N and P atoms acted as an active site and uniformly dispersed throughout the carbon substrate [102]. Their synthesis steps involved a two-stage pyrolysis process at 400 and 800 °C in forming Fe-P and Fe-N coordination bonds supported by XRD, X-ray photoelectron spectrometry (XPS), HAADF-STEM and inductive coupled plasma mass spectrometry (ICP-MS) studies. Creating Fe-N and Fe-P bonds together as FeN<sub>3</sub>P moiety in the Fe single-atom catalyst could alter the electronic structure of the Fe atom, which may boost the catalytic activity for CO<sub>2</sub> reduction. A different approach has been used by Chen et al. to synthesize porous carbon nanospheres containing high-density Fe-N-C active sites [105]. SiO<sub>2</sub> was used as a template for developing carbon shells and acted as a microreactor to prevent the aggregation of Fe atoms during the formation of Fe-N-C in the pyrolysis step. Multi-walled carbon nanotubes (MWCNTs) combined with ZIFs were used to prepare Fe-N-C catalyst, where MWCNT could create mesoporosity and increase electrical conductivity for higher mass transport and reduce the overpotential for the reduction of CO<sub>2</sub> to CO [95]. ZIF and MWCNTs were mixed with Zn and Fe precursors in methanol, and the obtained ZIF-Fe-CNT was pyrolyzed at 900 °C under the Ar. TEM analysis revealed that the networks of MWCNTs in ZIF-Fe-CNT covered by Fe-N-C and carboxylates on the MWCNTs induce site-specific nucleation. Pan et al. have used commercial MWCNTs to fabricate FeN<sub>4</sub> sites anchored on CNT and graphene nanoribbon networks (Fe-N/CNT@GNR) as an effective electrocatalyst for CO<sub>2</sub> reduction [103]. CNT was oxidized by H<sub>2</sub>O<sub>2</sub> and KMnO<sub>4</sub> mixture followed by pyrolysis at 900 °C in the presence of urea to obtain the atomically dispersed FeN<sub>4</sub> moiety Fe-N/CNT@GNR. The Fe residues present in the commercial MWCNTs served as Fe sources to grow isolated FeN<sub>4</sub> sites, the chemical unzipping incurred by oxidizing the CNT creates graphene nanoribbon (GNR) layers attached to the outer shell-wall of the CNTs and subsequent N doping by the thermal pyrolysis leads to the generation of FeN<sub>4</sub> sites containing Fe-N/CNT@GNR. In the developed structure, the CNTs act as a fibrous backbone to anchor the GNRs, suppress their aggregation and thus reticulate a hierarchically mesoporous structure with a large electrochemical surface area. The monodispersed FeN<sub>4</sub> centers supported on the CNT and GNR basal plane and edge sites in the mesoporous CNT@GNR architecture act as active and selective centers to enhance CO<sub>2</sub> activation and suppress hydrogen evolution reaction. Graphene has also been taken into consideration to deposit SAC due

to its unique electronic and physical properties. The FeN<sub>5</sub> SAC was successfully synthesized through the pyrolysis of hemin and melamine molecules on N-doped graphene [93]. The aggregation of Fe atoms on graphene is suppressed due to the formation of cross-linking of hemin and melamine at high temperatures, resulting in the homogeneous dispersion of FeN<sub>5</sub> sites. Moreover, melamine introduces the N-dopant into graphene because it is the main source of N, which is able to anchor the Fe atom to form a unique FeN<sub>5</sub> active site. Furthermore, graphene increases the electrical conductivity, provides a high specific surface area with hierarchical porosity. A facile approach to synthesis Fe-SAC was demonstrated for Fe metal foam by the adsorption graphene oxide (GO) based on the dangling bond trapping method [101]. The Fe-SAC was synthesized by injection GO dispersion slurry into the Fe foam and then drying at room temperature under Ar. Subsequently, the Fe-GO was ultrasonicated in ethanol to separate the adsorbed layers to yield Fe SAs/GO. The oxygen-containing group on the GO surface is strongly attached with Fe atoms of Fe foam due to the charge transfer between Fe and O atoms, resulting in Fe<sup>δ+</sup> (0 < δ < 3) species, which could be an efficient electrocatalyst for CO<sub>2</sub> reduction. HAADF-STEM, EDS elemental mapping and XANES analysis confirmed the uniform dispersion of Fe atoms rather than Fe nanoparticles or clusters on the surface of GO.

Ni nanostructured materials are more highly active for hydrogen evolution reactions than the electrochemical reduction of CO<sub>2</sub> due to the strong CO adsorption [32]. However, its electrochemical properties can significantly be turned into CO<sub>2</sub> reduction application once modified into single atoms, such as the nitrogen-stabilized nickel single-atom matrix (Ni-N). The atomically dispersed Ni-N centers have unique properties compared to corresponding nanostructured and bulk materials. Various Ni-based single-atom catalysts have been successfully developed for electrochemical reduction of CO<sub>2</sub>, typically for CO generation, as they exhibit high faradaic efficiencies [97, 105]. For example, a Ni SAC with coordinatively unsaturated Ni-N active sites fabricated by pyrolyzing Ni-substituted ZIF-8 exhibited Faradaic efficiencies of 92.0%–98.0% for the electrochemical reduction of over a wide potential range [86]. The high-resolution HAADF-STEM image (Fig. 5A) shows the atomic dispersion of nickel species and no existence of Ni nanoparticles in C-ZnNi<sub>4</sub> ZIF-8. The binding energies of the Ni 2p<sub>3/2</sub> peak of the pyrolyzed products are found to be ~855.0 eV, which is greater than that of metallic Ni and lower than that of Ni<sup>2+</sup> in NiPc (Fig. 5B), suggesting that the valence of Ni of pyrolyzed samples is between 0 and +2. Figure 5C and D displays the Ni K-edge XANES and EXAFS of the synthesized C-Zn<sub>x</sub>Ni<sub>y</sub> ZIF-8 and standard Ni foil and NiPc. The Ni absorption edge and main transition energies of C-ZnNi<sub>4</sub> ZIF-8 and other studied materials are

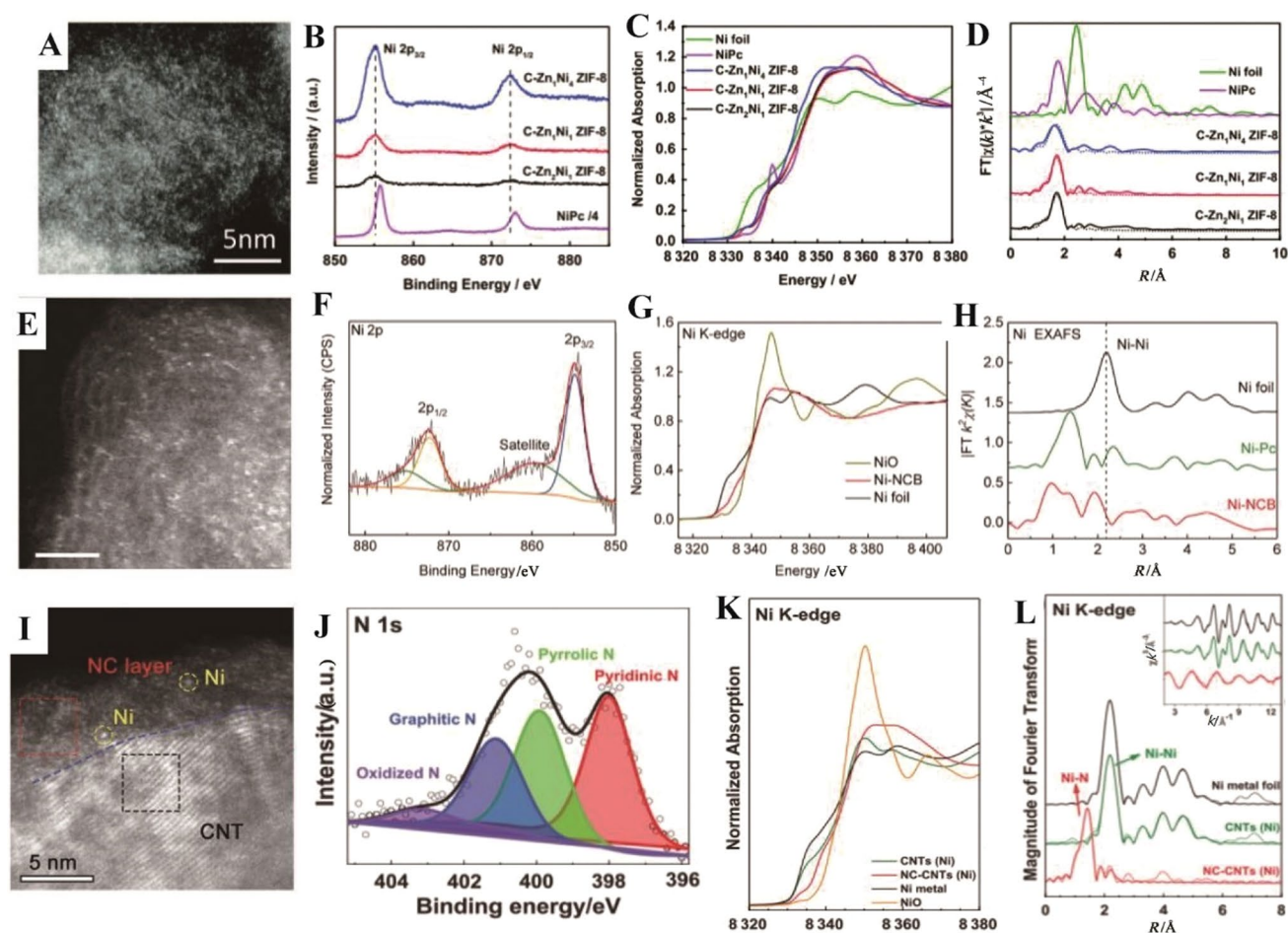


**Fig. 5** Characterization of various samples. For C-ZnNi<sub>4</sub> ZIF-8: a high-magnification HAADF-STEM image (A), Ni 2p high-resolution XPS spectra (B), XANES spectra (C) and Fourier transformed EXAFS spectra of the Ni K-edge and corresponding reference samples (D). The solid line represents experimental data, while the dotted line represents fitting curves. Reproduced with permission from Ref. [86]. Copyright 2018, Royal Society of Chemistry. For Ni-NCB: an aberration-corrected HAADF-STEM image (E) with a scale bar of 2 nm, Ni 2p high-resolution XPS spectra (F), Ni K-edge XANES

spectra (G) and Ni K-edge Fourier transformed EXAFS spectra in R space (H). Reproduced with permission from Ref. [41]. Copyright 2019, Cell Press Publishing group. For NC-CNTs: a high-resolution HAADF-STEM image (I), N 1s high-resolution XPS spectra (J), Ni K-edge XANES spectra (K) and Ni K-edge Fourier transformed EXAFS spectra in the R space of NC-CNTs (Ni) and CNTs in comparison to Ni metal foil (L). An inset is also included, showing the k<sup>2</sup>-weighted EXAFS in k space. Reproduced with permission from Ref. [106]. Copyright 2020, Wiley-VCH

between those of Ni foil and NiPc, indicating an intermediate valence state of Ni. Fourier transformed EXAFS analysis also revealed the presence of Ni–N bonds in the pyrolysis products, indicating that the Ni atoms are atomically dispersed in the samples. The coordination numbers of the Ni atom of the synthesized materials fitted from EXAFS analysis revealed the coordinatively unsaturated state of the Ni species. The 2-MeIm was carbonized and most of the Zn was sublimed during pyrolysis, resulting in coordinated Ni with N atoms anchored into the carbon matrix and thus forming a homogeneously dispersed and coordinatively unsaturated Ni SAC. Another simple and scalable method was used to synthesize Ni SACs supported on commercial carbon black as the efficient electrocatalyst for CO<sub>2</sub> reduction [41]. The

aberration-corrected HAADF-STEM image shows the homogeneously dispersed bright spot of the Ni atom on the entire carbon particles (Fig. 5E). Ni 2p XPS spectra of the synthesized Ni SAC catalysts are displayed in Fig. 5F, demonstrating that the binding energy of Ni 2p<sub>3/2</sub> of the Ni single atom dispersed on carbon black is higher than the Ni<sup>0</sup>, indicating its positive oxidation state. XANES and EXAFS analysis indicated further that the oxidation state of Ni species in synthesized Ni SACs was higher than Ni foil and lower than NiO (Fig. 5G and H). Fan et al. have designed a scalable strategy to grow Ni SACs on CNT by in situ thermal diffusions with NiN<sub>3</sub> moiety from the Ni nanoparticle in CNT [106]. Their developed Ni SAC exhibited a high FE, superb turnover frequencies and a large mass

activity for the conversion of  $\text{CO}_2$  to CO. High-resolution HAADF-STEM shows the isolated Ni atoms as bright spots, indicating the formation of Ni single atoms on the wall of MWCNT (Fig. 5I). Figure 5J displays the XPS of the developed Ni SAC-CNT, showing the presence of N atom and its deconvolution of the high-resolution 1s XPS peak indicating four N configurations including pyridinic, pyrrolic, graphitic and oxidized N. However, there was no Ni XPS peak appeared, which could be the low concentration of Ni on the surface. The EXAFS of Ni K-edge determined the electronic structure of the synthesized Ni SAC-CNT and its chemical configuration (Fig. 5K and L). The Ni edge positions of Ni SAC-CNTs are consistent with those of Ni metal and NiO, suggesting that the average oxidation state of Ni is 0 to 2. A Ni-Ni pair and a Ni-N interaction was identified at 2.15 Å ( $1 \text{ Å} = 1 \times 10^{-10} \text{ m}$ ) and 1.40 Å, respectively. After fitting the EXAFS curves, the coordination number of Ni was found to be between two and three, confirming the formation of Ni single atoms after the treatments.

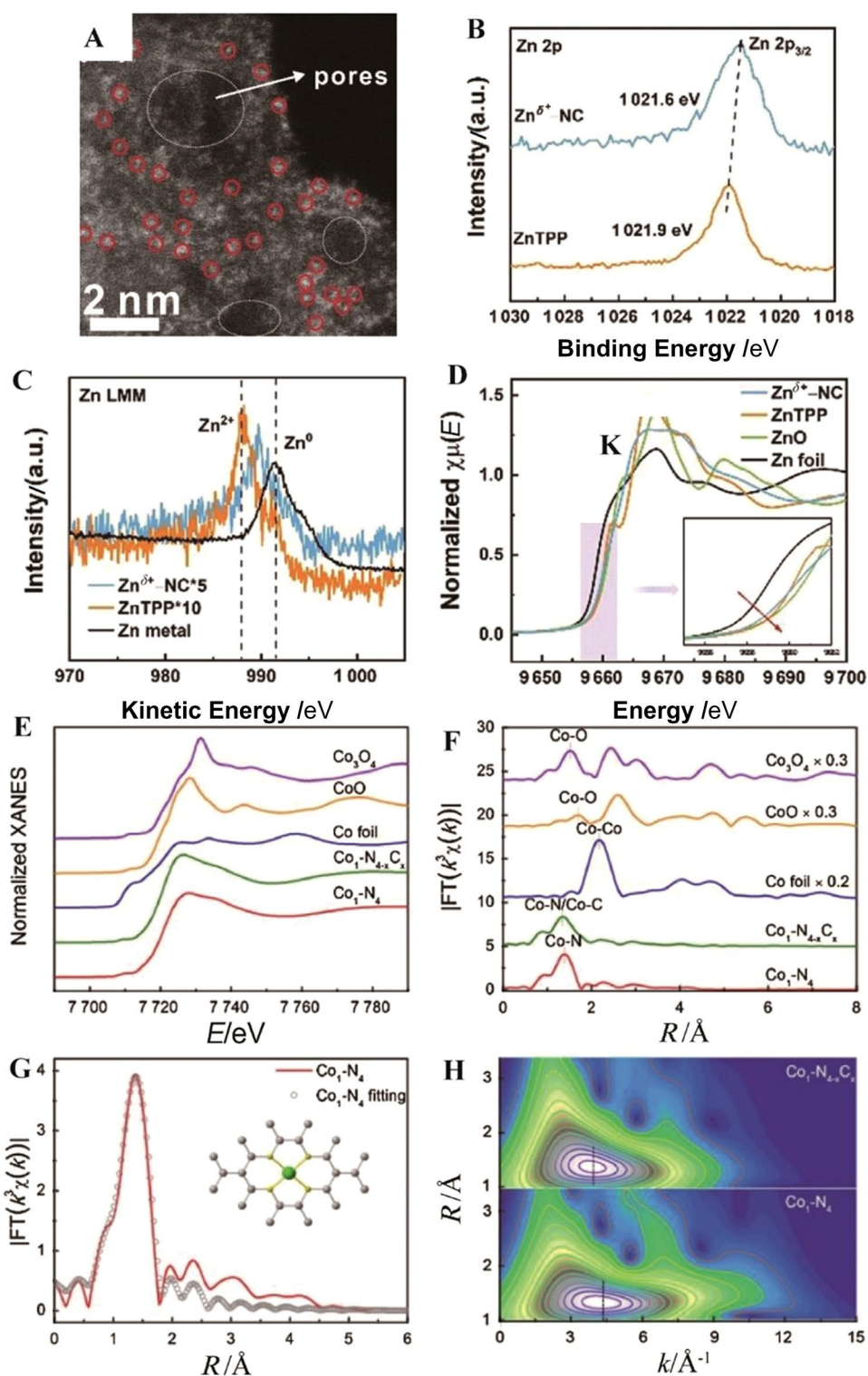
Among various metal SACs (e.g., Fe-NC, Co-NC and Ni-NC), Zn SAC (Zn-NC) has also been studied for  $\text{CO}_2$  electrolysis. However, the number of Zn SACs developed in the literature is much less compared to other transition metal SACs. It is difficult to incorporate Zn atoms into the carbon matrix because Zn has a low boiling point (1 180 K) and easily evaporates during pyrolysis [105]. Therefore, various metal-doped Zn precursors are commonly used as templates to fabricate uniformly dispersed metal atoms in porous carbon structures. As Zn has fully occupied  $3d^{10}$  configuration, the possibility of charge transfer might be low, resulting in the low catalytic activity of the developed Zn SAC. However, some studies still focused on the development of Zn SAC for the electrochemical reduction of  $\text{CO}_2$  and showed a significant improvement. For example, Daasbjerg and his coworkers developed N-containing low-valence Zn-based SACs ( $\text{Zn}^{\delta+}$ -NC) using Zn-containing precursors by pyrolyzing at high temperatures under the nitrogen environment [36]. Figure 6A shows an aberration-corrected HAADF-STEM image of the developed Zn SAC with a homogeneous distribution of bright spots with through-plane pores, indicating the formation of Zn atoms throughout the carbon matrix. XPS was employed to study the chemical composition and oxidation states of the Zn using  $\text{Zn}^{\text{II}}$  tetraphenylporphine (ZnTPP), showing the binding energy of Zn  $2p_{3/2}$  in  $\text{Zn}^{\delta+}$ -NC is 1 021.6 eV, which is lower than that of ZnTPP, indicating a low-valence Zn ( $< +2$ ) (Fig. 6B). A distinct Zn LMM peak was appeared at 990.0 eV of  $\text{Zn}^{\delta+}$ -NC in Zn Auger LMM kinetic energy spectra (Fig. 6C), which is located between ZnTPP (987.8 eV) and Zn metal (992.0 eV), suggesting that the states of Zn higher than 0 and lower than +2. Figure 6D shows the Zn K-edge spectrum taken from XANES with ZnTPP, ZnO and Zn foil serving as references to determine the electronic structure of the  $\text{Zn}^{\delta+}$ -NC

(Fig. 6D). The adsorption edge position of  $\text{Zn}^{\delta+}$ -NC is comparatively low than that of ZnTPP but also found to be far away from that of Zn foil. The  $D_{4h}$  symmetry fingerprint peak of Zn- $\text{N}_4$  appears at 9 661.8 eV (which is similar to the ZnTPP spectrum) but disappears in  $\text{Zn}^{\delta+}$ -NC, indicating a non-centrosymmetric Zn-N configuration. The DFT calculations suggest that  $\text{Zn}^{\delta+}$ -NC has partially unsaturated Zn- $\text{N}_3$  and Zn- $\text{N}_3$ -V sites, which favors the  $\text{COOH}^*$  intermediate formation. The developed Zn SACs exhibit Faradaic efficiency (99%) for CO production at the overpotential of 310 mV from  $\text{CO}_2$  electrolysis. Zhu et al. have developed Zn single atom (coexistence with Co) on N-doped carbon as an efficient electrocatalyst for  $\text{CO}_2$  reduction with Faradaic efficiency of 93% for CO [107]. They have found that electronic interaction between Zn and Co atoms facilitated  $\text{COOH}^*$  formation to boost CO generation during the electrolysis of  $\text{CO}_2$ . Hao et al. have shown that the curvature of Zn- $\text{N}_x$  sites can increase the electron density of the Zn 3d orbital, which can improve the catalytic performance for  $\text{CO}_2$  reduction [108].

Various Co SACs have been explored for HER and studies show that Co SACs dispersed on N-doped graphene exhibited higher catalytic activity than those dispersed on graphene for HER [14]. Recent studies also explored Co SACs for electrochemical reduction of  $\text{CO}_2$  [35, 109]. Pan et al. synthesized atomically dispersed Co sites anchored on polymer-derived hollow N-doped porous carbon spheres as electrocatalysts for  $\text{CO}_2$  reduction, which shows almost 100% FE for CO generation at  $-0.73 \text{ V}$  [35]. Another work adopted MOF assisting with pyrolysis at a high temperature to synthesize Co SACs with  $\text{N}_4$  and  $\text{N}_4/\text{C}$  coordinated on N-doped carbon for  $\text{CO}_2$  reduction [109]. The coordination of the Co with N and N/C plays an important role in the  $\text{CO}_2$  reduction activity, such as  $\text{Co}_1\text{-N}_4$  that exhibited higher performance than the  $\text{Co}_1\text{-N}_4/\text{C}$ . Figure 6E compares the XANES spectra at the Co K-edge of various Co SACs dispersed on N-doped carbon. The synthesized  $\text{Co}_1\text{-N}_4$  showed a higher energy absorption threshold value than that of Co foil and it was found to be in between CoO and  $\text{Co}_3\text{O}_4$ , suggesting the oxidation states of Co is +2 or +3. The higher energy absorption threshold value of  $\text{Co}_1\text{-N}_{4-x}\text{-C}_x$  was much closer to  $\text{Co}_1\text{-N}_4$ , indicating a similar valance state of Co in both compounds. As shown in Fig. 6F, the main peak of  $\text{Co}_1\text{-N}_4$  and  $\text{Co}_1\text{-N}_{4-x}\text{-C}_x$  of the Fourier transformed  $k^3$ -weighted  $\chi(k)$  function of the EXAFS spectra appeared at 1.35 Å and no Co-Co path at 2.16 Å was observed, ascribing to the Co-N/Co-C coordination peak and confirming the formation of the single atoms with homogenous dispersion. The EXAFS fitting further shows that the coordination number of Co is four in both  $\text{Co}_1\text{-N}_4$  and  $\text{Co}_1\text{-N}_{4-x}\text{-C}_x$  (Fig. 6G). The radial distance and  $k$  space resolution of both Co-coordinated compounds were determined by EXAFS wavelet transform (WT). The WT contour was maximum



**Fig. 6** Characterization of Zn SAC and Co SAC. Aberration-corrected HAADF-STEM image (A), XPS Zn 2p spectra (B), Zn Auger LMM kinetic energy Spectra (C) and Zn K-edge XANES with an enlarged near-edge pattern in the inset (D). Reproduced with permission from Ref. [36]. Copyright 2021, Wiley-VCH. Co K-edge XANES spectra (E), Fourier transformed  $k^3$ -weighted  $\chi(k)$  function of the EXAFS spectra for  $\text{Co}_1\text{-N}_4$ ,  $\text{Co}_1\text{-N}_{4-x}\text{-C}_x$ ,  $\text{CoO}$ ,  $\text{Co}_3\text{O}_4$  and Co foil (F). EXAFS spectra for  $\text{Co}_1\text{-N}_4$  with an atomic structure shown in the inset, where gray, yellow and green spheres represent C, N and Co atoms, respectively (G). WT of the Co K-edge for  $\text{Co}_1\text{-N}_{4-x}\text{-C}_x$  and  $\text{Co}_1\text{-N}_4$  (H). Reproduced with permission from Ref. [109]. Copyright 2019, Elsevier



at  $4.3 \text{ \AA}^{-1}$  for  $\text{Co}_1\text{-N}_4$  and  $4.0 \text{ \AA}^{-1}$  for  $\text{Co}_1\text{-N}_{4-x}\text{-C}_x$ , confirming the presence of the Co–N–C bond (Fig. 6H). The higher contour maximum of  $0.3 \text{ \AA}^{-1}$  at  $\text{Co}_1\text{-N}_4$  suggests the existence of a shorter Co–C path. The XAFS studies suggest that Co–N coordination turned into Co–C coordination

for  $\text{Co}_1\text{-N}_{4-x}\text{-C}_x$  under the high pyrolysis temperature. The variation of the coordination state of Co with N and N/C of the Co SACs influences their catalytic activity during the electrolysis of  $\text{CO}_2$ .



### 3.2 Electrochemical Reduction of CO<sub>2</sub> on Powder-Based SAC Electrode and Structure-Property Relationship

CO<sub>2</sub> is a fully oxidized inert molecule and thermodynamically very stable. The electrochemical conversion of CO<sub>2</sub> into other molecules is a complicated process, which involves multiple electrons and proton transfer processes [110–112]. Carbon monoxide (CO), formic acid (HCOOH), acetic acid (CH<sub>3</sub>COOH), methanol (CH<sub>3</sub>OH), ethanol (CH<sub>3</sub>CH<sub>2</sub>OH), methane (CH<sub>4</sub>) and ethylene (C<sub>2</sub>H<sub>4</sub>) are the common products of CO<sub>2</sub> reduction. The formation of these molecules involves two- to twelve-electron reaction pathways and requires high energy to activate CO<sub>2</sub>. The selectivity of the products from the CO<sub>2</sub> reduction reaction primarily depends on the nature of the catalysts, applied electrode potential and properties of the electrolyte [113–115]. Various metal and carbon-based nanostructured catalysts have been evaluated for CO<sub>2</sub> reduction over the past few decades and the search for efficient catalysts for CO<sub>2</sub> conversion at low overpotential with high selectivity and stability is ongoing. SACs are embedded into a support matrix having unsaturated coordination configurations that allow the binding of reaction intermediates and facilitate catalytic reactions. The structure of the SAC, in terms of oxidation states and coordination numbers, plays a crucial role in catalytic activity. Table 2 summarizes the electrocatalytic performance of recently reported SACs in the literature for CO<sub>2</sub> reduction to value-added products. For example, Fe-SAC (Fe<sup>3+</sup>-N-C), developed by Hu and coworkers, showed excellent catalytic performance for the conversion of CO<sub>2</sub> to CO in both H-cell and gas diffusion electrode (GDE) cells [92]. Figure 7A and B shows the Faradaic efficiencies (FE) and CO current density for this catalyst, respectively. CO was detected at an overpotential of 80 mV and the FE was exhibited higher than 80% at the applied potential between −0.2 and −0.5 V (vs. RHE). The synthesized catalyst generated 20 mA cm<sup>−2</sup> for CO at −0.47 V (vs. RHE) in an H-cell, whereas 94 mA cm<sup>−2</sup> current for CO at −0.45 V (vs. RHE) with FE higher than 90% while it was conducted in GDE using 0.5 M (1 M = 1 mol L<sup>−1</sup>) KHCO<sub>3</sub>. The lower current density for CO in the H-cell indicated the limited mass transport of CO<sub>2</sub> during the electrolysis. The performance of CO<sub>2</sub> reduction of Fe-SAC depends on the state of the Fe atom in the carbon matrix. Figure 7C and D shows the operando XAS characterization of the Fe-SACs at different applied potentials for the electrochemical reduction of CO<sub>2</sub> in a CO<sub>2</sub>-saturated 0.5 M KHCO<sub>3</sub> solution [92]. The Fe<sup>3+</sup>-N-C and Fe<sup>2+</sup>-N-C loaded glassy carbon electrodes were tested at open-circuit potential and the potential between −0.1 and −0.6 V vs. RHE. Fe K-edge spectra were recorded at all these potentials as well as their dry samples and compared with Fe<sup>3+</sup>TPPCl, Fe<sub>2</sub>O<sub>3</sub>, Fe foil and FeO. The activity

of Fe<sup>3+</sup>-N-C was satisfied at −0.5 V versus RHE; however, the catalyst became unstable, further increasing the cathode potentials. The Fe K-edge shift remains the same for dry samples and at −0.4 V, which is similar to Fe K-edge of Fe<sup>3+</sup>TPPCl, suggesting that the oxidation state of Fe atom in Fe<sup>3+</sup>-N-C did not change during the reduction of CO<sub>2</sub>. However, the Fe K-edge moved to lower energies while further increasing the cathode potential to −0.5 V and higher, which is close to that of FeO, indicating the Fe<sup>3+</sup> ion of Fe<sup>3+</sup>-N-C reduced to Fe<sup>2+</sup> during the CO<sub>2</sub> electroreduction. The spectroscopic data suggest that Fe<sup>3+</sup>-N-C and Fe<sup>2+</sup>-N-C comprise pyrrolic N ligands and pyridinic N ligands, respectively. The pyridinic N ligands may stabilize Fe<sup>2+</sup> compared to Fe<sup>3+</sup>, whereas the pyrrolic N ligands have the opposite effect. Hence, the oxidation state of the Fe atom and its coordination bond play vital roles in the electrocatalysis of CO<sub>2</sub>.

SACs often contain mixed structures and coordination numbers due to the lack of a precise synthesis method, which highly hinders a proper exploration of the CO<sub>2</sub> reduction reaction mechanism, and suppresses the development of high-performance catalysts for CO<sub>2</sub> reduction. Liu et al. have synthesized Ni SAC with a precise structure and well-defined Ni-N<sub>4</sub> site supported on CNT by linking Ni-TAPc to CNT through C-C coupling for the electrochemical reduction of CO<sub>2</sub> [97]. Their developed Ni SAC exhibited excellent performance with a CO<sub>2</sub>-to-CO Faradaic efficiency of 99% and in situ spectroscopy studies revealed that Ni<sup>+</sup> in the Ni SAC was very active for CO<sub>2</sub> activation. As shown in Fig. 8A, the Faradaic efficiency is over 90% at all the applied potentials, indicating that the developed Ni SAC is highly stable for CO<sub>2</sub> reduction. The transformation of the electronic state Ni atom in Ni SAC was investigated by using operando XAS during the CO<sub>2</sub> reduction process. Figure 8B and C describes the Ni K-edge XANES spectra at various cathodic potentials in Ar-saturated and CO<sub>2</sub>-saturated KHCO<sub>3</sub> solutions, respectively. The Ni K-edge of Ni SAC shifted to lower energy of 0.3 eV when potential is increased in the Ar-saturated solution (Fig. 8B inset), indicating the reduction of Ni<sup>2+</sup> to Ni<sup>+</sup>. However, there is no Ni K-edge shift observed in CO<sub>2</sub>-saturated solution (Fig. 8C inset) under a similar cathodic bias, suggesting that the Ni center in Ni SAC maintained a +2 oxidation state and remained stable during the CO<sub>2</sub> conversion process. Based on the operando XAS results, in the CO<sub>2</sub> environment, the in situ formed Ni<sup>+</sup> center would activate CO<sub>2</sub> by donating its lone pair electrons. Pan et al. have reported on Co SAC, atomically dispersed Co sites anchored on hollow N-doped porous carbon spheres with abundant coordination N sites (Co-N<sub>5</sub>/HNPCs), which exhibited excellent performance for the reduction of CO<sub>2</sub> to CO with FE of over 90% over a wide potential range (from −0.75 to −0.88 V vs. RHE) [35]. The current density for CO<sub>2</sub> reduction of the synthesized Co-N<sub>5</sub>/HNPCs was 15.5 times higher compared to the pure CoPc

**Table 2** Electrocatalytic performance of reported various catalysts for CO<sub>2</sub> reduction to value-added products. Data are extracted from different sources and thus are with different significant digits

Catalyst	Electrolyte	Membrane	Type of cell	Cathode potential at max FE (vs. RHE when applicable unless otherwise stated)/V	Current density at max FE*/(mA cm <sup>-2</sup> )	Products	Maximum Faradaic efficiency for carbon products/ (%)	References
<b>Ag<sub>1</sub>/MnO<sub>2</sub></b>	0.1 M KHCO <sub>3</sub>	Nafion N117	Half	−0.85	2.4	CO	95.7	[30]
Ag nanoparticles/ MnO <sub>2</sub>					1.3	CO	<65	
5 nm Ag/C	0.5 M KHCO <sub>3</sub>	Nafion N117	Half	−0.75	~3.9	CO	84.4	[116]
<b>Ag<sub>1</sub>/graphene</b>	0.5 M KHCO <sub>3</sub>	Nafion N117	Half	−0.7	6.47	CO	79	[31]
Ag <sub>2</sub> /graphene					11.87	CO	93.4	
Coral-like porous Ag-1.3	0.1 M KHCO <sub>3</sub>	Nafion N117	Half	−0.8	6.36	CO	96.38	[117]
Sponge-like porous Ag nanocubes	0.1 M KHCO <sub>3</sub>	Nafion N117	Half	−0.9	7.1	CO	93	[118]
Tri-Ag nanoplates	0.1 M KHCO <sub>3</sub>	Nafion N117	Half	−0.856	~1.3	CO	96.8	[119]
<b>Ni/NG</b>	0.5 M KHCO <sub>3</sub>	Nafion N117	Half	−0.77	11	CO	95	[32]
<b>Ni/NG</b>	0.1 M KHCO <sub>3</sub>	PSMIM Anion Exchange Membrane	MEA	2.78	51.5	CO	97	[32]
<b>Ni/NC</b>	0.5 M KHCO <sub>3</sub>	Nafion 115	Half	−0.9	~10	CO	71.9	[10]
Ni NPs/NC				−0.8	~2.5	CO	28	
<b>Ni/NCNT</b>	0.5 M KHCO <sub>3</sub>	Nafion 117	Half	−0.9	41.5	CO	97	[33]
Ni/Fe-N-C	0.5 M KHCO <sub>3</sub>	Nafion 117	Half	−0.7	7.4	CO	98	[120]
Cu/Ni(OH) <sub>2</sub> nanosheets	0.5 M NaHCO <sub>3</sub>	Nafion 117	Half	−0.5	4.3	CO	92	[121]
<b>Cu-APC</b>	0.2 M NaHCO <sub>3</sub>	Nafion 117	MEA	−0.78	8.6	CO	92	[122]
Au NP/2b-GNR	0.5 M KHCO <sub>3</sub>	Selemion AMV	Half	−0.87	17	CO	80	[123]
AuCu NPs	0.1 M KHCO <sub>3</sub>	Selemion AMV	Half	−0.77	1.39	CO	80	[124]
Au NPs					1.01	CO	87	
Au-CeO <sub>x</sub> /C	0.1 M KHCO <sub>3</sub>	Nafion 115	Half	−0.89	12.9	CO	89.1	[125]
<b>Co-N<sub>2</sub></b>	0.5 M KHCO <sub>3</sub>	Nafion 115	Half	−0.63	18.1	CO	94	[34]
Co-Pc/CNT	0.1 M KHCO <sub>3</sub>	Nafion 117	Half	−0.63	~10	CO	92	[126]
CoPPc/CNT	0.5 M NaHCO <sub>3</sub>	Selemion AMV	Half	−0.54	18.7	CO	>80	[127]
<b>Co-N<sub>3</sub>/HNPCS</b>	0.2 M NaHCO <sub>3</sub>	Nafion 117	Half	−0.73	4.5	CO	99.2	[35]
CuO/SnO <sub>2</sub>	0.1 M NaHCO <sub>3</sub>	Nafion 117	Half	−0.7	~1.1	CO	90	[128]
COF-367-Co	0.5 M KHCO <sub>3</sub>	Nafion 117	Half	−1.1	3.3	CO	91	[129]
CoPc/P4PV	0.1 M NaH <sub>2</sub> PO <sub>4</sub>	-	Half	−0.75	2.0	CO	89	[130]
Au nanowires	0.5 M KHCO <sub>3</sub>	Nafion 212	Half	−0.35	8.16	CO	94	[131]
<b>Zn<sup>δ+</sup>-NC</b>	0.5 M KHCO <sub>3</sub>	-	Half	−0.57	0.9	CO	>95	[36]
	1 M KOH	Sustainion® X37-50	Flow	-	1 000	CO	98	
<b>Cu<sub>3</sub>(HHTQ)<sub>2</sub></b>	0.1 M KHCO <sub>3</sub>	-	Half	−0.4	~1	CH <sub>3</sub> OH	53.6	[37]

**Table 2** (continued)

Catalyst	Electrolyte	Membrane	Type of cell	Cathode potential at max FE (vs. RHE when applicable unless otherwise stated)/V	Current density at max FE*/(mA cm <sup>-2</sup> )	Products	Maximum Faradaic efficiency for carbon products/ (%)	References
NiPc-TFPN COF	0.5 M KHCO <sub>3</sub>	Nafion 212	Half	−0.9	14.1	CO	99.8	[132]
NiPc-TFPN COF + light					17.5	CO	100	
CoPc-TFPN COF					10.6	CO	96.1	
CoPc-TFPN COF + light					16.3	CO	98.2	
CoPc	0.5 M KHCO <sub>3</sub>	Nafion 115	Half	−0.8	~8	CO	99	[133]
Ni@NiNCM	0.5 M KHCO <sub>3</sub>	Nafion 117	Half	−0.9	~13	CO	97.6	[38]
AuCu <sub>3</sub> @Au	0.1 M KHCO <sub>3</sub>	Nafion 117	Half	−0.6	5.3	CO	97.3	[134]
Co-Ni/NPCNS	0.1 M KHCO <sub>3</sub>	Nafion 211	Half	−0.48	3.2	CO	96.4	[135]
m-Cu NPs	0.1 M KHCO <sub>3</sub>	-	Half	−1.3	~8	CH <sub>4</sub> , C <sub>2</sub> H <sub>4</sub> , C <sub>2</sub> H <sub>5</sub> OH, CH <sub>3</sub> COOH, HCOOH	~82	[136]
SnO <sub>2</sub> QWs	0.1 M KHCO <sub>3</sub>	Nafion N117	Half	−1.16	13.7	HCOOH, CO	~89	[137]
Au <sub>94</sub> Pd <sub>6</sub> NPs	0.5 M KHCO <sub>3</sub>	Nafion 117	Half	−0.7	~1.0	CO	~90	[138]
Bi-Sn/CF	0.5 M KHCO <sub>3</sub>	Nafion 117	Half	−1.14	~60	HCOOH, CO	94	[139]
Pd <sub>2</sub> DAC	0.5 M KHCO <sub>3</sub>	Nafion N117	Half	−0.85	6.76	CO	98.2	[140]
Sn/CuO <sub>2</sub>	0.5 M KHCO <sub>3</sub>	Nafion N117	Half	−1.1	~30	HCOOH, CO, CH <sub>4</sub> , C <sub>2</sub> H <sub>4</sub>	81	[141]
NSHCF900	0.1 M KHCO <sub>3</sub>	Nafion 117	Half	−0.7	103	CO	94	[142]
MoP@In-PC	0.5 M H <sub>2</sub> SO <sub>4</sub> (anode); [Bmim]PF <sub>6</sub> /MeCN/H <sub>2</sub> O (cathode)	Nafion 117	Half	−2.2 versus Ag/Ag <sup>+</sup>	43.8	HCOOH	96.5	[143]
HNCM/CNT	0.1 M KHCO <sub>3</sub>	-	Half	−0.9	~3.3	HCOOH, CO	~88	[144]
N-graphene	0.5 M KHCO <sub>3</sub>	Selemin AMV	Half	−0.84	7.5	HCOOH	73	[145]
Boron-doped diamond	0.5 M KCl/1.0 M KOH	Nafion NRE-212	Flow	Not stated	~2	HCOOH	~90	[146]
PEI-NGCNT	0.1 M KHCO <sub>3</sub>	-	Half	−1.8 versus SCE	3.8	HCOOH	87	[147]
NGM-1/CP	0.5 M H <sub>2</sub> SO <sub>4</sub> ; [Bmim]BF <sub>4</sub>	Nafion 117	Half	−1.4 versus SHE	1.42	CH <sub>4</sub> , CO	97.7	[148]
ZnN <sub>x</sub> /C	0.5 M KHCO <sub>3</sub>	Nafion 117	Half	−0.43	0.43	CO	95	[39]
Ni-SA-NC	0.5 M KHCO <sub>3</sub>	Nafion 115	Half	−0.8	26	CO	99	[40]
		Sustainion X37-50	MEA	2.6	145	CO	98	
			MEA	3.0	380	CO	98	
Ni-NCB	0.5 M KHCO <sub>3</sub>	Nafion 117	Half	−0.68	6.8	CO	99.4	[41]
	0.1 M KHCO <sub>3</sub>	PSMIM Anion Exchange Membrane	MEA	2.44	73.8	CO	102.4	
Ni-SAC (Pc)	0.5 M KHCO <sub>3</sub>	-	Half	−0.63	9.8	CO	98	[42]
	1.0 M KHCO <sub>3</sub>	-	Flow	−0.68	192	CO	96	
Ni(NC)-1	1.0 M KOH	Nafion 115	Flow	−1.82	160	CO	99	[43]

**Table 2** (continued)

Catalyst	Electrolyte	Membrane	Type of cell	Cathode potential at max FE (vs. RHE when applicable unless otherwise stated)/V	Current density at max FE*/(mA cm <sup>-2</sup> )	Products	Maximum Faradaic efficiency for carbon products/ (%)	References
<b>Pd<sub>83</sub>Cu<sub>17</sub></b>	25 mol% (mol% means molar percentages) [Bmim]BF <sub>4</sub>	Nafion 117	Half	− 2.1	~ 40	CH <sub>3</sub> OH	80	[149]
<b>c-NC</b>	0.1 M KHCO <sub>3</sub>	Nafion 117	Half	− 0.56	~ 1.5	C <sub>2</sub> H <sub>5</sub> OH	77	[150]
<b>Cu/CNS</b>	0.1 M KHCO <sub>3</sub>	Seleminion AMV	Half	− 1.2	~ 0.85	C <sub>2</sub> H <sub>5</sub> OH, CH <sub>4</sub>	~ 70	[151]
<b>Cu/Ag wire</b>	1.0 M KOH	Carbon Paper (Sigracet 35 BC, Ion Power)	Flow	− 0.68	310.8	C <sub>2</sub> H <sub>4</sub> C <sub>2</sub> H <sub>5</sub> OH CO	~ 88	[152]
<b>CoPc@Zn-N-C</b>	1.0 M KOH	Anion Exchange Membrane (unspecified)	Flow	− 1.24 − 0.69	44.3 ~ 125	CH <sub>4</sub> CO	18.3 ~ 91	[153]
<b>CoPc@Fe-N-C</b>	0.5 M KOH	Anion Exchange Membrane (unspecified)	Flow	− 0.84	275.6	CO	93	[154]
<b>C/Ag/PTFE</b>	1.0 M KOH 1.0 M KHCO <sub>3</sub>	Anion Exchange Membrane (unspecified)	Flow	− 0.8 − 1.2	~ 160 ~ 150	CO CO	> 90 > 90	[155]
<b>CoSA/HCNFs</b>	0.1 M KHCO <sub>3</sub>	Nafion 117	Half	− 0.9	67	CO	91	[28]
		-	Flow	− 0.9	211	CO	92	
<b>CuSA/TCNFs</b>	0.1 M KHCO <sub>3</sub>	Nafion 117	Half	− 0.9	93	CH <sub>4</sub> CO	~ 100	[44]
<b>Fe-N-C</b>	0.5 M KHCO <sub>3</sub>	Nafion 117	Half	− 0.5	~ 5	CO	93.5	[85]
<b>Fe-N-PC</b>	0.5 M KHCO <sub>3</sub>	Nafion 115	GDE	− 0.49	11.44	CO	~ 90	[104]
<b>FeN<sub>5</sub></b>	0.1 M KHCO <sub>3</sub>	Nafion 117	Half	− 0.46	~ 2.5	CO	97.0	[45]
<b>NiSA/PCFM</b>	0.5 M KHCO <sub>3</sub>	Nafion 117	GDE	− 1.0	308.4	CO	88	[46]
<b>Ni-N<sub>3</sub>-V</b>	0.5 M KHCO <sub>3</sub>	Nafion 117	Half	− 0.9	65	CO	> 90	[47]
<b>ACP/S-N-Ni</b>	0.5 M KHCO <sub>3</sub>	Not specified	Half	− 0.77	3.40	CO	91	[48]
<b>Ni H-CPs</b>	0.5 M KHCO <sub>3</sub>	Nafion R115	Half	− 1.0	48.66	CO	97	[49]
<b>In<sup>δ+</sup>-N<sub>4</sub></b>	0.5 M KHCO <sub>3</sub>	Nafion 117	Half	− 0.65	8.87	HCOOH, CO	96	[50]
<b>Cu-S<sub>1</sub>N<sub>3</sub>/Cu<sub>x</sub></b>	0.1 M KHCO <sub>3</sub>	-	Half	− 0.65	~ 25	CO	100	[51]
<b>CdN<sub>4</sub>S<sub>1</sub>/CN</b>	[Bmim]PF <sub>6</sub> -MeCN	Nafion 117	Half	− 2.4 versus Ag/Ag <sup>+</sup>	182.2	CO	99.7	[52]
<b>SA-Zn/MNC</b>	1 M KHCO <sub>3</sub>	-	Half	− 1.8 versus SCE	31.8	CH <sub>4</sub>	85	[53]
<b>Cu-SA/NPC</b>	Not specified	Nafion N117	Half	− 0.36	~ 4	CH <sub>3</sub> COCH <sub>3</sub> HCOOH CH <sub>3</sub> COOH CH <sub>3</sub> OH C <sub>2</sub> H <sub>5</sub> OH	~ 50	[156]
<b>Ag<sub>1</sub>-N<sub>3</sub>/PCNC</b>	0.1 M KHCO <sub>3</sub>	Nafion 211	Half	− 0.37	~ 4	CO	95	[54]
<b>PA-CuDBC-1</b>	0.5 M KHCO <sub>3</sub>	Unspecified	Half	− 1.1	47.8	CH <sub>4</sub> , CO, C <sub>2</sub> H <sub>4</sub>	96.5	[55]
<b>Ni-HMCS-3-800</b>	0.5 M KHCO <sub>3</sub>	Nafion 117	Half	− 1.0	~ 10.5	CO	~ 95	[157]



**Table 2** (continued)

Catalyst	Electrolyte	Membrane	Type of cell	Cathode potential at max FE (vs. RHE when applicable unless otherwise stated)/V	Current density at max FE*/(mA cm <sup>-2</sup> )	Products	Maximum Faradaic efficiency for carbon products/ (%)	References
<b>NiSA-NGA-900</b>	0.5 M KHCO <sub>3</sub>	Nafion N117	Half	−0.8	~6	CO	90.2	[56]
<b>Ni-N<sub>4</sub>/C</b>	0.5 M KHCO <sub>3</sub>	Nafion N117	Half	−0.8	~20	CO	98.1	[57]
<b>Ni-N<sub>4</sub>/C-NH<sub>2</sub></b>				−0.7	~30	CO	96.2	
<b>Fe-N-G-p</b>	0.1 M KHCO <sub>3</sub>	Nafion 117	Half	−0.58	4.5	CO	94	[58]

\*Partial CO current density when CO or CH<sub>4</sub> is the only desired product, and is total current density otherwise;

Bold indicates a SAC;

Italic text indicates a diatomic catalyst

as shown in Fig. 8D, indicating that the Co-N<sub>5</sub> active site plays a crucial role in the excellent catalytic activity. In CO<sub>2</sub> electroreduction, reaction pathways depend on the metal catalytic sites, leading to a difference in FE. For example, M-N<sub>5</sub> sites (M=Fe, Ni, Cu, Co) are dispersed on the same HNPCSs support to probe the effect of metal active sites on electrocatalytic activity. Figure 8E displays the FE of CO from CO<sub>2</sub> reduction, showing that Co-N<sub>5</sub>/HNPCSs possessed higher FE compared to Fe-N<sub>5</sub>/HNPCSs, Ni-N<sub>5</sub>/HNPCSs and Cu-N<sub>5</sub>/HNPCSs catalysts, indicating the vital role of Co sites in CO<sub>2</sub> reduction activity. The electronic structure of the metal sites also plays an important role in the selective reduction of CO<sub>2</sub>. As seen in Fig. 8F, the Co K-edge XANES peaks, recorded at potential from −0.66 to −0.79 V during CO<sub>2</sub> electrolysis, appeared at higher energy than that of the ex situ state, suggesting a higher oxidation state of Co. However, Co K-edge has significantly shifted when 0.88 V is applied and FE of CO is also decreased at this potential, suggesting that the electronic structure of metal sites is also important for the electrochemical reduction of CO<sub>2</sub>. Shang et al. have designed In SAC with In<sup>δ+</sup>-N<sub>4</sub> atomic interface moieties on MOFs derived N-doped carbon matrix (In-SAC/NC), which served as a highly efficient electrocatalyst for electrochemical reduction of CO<sub>2</sub> to formate [50]. Figure 8G compares the FE and turnover frequency (TOF) for HCOO<sup>−</sup> production at various potentials of In-SAC/NC, In-NP/NC and NC. The In-SAC/NC attained FE<sub>HCOOH</sub><sup>−</sup> over 85% in the potential between −0.65 and −0.95 V (vs. RHE) and exhibited over 12 500 h<sup>−1</sup> TOF at −0.95 V, suggesting superb catalytic activity of In-SAs/NC owing to the exclusive In<sup>δ+</sup>-N<sub>4</sub> atomic active sites. In situ XAFS was performed at the different potential of In-SAC/NC to evaluate its chemical and atomic structure during CO<sub>2</sub> reduction. The In K-edge peak of In-SAs/NC appeared to have higher energy in the CO<sub>2</sub>-saturated 0.5 M KHCO<sub>3</sub> solution (Fig. 8H), indicating a higher oxidation state of the In sites,

suggesting the formation of CO<sub>2</sub><sup>δ−</sup> species due to a charge transfer from low-valent In<sup>δ+</sup> to CO<sub>2</sub> molecule. However, the In K-edge shifted back to lower energy during CO<sub>2</sub> reduction at −0.65 V, indicating the high activation ability of In<sup>δ+</sup>-N<sub>4</sub> sites for CO<sub>2</sub> electroreduction. As seen in Fig. 8I, the main peak of FT-EXAFS was shifted to a lower bond length of around 0.02 Å at −0.65 V and EXAFS fitting showed that the In–N bond length was much shorter when no potential was applied, suggesting that the shorter bond length of In<sup>δ+</sup>-N<sub>4</sub> sites plays a critical role for high catalytic activity and selectivity for CO<sub>2</sub> reduction.

Using a straightforward one-step synthesis method, Dong et al. covalently integrated Mn-N<sub>2</sub>O<sub>2</sub> sites into carbon nanosheets to develop a low MN-content single-atom catalyst (SAC), referred to as Mn-NO/CNs [73]. They found that the Mn-NO/CN catalyst showed impressive electrocatalytic performance for the CO<sub>2</sub> reduction reaction. In Fig. 9A, it is demonstrated that the current density in the CO<sub>2</sub>-saturated electrolyte was significantly higher for the Mn-NO/CN catalyst than for the Mn-metal containing Mn-NO/CN catalyst, but not for the Ar-saturated electrolyte. They also measured the CO<sub>2</sub> reduction performance of the Mn-NO/CN catalysts Mn-NO/CNs-900 and Mn-NO/CNs-1100 and observed that the current density in the CO<sub>2</sub> atmosphere was higher than that in the Ar atmosphere, indicating their CO<sub>2</sub> reduction activity. Figure 9B shows that the MN-containing SAC released only CO as the CO<sub>2</sub> reduction product, demonstrating superior CO<sub>2</sub> reduction performance compared to the NO/CN catalyst. At a cathode potential of −0.46 V (V vs. RHE), the maximum faradaic efficiency (FE) of CO reached 96.0%. Figure 9C reveals that the Tafel slope of Mn-NO/CNs was lower than those of the NO/CNs, Mn-NO/CNs-900 and Mn-NO/CNs-1100 catalysts. The Tafel slope of the Mn-NO/CN catalyst was closer to the theoretical value of 59 mV dec<sup>−1</sup> for the rate-limiting step, indicating faster

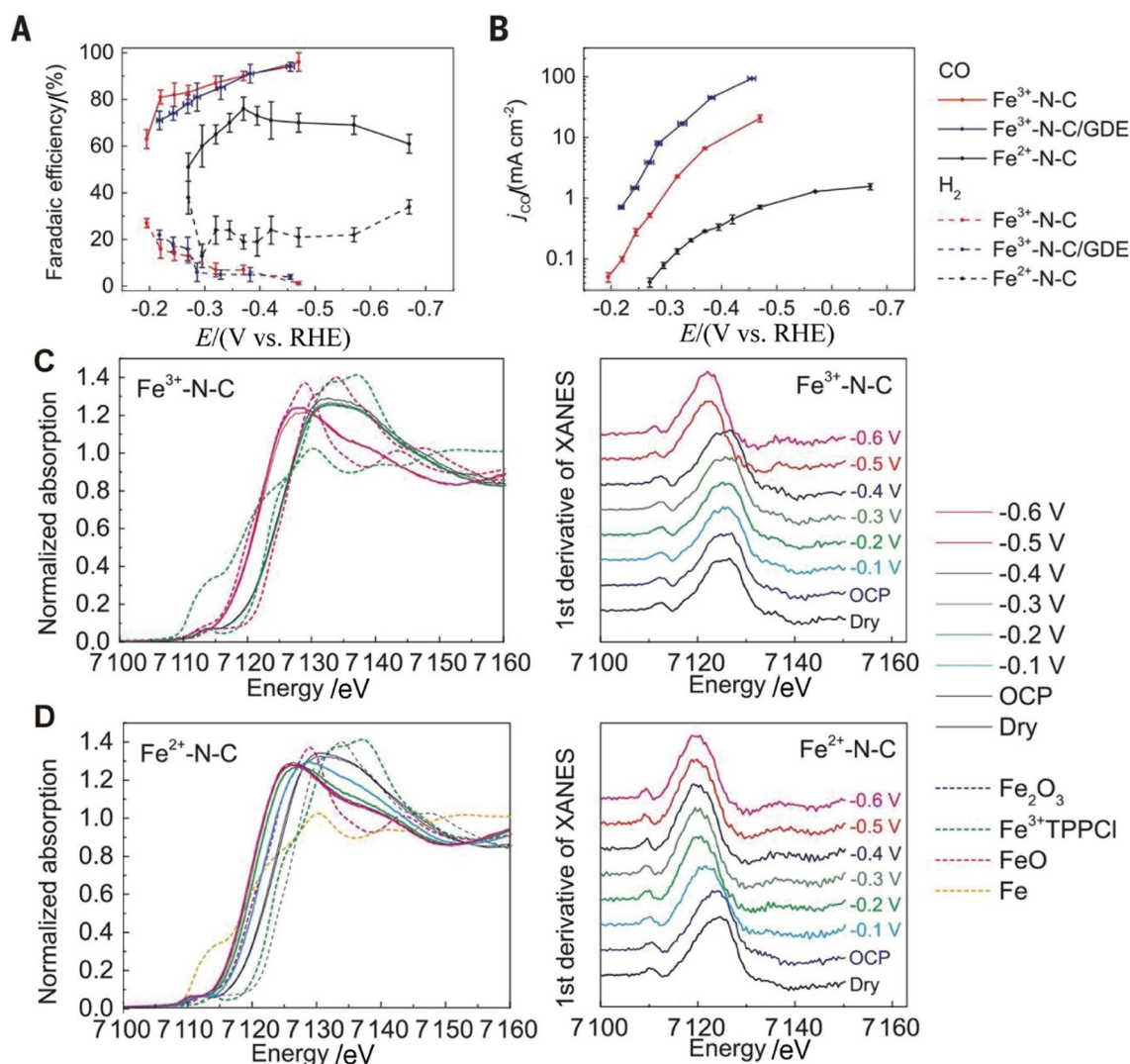


**Fig. 7** Product analysis and Operando XAS Characterization of  $\text{CO}_2$  reduction at the Fe-SAC. **A** Faradaic efficiency of CO (solid lines) and  $\text{H}_2$  (dashed lines). **B** Partial current density of CO and  $\text{H}_2$  in an H-cell and on a GDE. Operando XAS characterization of Fe-SAC at different electrode potentials, including Fe K-edge XANES spectra

(left column) and the first derivative of the spectra (right column). **C**  $\text{Fe}^{3+}$ -N-C and **D**  $\text{Fe}^{2+}$ -N-C as a dry powder (black) and loaded on glassy carbon electrodes at various applied potentials versus RHE. Reproduced with permission from Ref. [92]. Copyright 2019, Science Publishing Group

kinetics for the transfer of the first electron to adsorbed  $\text{CO}_2$  species at Mn-NO/CN. Li et al. synthesized a Ni SAC with a hierarchical hollow structure (Ni/HH) that showed a larger current density in  $\text{CO}_2$ -saturated electrolytes than in Ar-saturated ones (Fig. 9D) [88]. Ni/HH achieved a maximum FECO of 97.9%, higher than other Ni SACs (Fig. 9E). In situ ATR-SEIRAS measurements indicated that Ni/HH facilitated the formation of the rate-determining intermediate  $^*\text{COOH}$  (Fig. 9F). The special hierarchical porous structure of Ni/HH increased the number and accessibility of active sites, facilitated mass and charge transfer for enhanced kinetics and enhanced overall  $\text{CO}_2$  reduction reaction performance. Zhang et al. discovered that downsizing the active center of gallium (Ga) to the

atomic level results in SACs with unique properties [71]. Ga SACs with P, S atomic coordination environment showed higher CO formation ability than traditional gallium oxide (Fig. 9G). The Ga- $\text{N}_3\text{S}$ -PC structure achieved a CO Faradaic efficiency of 92% at  $-0.3$  V versus RHE, which was better than the Ga- $\text{N}_4$  structure (Fig. 9H). By modulating the coordination environment through polymer-coating, they could improve CO formation and restrict the HER side reaction. Through in situ FTIR test, AIMD and DFT calculation, they explored the catalytic intermediate of SAC and constructed the probable structure model of the best Ga- $\text{N}_3\text{S}$ -PC catalyst (Fig. 9I). The Ga- $\text{N}_3\text{S}$ -PC structure is flexible, and the Ga-S and Ga-P bonds are constantly reconfigured and adjusted during

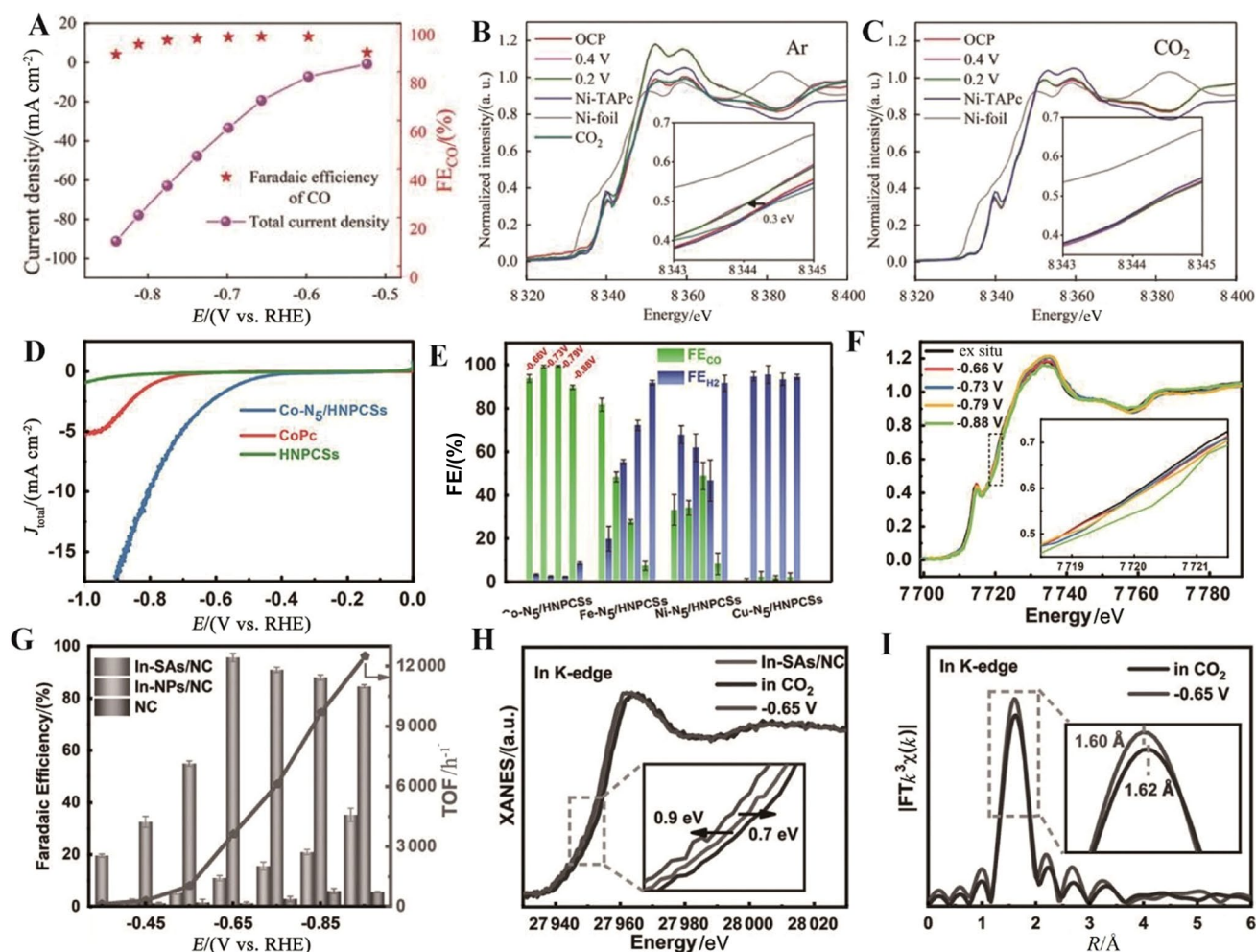


**Fig. 8** **A** Current density and CO FE (symbol) at various applied electrode potentials on Ni SAC. Ni K-edge XANES spectra of Ni-CNT-CC in 0.5 M  $\text{KHCO}_3$  aqueous solution under **B** Ar (1 atm, 1 atm = 101 325 Pa) and **C**  $\text{CO}_2$  (1 atm) atmospheres, recorded at different applied potentials; inset shows enlarged Ni K-edge XANES. The OCP is  $\sim -0.57$  V versus RHE. The  $\text{CO}_2$  line in (**C**) was obtained 5 min after switching Ar to  $\text{CO}_2$  at 0.2 V versus RHE. Reproduced with permission from Ref. [97]. Copyright 2020, Wiley-VCH. **D** LSV curves of different Co catalysts in  $\text{CO}_2$  saturated 0.5 M  $\text{KHCO}_3$  solu-

tion. FE<sub>CO</sub> and FE<sub>H<sub>2</sub></sub> of **E** M-N<sub>5</sub>/HNPCSs (M = Co, Fe, Ni, Cu). **F** XANES of Co-N<sub>5</sub>/HNPCSs catalyst under ex situ and in situ conditions (inset shows the magnified image). Reproduced with permission from Ref. [35]. Copyright 2018, American Chemical Society. **G** FEs and TOF of  $\text{HCOO}^-$  at different potentials of In SAC, In nanoparticles and N-doped carbon catalysts. **(H)** XANES and **(I)** FT-EXAFS of In-SAs/NC with and without applied voltage. Reproduced with permission from Ref. [50]. Copyright 2020, Wiley-VCH

the catalytic process, reducing the adsorption activation energy of  $\text{*COOH}$  species, thus promoting the formation of CO products.

### 3.3 DFT Studies of Electrochemical Reduction of $\text{CO}_2$ on Powder-Based SAC Electrode

Metal SACs are dispersed on various carbon supports, such as graphene, carbon nanotubes and porous carbon. These carbon supports possess high electrical conductivity and large surface area, which facilitates high active catalyst loading and uniform distribution metal atoms (Co, Ni, Fe, Zn and Cu) usually bind weakly to the carbon atoms of the carbon

substrate, which can be easily aggregated or separated from the substrate during the electrochemical reaction. Therefore, metal atoms need to chemically bond to the substrate to be stable. The stabilization of metal atoms is often achieved via binding with the defect sites or forming coordination bonds with the heteroatoms on the carbon substrate, such as N, O, P and S. The geometric and electronic structures of the metal active sites depend on the nature of the coordination atoms and coordination numbers. For example, interactions between the metal atom and  $\text{CO}_2$  molecule and reaction intermediates can vary by the strong or weak coordination bond of the metal atom with the heteroatom on the carbon substrate. Decreasing the coordination number can increase



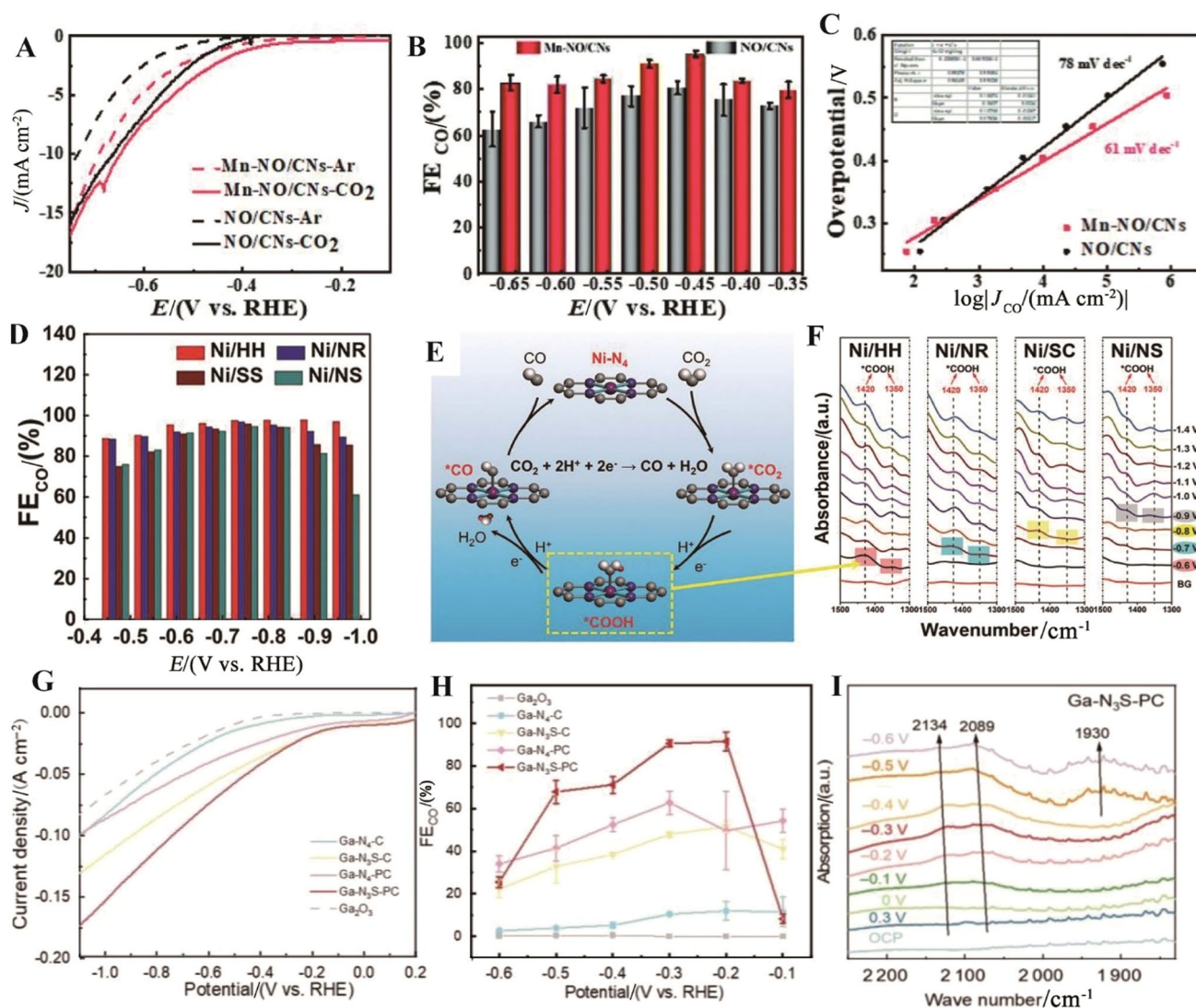


**Fig. 9** Electrocatalytic activity of Mn-NO/CN and NO/CN for CO<sub>2</sub> reduction: **A** LSV curve, **B** FE of CO and **C** Tafel slopes. Reproduced with permission from Ref. [72]. Copyright 2022, Royal Society of Chemistry. CO<sub>2</sub> reduction activity of Ni SACs: **D** FE of CO, **E** proposed reaction pathway to CO on the Ni-N<sub>4</sub> active site, and **F** in situ ATR-SEIRAS spectra at various applied potentials (purple,

blue, gray, silver, red lines represent Ni, N, C, O and H atoms, respectively). Reproduced with permission from Ref. [88]. Copyright 2023, Royal Society of Chemistry. CO<sub>2</sub> reduction performance of Ga SACs: **G** LSV curves, **H** FE of CO, and **I** in situ FTIR spectra during CO<sub>2</sub> electrolysis. Reproduced with permission from Ref. [71]. Copyright 2023, Wiley-VCH

the interaction between CO<sub>2</sub> and metal atoms [34, 158]. Density functional theory (DFT) calculation can provide an understanding of the role of active sites, coordination bonds and coordination numbers for high catalytic performance. Fe-based SACs have widely been studied for CO<sub>2</sub> electroreduction. Various synthesis approaches were been used to develop these catalysts and N-doped carbon surfaces were mainly chosen to disperse Fe atoms, where N forms coordination bonds with Fe as Fe-N<sub>4</sub> and Fe-N<sub>3</sub> [85, 87, 93, 102–104]. The coordination numbers and electronic structures of these active sites play vital roles in catalytic performance. Zhang et al. have reported on Fe-SACs/N-graphene

for electrochemical reduction of CO<sub>2</sub>, where Fe single atoms were homogeneously dispersed on N-doped graphene support and Fe-N<sub>4</sub> and Fe-N<sub>5</sub> played as the active sites for CO<sub>2</sub> reduction [93]. According to the experimental results, the Fe-N<sub>5</sub> active site containing Fe-SACs/N-graphene achieved the highest CO FE of 97.0% at −0.46 V (vs. RHE), whereas the Fe-N<sub>4</sub> active site containing Fe-SACs/N-graphene exhibited ~55% CO FE. DFT calculation suggested that Fe-N<sub>5</sub> has the lowest free energy pathway for CO<sub>2</sub> to CO reduction compared to Fe-N<sub>4</sub>. The main step is CO<sub>2</sub> → \*COOH at the FeN<sub>5</sub> and \*CO desorption at the FeN<sub>4</sub> catalyst for CO production. The free energy change for CO<sub>2</sub> → \*COOH is



0.77 eV over Fe-N<sub>5</sub>, whereas Fe-N<sub>4</sub> has a much higher free energy change for the key step (1.35 eV for \*CO → CO + \*), therefore Fe-N<sub>5</sub> catalysts possessed excellent catalytic performance for the CO<sub>2</sub> to CO conversion. Li et al. have successfully fabricated a Fe-N/P-C catalyst that contains FeN<sub>4</sub>P moiety, which plays the main role in CO<sub>2</sub> reduction to CO [102]. The Fe atom was coordinated with N and P atoms forming Fe-N<sub>3</sub>/P as active sites, which were highly dispersed on the activated carbon. The Fe-N/P-C catalyst exhibited excellent catalytic activity at 0.34 V (vs. RHE) with CO FE of 98% and maintained over 90% CO FE in the potential window between −0.40 to −0.70 V in an H-type cell. Moreover, it showed outstanding long-term electrochemical stability, remaining > 96% FE of CO at −0.45 V after 24 h electrolysis. The high performance of the Fe-N/P-C catalyst for CO<sub>2</sub> reduction was evaluated by the DFT calculations as shown in Fig. 10. The DFT studies revealed that the incorporation of P into the Fe-N-C catalyst reduced the energy barrier for forming COOH\*, which is one of the key steps for CO<sub>2</sub> reduction [45, 159]. It has proven by calculating energy barriers and reaction pathways for the conversion of CO<sub>2</sub> to CO using Fe-N<sub>4</sub>-C, Fe-N<sub>3</sub>/P-C, Fe-N<sub>4</sub>/P-C and Fe-N<sub>4</sub>/Vac-P-C configurations. The free energies for the protonation of the CO<sub>2</sub> to \*COOH step for Fe-N<sub>4</sub>-C, Fe-N<sub>3</sub>/P-C, Fe-N<sub>4</sub>/P-C and Fe-N<sub>4</sub>-Vac-P-C are 0.63, 0.63, 0.48 and 0.62 eV, respectively, suggesting that the potential-limiting step is the formation of \*COOH during the CO<sub>2</sub> reduction reaction process and Fe-N<sub>4</sub>/P-C exhibited lower free energy of formation of \*COOH compared to other three single-Fe-atom configurations (Fig. 10A). Furthermore, the CO<sub>2</sub> adsorption energies were calculated to be −0.17, −0.20, −0.20 and −0.17 eV for Fe-N<sub>4</sub>-C, Fe-N<sub>3</sub>/P-C, Fe-N<sub>4</sub>/P-C and Fe-N<sub>4</sub>-Vac-P-C, respectively, suggesting that the formation of \*COOH is limited by the low adsorption energy of CO<sub>2</sub>. Desorption of \*CO from the catalyst surface can also influence the CO<sub>2</sub> reduction reaction process. The energy barriers of the \*CO → CO step were calculated to be 1.09, 1.05, 0.81 and 0.96 eV over Fe-N<sub>4</sub>-C, Fe-N<sub>3</sub>/P-C, Fe-N<sub>4</sub>/P-C and Fe-N<sub>4</sub>-Vac-P-C, respectively, suggesting that the Fe-N<sub>4</sub>/P-C configuration obtains the lowest energy barrier. The adsorption energy of CO was also determined to be −1.68 eV, −1.61, −1.39 and −1.55 eV for Fe-N<sub>4</sub>-C, Fe-N<sub>3</sub>/P-C, Fe-N<sub>4</sub>/P-C and Fe-N<sub>4</sub>-Vac-P-C, respectively, suggesting that it is unfavorable for desorption of the \*CO intermediate on the catalyst surface. As HER is the primary competitive reaction during CO<sub>2</sub> electrolysis in an aqueous solution, the Gibbs free energy barrier of hydrogen adsorption is also estimated for each configuration as shown in Fig. 10B. The energy barrier was calculated to be 0.24 eV for Fe-N<sub>4</sub>/P-C, 0.27 eV for Fe-N<sub>4</sub>-C, 0.48 eV for Fe-N<sub>3</sub>/P-C and 0.37 eV for Fe-N<sub>4</sub>-Vac-P-C, indicating that the HER is largely limited on the Fe-N<sub>3</sub>/P-C and Fe-N<sub>4</sub>-Vac-P-C configurations. Figure 10C-E shows the differential charge

density upon \*COOH, \*CO and \*H intermediates adsorption on the Fe-N<sub>4</sub>-C configuration, respectively. Similarly, Fig. 10F-H displays differential charge density for the same intermediates on the Fe-N<sub>3</sub>/P-C configuration. It is seen that the Fe center of P-tuned single-Fe-atom catalysts has more localized electrons and fewer electrons can be transferred to the P and N atoms, suggesting a lower oxidation state of Fe, which is in good agreement with the ex situ XANES results. Bader charge analysis further confirmed that Fe atom Fe-N<sub>3</sub>/P-C catalyst obtains a lower oxidation state upon \*COOH, \*CO and \*H intermediate adsorption, which consequently provides more electrons to increase CO<sub>2</sub> activation and CO desorption, revealing that the Fe tuning with P and N boosts the catalytic performance of the CO<sub>2</sub> reduction. Another Fe-SAC containing Fe-N<sub>4</sub> moieties dispersed on defective graphite layers developed by Qin et al. has exhibited a very low overpotential of 90 mV and a high FE of 93.5% at −0.5 V (vs. RHE) for CO generation [85]. Their DFT calculations suggest that if Fe centers of bulk and edge Fe-N<sub>4</sub> sites are poisoned by \*CO, they do not act as active sites for CO generation from CO<sub>2</sub>. However, high catalytic activity for CO<sub>2</sub> reduction comes from the synergistic interactions between the defective graphitic layer and the Fe-N<sub>4</sub> moiety, which supports a balanced \*COOH and \*CO binding strength, mitigating the \*CO poisoning and facilitating the low overpotential. Chen et al. have developed Fe-SACs catalyst consisting of Fe-N<sub>4</sub> sites and Fe clusters supported on porous carbon (Fe-N-PC) for efficient CO<sub>2</sub> reduction to CO with FE of ~90% and a partial CO current density of 11.44 mA cm<sup>−2</sup> at −0.49 V (vs. RHE) [104]. The DFT studies suggest that \*COOH and \*CO are the important intermediates of CO<sub>2</sub> reduction and the CO desorption step is easier and free energy change for HER was low on the Fe-N-PC catalysts surface. The Fe-SAC composed of CNT and GNR decorated by Fe-N<sub>4</sub> moieties exhibited an excellent CO<sub>2</sub> reduction performance with CO FE of 96% at the overpotential of 0.650 V [103]. DFT calculation suggests that the Fe-N<sub>4</sub> sites dispersed on CNT/GNR networks have a high capability of CO<sub>2</sub> activation and HER suppression in an aqueous solution. The CO<sub>2</sub> reduction reaction pathway involves the formation of \*COOH and \*CO intermediates including a two-step proton-coupled electron transfer process, where Fe-N<sub>4</sub> moiety works as an adsorption site for intermediates [160–162]. Moreover, the Fe-N<sub>4</sub> site has a low free energy barrier for the formation of \*COOH and shows weak adsorption for CO, enabling low onset potential for CO<sub>2</sub> to CO conversion.

Ni SACs containing various active sites, including Ni-N<sub>4</sub>, Ni-N<sub>3</sub> and Ni-N<sub>2</sub> supported on different carbon surfaces have been used as effective catalysts for electrochemical reduction of CO<sub>2</sub>. The electrocatalytic activity for CO<sub>2</sub> reduction varies on the surface structures and formation of the different intermediates and free energy changes on the

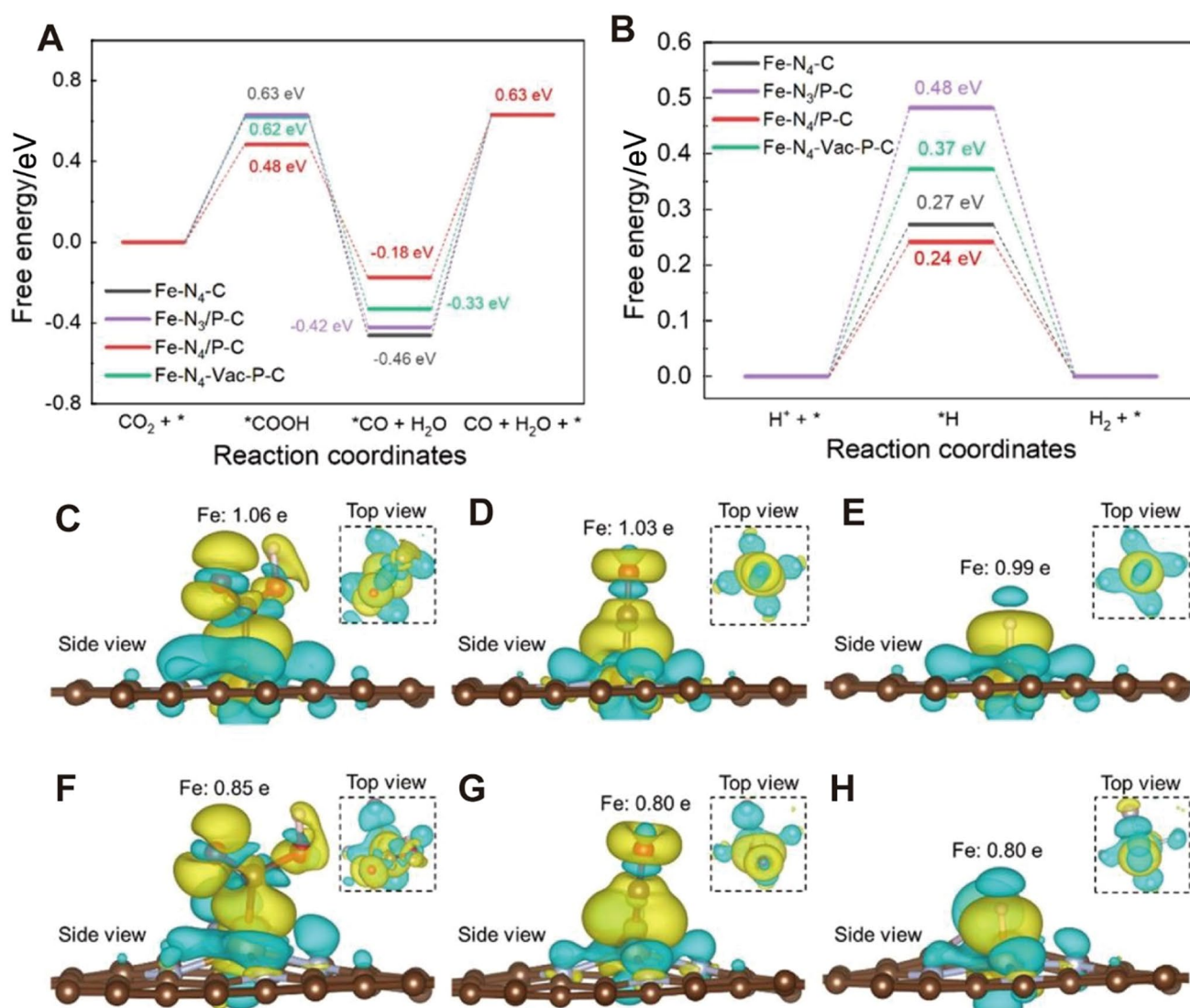


**Fig. 10** DFT calculation evaluating catalytic activity. **A** Gibbs free energy profiles for electroreduction of  $\text{CO}_2$  to  $\text{CO}$  on single-Fe-atom structures with different coordination environments. **B** Gibbs free energy profiles for hydrogen adsorption on the single-Fe-atom structures with different coordination environments. Differential charge densities of Fe- $\text{N}_4$ -C (**C**, **D** and **E**) and Fe- $\text{N}_3$ /P-C (**F**, **G** and **H**) after

the adsorption of  $^*\text{COOH}$ ,  $^*\text{CO}$  and  $^*\text{H}$  intermediates near the Fe atom. Yellow and cyan isosurfaces represent electron accumulation and depletion, respectively, which shows an isosurface value of  $0.0015 \text{ e } \text{\AA}^{-3}$ . Reproduced with permission from Ref. [102]. Copyright 2022, American Chemical Society

active sites. Fan et al. have synthesized Ni SACs supported on the CNT with homogeneously distributed  $\text{Ni-N}_3$  moiety, which exhibited an improved  $\text{CO}_2$  reduction activity compared to Ni nanoparticles [106]. According to their XANES and XPS analysis, Ni-N has a coordination number of  $2.5 \pm 0.2$  and the Ni atom is coordinated with both pyridinic N [ $\text{Ni@N}_3$ (pyridinic)] and pyrrolic N [ $\text{Ni@N}$ (pyrrolic)], as shown in Fig. 11A. DFT calculation indicated that the  $\text{Ni@N}$ (pyrrolic) site plays a vital role in high catalytic activity for  $\text{CO}_2$  to  $\text{CO}$  conversion (Fig. 11B). The free energy changes for the formation of  $^*\text{COOH}$  intermediate are  $-0.2 \text{ eV}$  at  $\text{Ni@N}$ (pyridinic),  $0.29 \text{ eV}$  at  $\text{Ni(111)}$  and

$1.09 \text{ eV}$  at  $\text{Ni@N}$ (pyrrolic). The second intermediate  $^*\text{CO}$  formation is exothermic at all the catalyst surfaces. The  $\text{CO}$  desorption step is highly endothermic at  $\text{Ni@N}$ (pyridinic) and  $\text{Ni(111)}$ ; however, the same step is exothermic with free energy changes of  $0.03 \text{ eV}$  at  $\text{Ni@N}$ (pyrrolic), suggesting that  $\text{Ni@N}$ (pyridinic) and  $\text{Ni(111)}$  sites can easily be poisoned by  $^*\text{CO}$ . The free energy changes for the formation of  $^*\text{COOH}$  and desorption of  $\text{CO}$  were also estimated on  $\text{Ni-N}_4$  sites, showing that free energy change for  $\text{CO}$  desorption is similar to  $\text{Ni@N}$ (pyrrolic) site and  $^*\text{COOH}$  formation requires  $1.54 \text{ eV}$  on the  $\text{Ni-N}_4$  site, which is much higher than that of the  $\text{Ni@N}$ (pyrrolic) site, indicating that

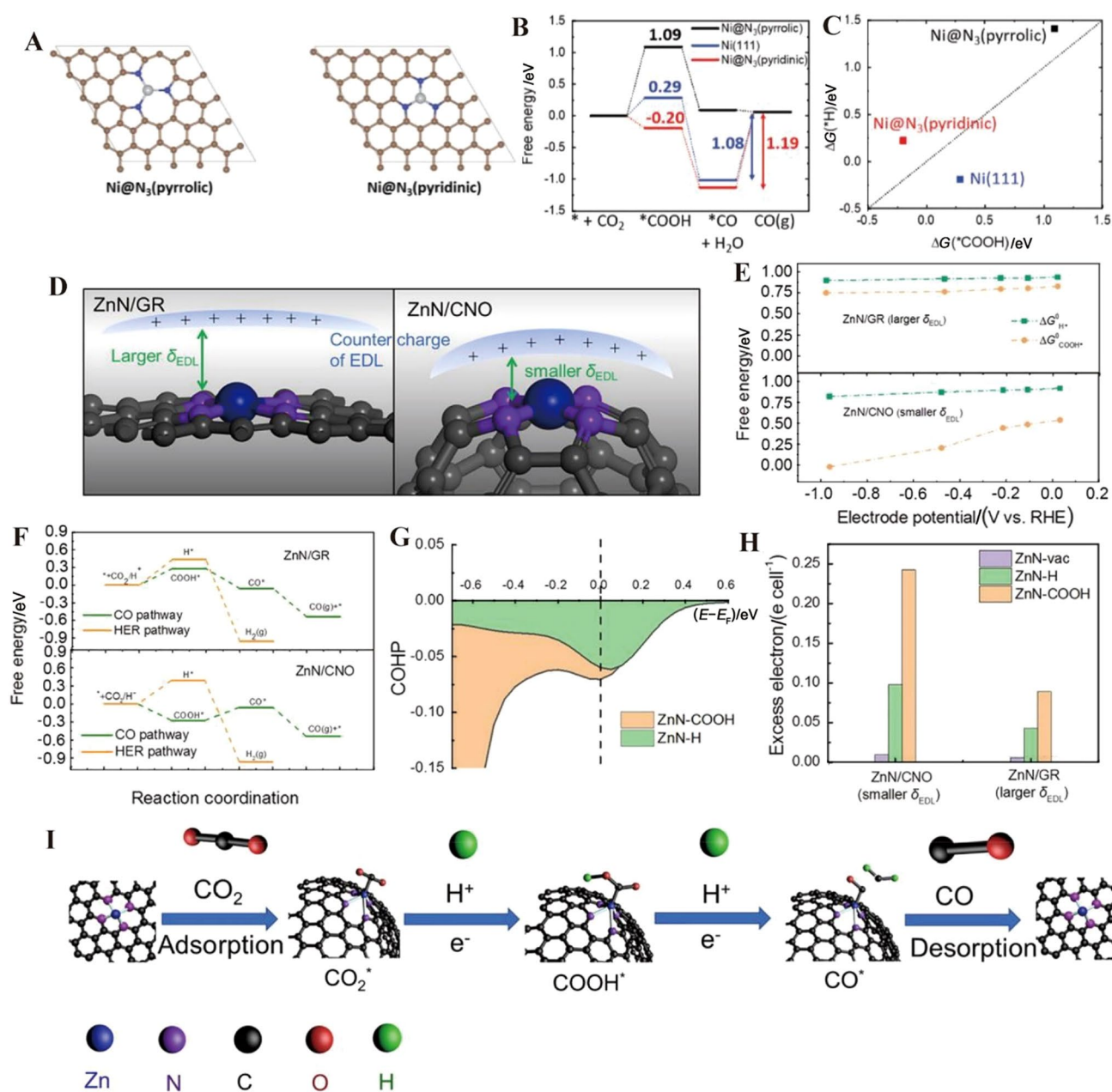


**Fig. 11** A Schematic representation of Ni@N<sub>3</sub>(pyrrolic) and Ni@N<sub>3</sub>(pyridinic) models for CO<sub>2</sub> reduction reaction. Gray, brown and blue balls represent Ni, C and N atoms, respectively. B Free energy diagram illustrating the electrochemical reduction of CO<sub>2</sub> to CO. C Comparison of  $\Delta G(^*H)$  and  $\Delta G(^*COOH)$ . Reproduced with permission from Ref. [106]. Copyright 2020, Wiley-VCH. D Schematic showing the key practical difference between ZnN/CNO and ZnN/GR in terms of thickness of the EDL (0.3 and 0.9 nm). E The potential-dependent standard formation Gibbs free energy of COOH\* and H\* for ZnN/GR (above) and ZnN/CNO (below). F Reaction free energy

diagrams of HER and CO<sub>2</sub> reduction reaction pathway for ZnN/GR (above) and ZnN/CNO (below) on  $U_{RHE} = -0.48$  V. G The projected crystal orbital Hamilton population (pCOHP) analysis for Zn-H (orange) and Zn-C (green) bonds in ZnN-H and ZnN-COOH, respectively, on ZnN/CNO at  $U_{RHE}=0$  V. H The excess electron number in the unit cell for ZnN/CNO and ZnN/GR under  $U_{RHE} = -0.5$  V. I Proposed reaction pathways for complete CO<sub>2</sub> reduction reaction on ZnN/CNO. Reproduced with permission from Ref. [108]. Copyright 2021, Elsevier

the Ni@N(pyrrolic) site is better than the Ni-N<sub>4</sub> site for CO<sub>2</sub> reduction activity [15, 89]. The Ni@N<sub>3</sub> site in both pyridinic and pyrrolic obtained more negative  $\Delta G(^*COOH)$  than  $\Delta G(^*H)$ , indicating that CO<sub>2</sub> reduction can be dominant on

the Ni@N<sub>3</sub> site, as shown in Fig. 11C. However, the  $\Delta G(^*H)$  is more negative than  $\Delta G(^*COOH)$  on Ni(111), suggesting that HER is more favorable than CO<sub>2</sub> reduction on Ni(111) site (Fig. 11C). Bao group has developed coordinatively



unsaturated Ni-N sites supported on porous carbon for CO<sub>2</sub> reduction with CO FE of 92.0%–98.0% at the potential between −0.53 and −1.03 V (vs. RHE) [86]. The free energy changes of \*COOH on coordinatively unsaturated Ni-N sites are much lower than those on Ni-N<sub>4</sub>, implying that the enhanced CO<sub>2</sub> reduction activity could originate from the coordinatively unsaturated Ni-N sites. Ni atoms dispersed on the graphene layer have also been studied for CO<sub>2</sub> reduction, showing that free energy change for \*COOH is more negative than \*H and CO desorption is low, indicating the high catalytic activity for CO<sub>2</sub> reduction of the Ni-C site [32]. The Co-N<sub>5</sub> site anchored in N-doped porous carbon spheres has shown excellent CO<sub>2</sub> reduction activity with CO FE over 90% at a wide range of potential of −0.57 to −0.88 V (vs. RHE) [35]. DFT calculations suggest that the Co-N<sub>5</sub> site can simultaneously activate CO<sub>2</sub> molecule, form \*COOH intermediate and desorb CO easily.

Zn-based SACs have emerged as one of the most competitive CO<sub>2</sub> reduction catalysts [36, 39, 53, 108]. The Zn can form a coordination bond with N as Zn-N<sub>4</sub> active site supported on the carbon substrate. Xu's group has synthesized carbon-supported N-anchored Zn SAC for CO<sub>2</sub> to CO conversion with FE up to 95% at −0.43 V (vs. RHE) [39]. The formation of \*COOH and \*CO intermediates has a low free energy barrier on the Zn-N<sub>4</sub> site compared to N<sub>4</sub>-C and Zn-C sites. Moreover, desorption of CO on the Zn-N<sub>4</sub> active site has more negative free energy than the other two active sites, indicating a high CO selectivity for the Zn-N<sub>4</sub> site. The surface curviness of the carbon substrate of the Zn SACs may also play important role in catalytic activity for CO<sub>2</sub> reduction. For example, Hao et al. have developed Zn SAC, where Zn-N<sub>4</sub> sites were homogeneously dispersed on N-doped carbon onions (Zn SACs/N-CNO), as the catalyst for electrochemical reduction of CO<sub>2</sub>, obtaining a CO FE ~97% at −0.47 V (vs. RHE) and over 100 h durability without losing activity [108]. The effects of curviness of carbon substrates were studied by DFT calculations, as shown in Fig. 11D–I. The electrochemical double-layer (EDL) charge of the flat and curved surface decorated by Zn single atoms was estimated by the Gouy-Chapman-Stern model, which found that the curved surface catalyst (Zn SACs/N-CNO) exhibited lower EDL charge than the flat surface catalyst (Zn SACs/N-graphene) (Fig. 11D) [163]. However, HER dominates over the CO<sub>2</sub> reduction reaction at high overpotentials due to the mass transport limitation of CO<sub>2</sub>; therefore, the thickness of EDL could not be one of the important factors for high catalytic activity. The free energy at different potentials on both surfaces is calculated using the hydrogen electron model proposed by Norskov et al. displayed in Fig. 11E for CO generation from CO<sub>2</sub> and HER in the aqueous solution [164, 165]. The relative kinetics ( $v_{\text{HER/CO}}$ ), calculated by using the microkinetic model, was 0.07 for Zn SACs/N-graphene and  $3.5 \times 10^{-6}$  for Zn SACs/N-CNO, suggesting a higher CO selectivity at Zn SACs/N-graphene [166]. Further, free energy for

H\* and COOH\* intermediates was determined, observing that the free energy for both intermediates is similar at the surface of Zn SACs/N-graphene at all the applied potentials. However, free energy is found to be lower at higher electrode potentials at Zn SACs/N-CNO for COOH\* compared to H\*, implying that CO<sub>2</sub> reduction reaction is dominant at highly curved surface catalysts. Therefore, the product selectivity of CO<sub>2</sub> electrolysis in aqueous media is largely dependent on the relative affinity to COOH\* and H\* at the surface of the catalyst. Figure 11F displays the potential-dependent free energy changes of different intermediates on both catalysts' surfaces for CO and HER pathways. The free energy changes for COOH\* were smaller than H\* at both flat and curved surfaces, indicating that both surfaces tend to have high CO selectivity. However, the difference in the free energy changes between COOH\* and H\* ( $\Delta G(*\text{COOH}) - \Delta G(*\text{H})$ ) was found to be low at the Zn SACs/N-CNO compared to the Zn SACs/N-graphene, providing a low free energy pathway of CO at Zn SACs/N-CNO, which resulted in a higher FE for CO. Therefore, low value of  $\Delta G(*\text{COOH}) - \Delta G(*\text{H})$  than the smaller EDL charge could be the primary factor of having higher CO selectivity. The origin of lower ( $\Delta G(*\text{COOH}) - \Delta G(*\text{H})$ ) was clarified by the crystal orbital Hamilton population (COHP) analysis along with the charge analysis, shown in Fig. 11G and F, respectively. The orbitals for both Zn-COOH and Zn-H on the Fermi level have negative COHP values, which indicates having the bonding orbitals in both catalysts (Fig. 11G). Once experiments are performed at different cathode potentials, which means additional charges are applied to the systems; therefore, adsorption of both COOH\* and H\* will be strengthened. However, when EDL charge is lowered at a fixed potential, correspondingly, a larger amount of charge is injected into COOH\* rather than H\*, as shown in Fig. 11H. Therefore, COOH\* receives more charges than H\* while decreasing EDL charge, causing the stronger adsorption of COOH\*, making it a major intermediate of CO<sub>2</sub> reduction reaction and resulting in high selectivity of CO. According to the aforementioned DFT calculations, the proposed reaction pathways on Zn SACs/N-CNO for the complete CO<sub>2</sub> reduction reaction are shown in Fig. 11F. Therefore, the curvature effect is the key effect of Zn SACs/N-CNO to provide enhanced CO<sub>2</sub> reduction activity. Above results suggest that Zn-N<sub>4</sub> sites dispersing on the carbon substrate with a highly curved surface than the flat surface may possess a low EDL charge, but shows a strong COOH\* absorption, resulting in the high conversion of CO<sub>2</sub> to CO.

#### 4 Free-Standing Electrode Architecture for Electrochemical Reduction of CO<sub>2</sub>

Many nanostructured materials have been explored for the electrochemical reduction of CO<sub>2</sub>, e.g., metal nanoparticles, nanorods, nanoneedles, nanocubes and carbon-based nanostructured materials [44, 137, 167–170]. Molecular



catalysts, such as metal-porphyrin and metal-pyridine complexes have also been widely studied as catalysts for CO<sub>2</sub> reduction [171–173]. Both types of catalysts are usually in a powder form and thereby need to be attached to a support surface to use these catalysts as working electrodes. Nafion or polyvinylidene difluoride (PVDF) is commonly used as a binder material for most powdered materials. Unfortunately, the binder may block the potential active sites, lower the accessibility to the pores and decrease the electrical conductivity of the catalysts [144, 174–176]. Thus, the design of binder-free electrocatalysts is necessary to achieve high catalytic performance and many efforts have been focused on the development of free/self-standing electrodes. A free-standing electrode is an electrode having an independent and separate component that can be detached from the assembly but still retains its structural integrity and mechanical strength. Free-standing electrode architectures can be developed through the formation of nanostructured materials on flat surfaces, assembly of them into hierarchical structures and grafting molecular catalysts on the electrode surface through chemical bonding. Recently, several free-standing single-atom catalysts (FSSACs), such as Ni single-atom catalysts decorated on carbon membrane and carbon paper, Co single-atom catalysts on carbon nanofiber, Cu, Mn, Fe and Sn single-atom catalysts-doped polyanilines, Cu single-atom catalysts decorated on carbon nanofibers, have been developed as effective electrocatalysts for CO<sub>2</sub> reduction [44, 46, 48, 49, 177].

#### 4.1 Fabrication and Structure Characterization of Free-Standing SAC Electrode (FSSACE)

Various methods, such as electrospinning, solid diffusion, metal ion adsorption into carbon surface and bulk polymerization of aniline, have been employed to synthesize transitional metal single-atom free-standing electrode architectures for electrochemical reduction of CO<sub>2</sub> [28, 44, 46, 48, 49, 177]. Yang et al. have utilized the electrospinning process to construct a flexible and self-supported Ni single-atom-decorated porous carbon membrane, which possesses hierarchical pores with interconnected nanofibers [46]. The synthesized Ni single-atom-decorated carbon membrane exhibited excellent mechanical strength and Ni atoms were homogeneously distributed throughout the membrane. This membrane acted as a free-standing electrode which played a role in both gas diffusion and catalysts layers. Figure 12A shows the fabrication method of free-standing Ni single-atom/porous carbon fiber membrane (NiSA/PCFM), which involves the electrospinning process and pyrolysis treatment process. The fibers were initially electrospun from the mixture of ZIF-8 nanoparticles, Ni<sup>2+</sup> precursor and polyacrylonitrile (PAN), followed by pyrolysis at 900 °C for 2 h, where ZIF-8 acted as pore former and

Ni<sup>2+</sup> ions were reduced by polymerized PAN during the heat treatment, forming atomically disperse Ni atoms throughout the carbon matrix. The fabricated membrane was very large, robust and flexible with a size of ~280 cm<sup>2</sup> as seen in Fig. 12B, confirming the scalability of the manufacturing process to obtain the free-standing electrode. EDS analysis showed the homogeneous distribution of the Ni, C and N atoms and the accumulation of Ni elements was absent throughout the carbon support (Fig. 12C). As shown in Fig. 12D, the bright spots in the HAADF-STEM image that are uniformly dispersed in the carbon phase correspond to Ni atoms [10]. Figure 12E exhibits the XANES spectrum in the Ni K-edge of synthesized NiSA/PCFM free-standing electrodes, together with pure Ni foil and NiO as the references. The near-edge spectra of the electrode locate between Ni foil and NiO, indicating that the valence states of those isolated Ni atoms are between 0 and +2 status [10, 17]. The EXAFS spectra of NiSA/PCFM showed a dominant peak at 1.42 Å for Ni-N coordination, Ni foil at 2.20 Å for a typical Ni-Ni pair and NiO at 1.62 Å for Ni-O interaction (Fig. 12F). As seen in Fig. 12G, the fitting results suggested that the proposed local structure of NiSA/PCFM involves coordination by four N atoms (Ni-N<sub>4</sub>).

The solid-state diffusion strategy is being used to synthesize hierarchical and atomistic free-standing catalysts for different applications. Metal atoms are diffused into the carbon matrix from a bulk metal support during the thermal treatment at high temperatures in the solid-state diffusion process. The carbon support adsorbs the metal atoms and forms M–N–C moiety, which acts as active sites. Moreover, the structure of the self-supported materials can be manipulated at the nano- and atomic scales by controlling local chemical environments, which results in high catalytic activity [178, 179]. Zhao et al. have used this strategy to fabricate free-standing Ni SAC electrodes, where the Ni SAC electrode was self-supported and utilized for CO<sub>2</sub> reduction without supporting onto a conductive substrate [49]. Figure 13A describes the synthesis steps of the free-standing Ni SAC electrode. A thin film of melamine was first sprayed on Ni foil followed by heating at 1 000 °C under the Ar flow. A black carbon paper was formed with a hierarchical structure on Ni foil and peeled off after cooled down to room temperature from the Ni surface, which was used as a free-standing Ni SAC electrode for CO<sub>2</sub> reduction. The formation and distribution of Ni SAC into the matrix are shown in the HAADF-STEM image (Fig. 13B). The bright dots inside the red circles indicate the formation of the Ni atoms into the carbon support. It is seen that the isolated Ni atoms are discerned due to the variation of Z contrasts among Ni, C and N atoms and Ni atoms are homogeneously distributed throughout the carbon matrix. The flexible and self-supported Ni SAC electrode can easily be manufactured by this method to obtain various shapes and for scale-up production. As

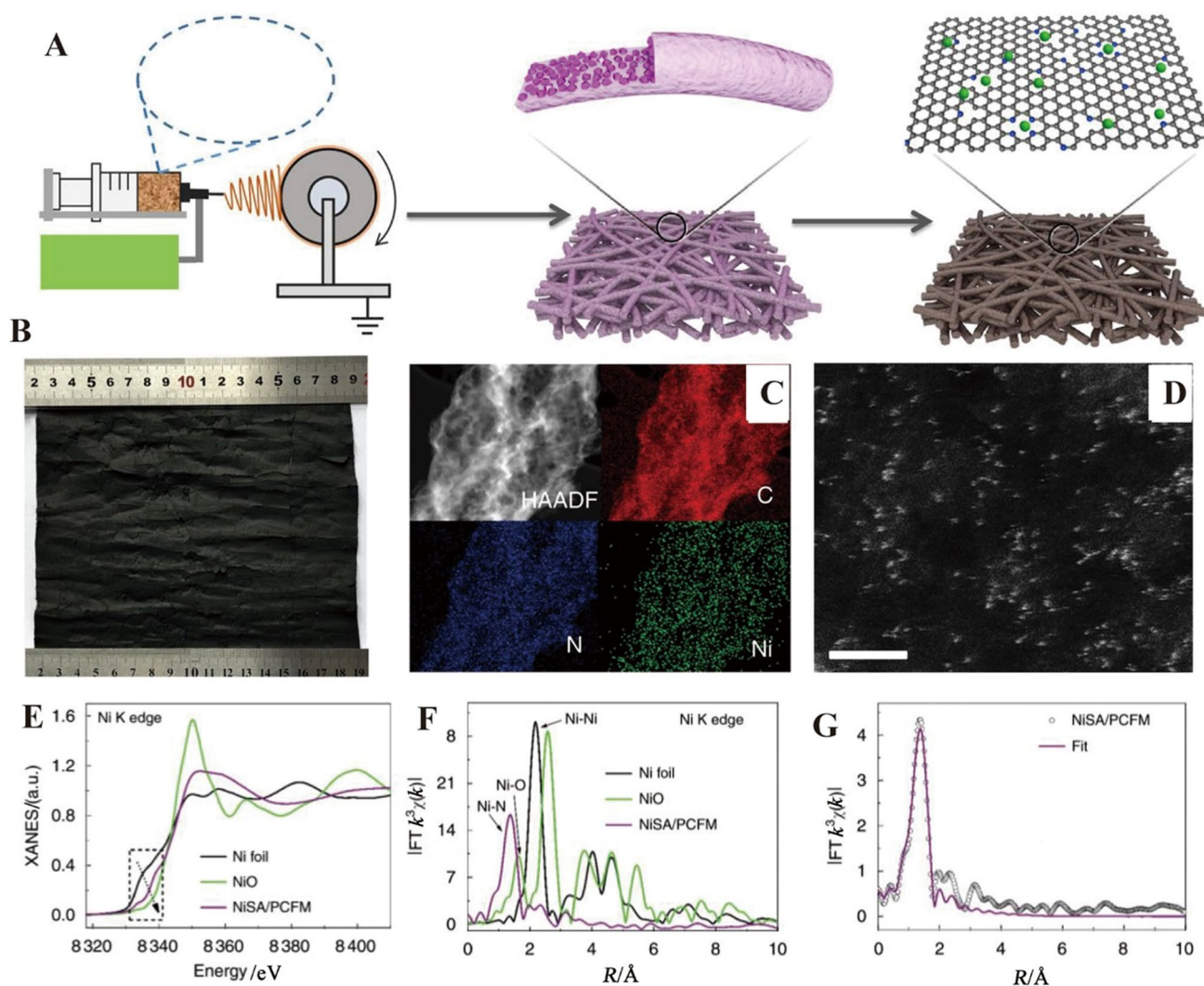


**Fig. 12** **A** Schematic representation of the synthesis of NiSA/PCFM. **B** Photograph showing the NiSA/PCFM membrane. **C** EDS mapping of a NiSA/PCFM nanofiber. **D** HAADF-STEM images of NiSA/PCFM with high-resolution. **E** XANES spectra at the Ni K-edge of

Ni foil, NiO and NiSA/PCFM. **F** The Fourier transform of EXAFS data for three samples. **G** Fitting of the EXAFS data for NiSA/PCFM. Reproduced with permission from Ref. [46]. Copyright 2020, Nature Publishing Group

shown in Fig. 13C, the free-standing Ni SAC electrode is robust and flexible and can retain its initial structure under bending stress and can tolerate a high tensile strength. Figure 13D shows the N K-edge spectrum in near-edge X-ray absorption fine structure (NEXAFS) for the synthesized self-supported Ni SAC electrode. Peak A located at 399.5 eV and peak B appeared at 402.4 eV can be assigned to pyridinic  $p^*$  and graphitic  $p^*$  transitions, respectively. However, peak D centered at 408.5 eV strongly suggests the formation of the C–N–C or C–N  $s^*$  bond in the developed free-standing Ni SAC electrode. Lu and his coworkers have used another strategy to diffuse Ni atom into the carbon support to fabricate a free-standing electrode [47]. They have synthesized vacancy defect Ni SAC with Ni–N<sub>3</sub> sites, which shows much higher catalytic activity compared to the Ni SAC-containing

Ni–N<sub>4</sub> sites. Both nitrogen and oxygen-containing precursors were heated at 500 °C with Ni(II) salt to create N/O mixing coordinated Ni–N<sub>3</sub>O SAC followed by calcination at 800 °C to generate vacancy defect Ni–N<sub>3</sub> SAC. Figure 13E illustrates the fabrication process of this vacancy defect Ni–N<sub>3</sub> SAC supported on carbon cloth. The source of oxygen and nitrogen was cyanuric acid and 2,4-diamino-6-phenyl-1,3,5-triazine, which coordinated with Ni(II) and formed N/O. Further treatment at high temperature removed the coordinated oxygen atom due to the weaker N–O bond, resulting in a vacancy defect Ni–N<sub>3</sub> SAC. The HAADF-STEM image of the obtained Ni–N<sub>3</sub>-V SAC showed abundant pores with the pore size around 1 nm in diameter. Figure 13F displays the atomic resolution HAADF-STEM image of Ni–N<sub>3</sub>-V SAC, which shows homogeneously distributed isolated Ni



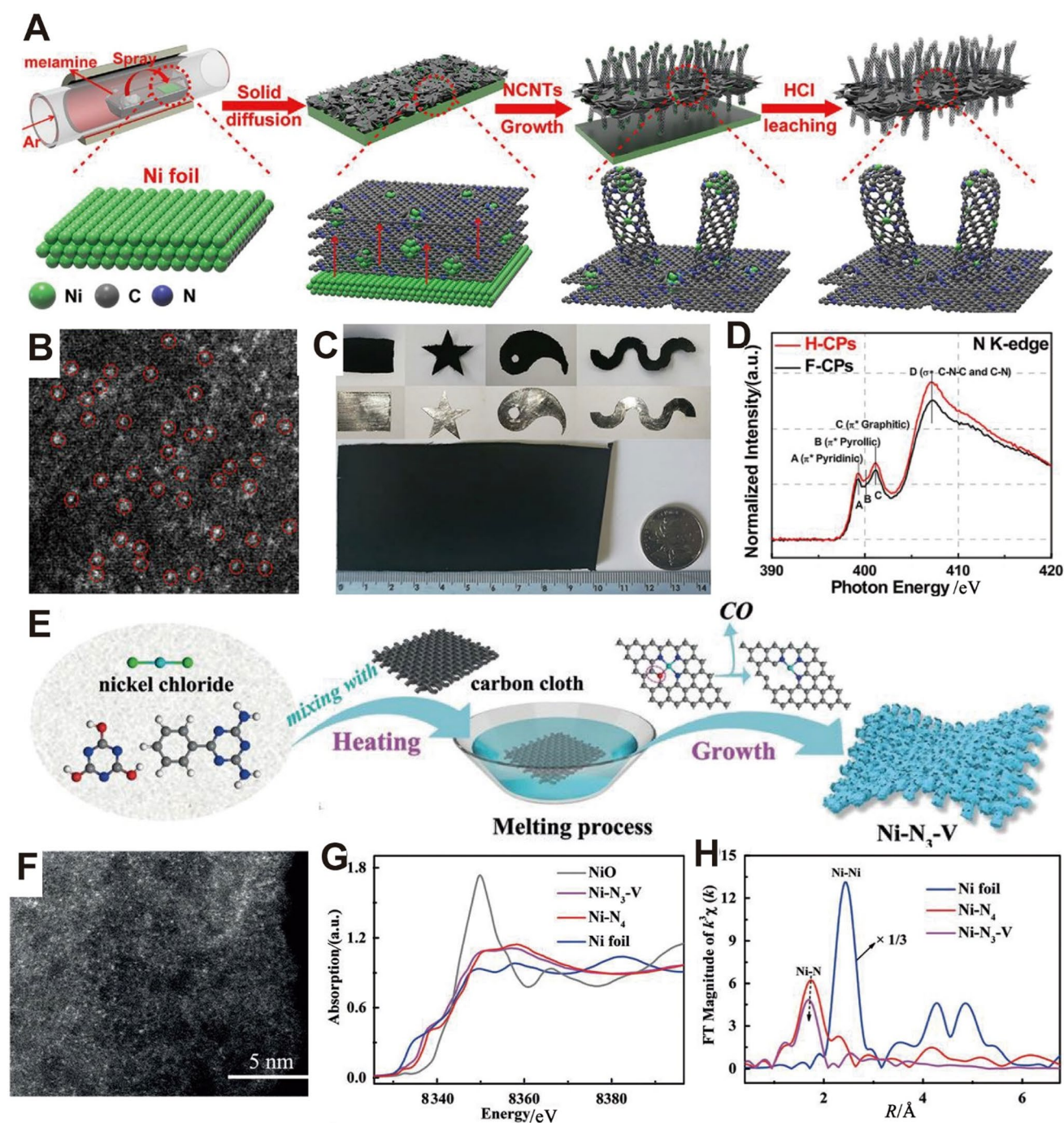


**Fig. 13** **A** Schematic representation of the process for forming H-CPs. **B** HAADF-STEM image of H-CPs at high magnification with Ni single atoms is marked with red circles. **C** The programmable and controllable shapes of the carbon papers by selecting different shapes of the carbon papers. **D** N K-edge spectra of H-CPs and F-CPs. Reproduced with permission from Ref. [49]. Copyright 2020, Cell Press Publishing Group. **E** Illustration depicting the synthesis of Ni-N<sub>3</sub>-V. **F** HAADF-

STEM image for Ni-N<sub>3</sub>-V, with bright dots indicating Ni single atoms. **G** XANES profiles for Ni-N<sub>3</sub>-V, Ni-N<sub>4</sub>, Ni foil and NiO, as measured at Ni K-edge. **H** The  $k^3$ -weighted FT-EXAFS spectra of Ni-N<sub>3</sub>-V, Ni-N<sub>4</sub> and Ni foil at Ni K-edge (Ni foil EXAFS intensity shown at one-third value). Reproduced with permission from Ref. [47] Copyright 2020, Wiley-VCH

single atoms. XAFS was carried out to investigate the electronic and structural information of Ni atoms in Ni-N<sub>3</sub>-V and Ni-N<sub>4</sub> SACs. The XANES curves for Ni-N<sub>3</sub>-V and

Ni-N<sub>4</sub> appeared at lower energy than that of NiO and higher than that of Ni foil, suggesting the charges of Ni atoms are between +2 and +1 in Ni-N<sub>3</sub>-V and Ni-N<sub>4</sub> (Fig. 13G). The

main peaks in FT-EXAFS spectra of Ni-N<sub>3</sub>-V and Ni-N<sub>4</sub> appeared around 1.86 Å (Fig. 13H), indicating the formation of Ni–N bonds as this bond length is similar to NiPc and Ni(acac)<sub>2</sub> [160]. Both Ni-N<sub>3</sub>-V and Ni-N<sub>4</sub> SACs did not have the Ni–Ni peak at 2.5 Å in their FT-EXAFS spectra, further confirming the presence of isolated Ni atoms on the carbon support.

Nitrogen-anchored Co atom (Co-N<sub>x</sub>) moieties have been considered an efficient SAC for the electrochemical reduction of CO<sub>2</sub> due to their special electronic structure [35, 109, 114]. Most of the powdered Co SACs have been used with binders to attach to a conductive substrate to make the working electrode. However, some of the active sites could be covered by the binders, which subsequently lowers the catalytic performance [144, 174]. Yang et al. have proposed a strategy for maximum utilization of Co single-atom sites via fabricating a free-standing cross-linked carbon membrane (CoSA/HCNFs) for the electrochemical reduction of CO<sub>2</sub> [28]. Figure 14A briefly describes the synthesis steps for the free-standing CoSA/HCNFs, where the electrospinning process was employed followed by pyrolysis at a high temperature. A precursor solution containing polyacrylonitrile (PAN), ZIF-8 and Co(NO<sub>3</sub>)<sub>2</sub> in DMF was electrospun at high voltage power using a parallel-plate apparatus. The synthesized nanofibrous materials were heated at 220 °C under the air environment for 1 h and then pyrolyzed at 900 °C for 1 h under the Ar gas flow. The residual Zn species in the resultant materials were removed by washing thoroughly in the H<sub>2</sub>SO<sub>4</sub> solution. The developed free-standing CoSA/HCNFs by this method possessed a large surface area with the existence of both mesopores and macropores. The isolated Co atoms were successfully formed and homogeneously distributed throughout the carbon nanofibers. The XAFS measurements suggested that the oxidation state of the Co atom in CoSA/HCNFs is between +1 and +3. The extended FT-EXAFS spectra of CoSA/HCNFs showed one main peak at 1.5 Å, which is close to Co–O peak (1.54 Å) of Co<sub>3</sub>O<sub>4</sub>, indicating the presence of Co–N first coordination bond (Fig. 14B). There was no Co–Co peak around 2.2 Å appeared for the CoSA/HCNFs, suggesting that Co atoms did not form metal particles [180–182]. Figure 14C displays the wavelet transform (WT) curve of CoSA/HCNFs, showing that it did not obtain WT curves for Co–Co bond but possessed the WT maximum at 6 Å<sup>−1</sup>, which can be attributed to the Co–N bond. EXAFS fitting suggests the formation of Co–N<sub>4</sub>–C sites and Co–N has the coordination number of 4 in CoSA/HCNFs catalysts. The developed free-standing 3D net-like CoSA/HCNFs nanofibers possessed a continuous porous structure with a large electrochemically active surface area, which can facilitate high mass transport and abundant cobalt sites for CO<sub>2</sub> reduction.

Cu-based electrocatalysts are well known for the generation of hydrocarbon fuels from CO<sub>2</sub> reduction [62,

183–186]. Various types of Cu catalysts have been developed for CO<sub>2</sub> reduction, such as nanoparticles, nanowires, nanodendrites, nanoflowers, nanoneedles and nanoalloys and others [187–191]. These nanostructured catalysts possess a large ECSA, high roughness factors and special crystal facets that play vital roles in high catalytic activity. The electrocatalytic activity for the CO<sub>2</sub> reduction is primarily determined by the surface active sites of the Cu catalysts and the contribution of internal atoms is limited. Moreover, the product selectivity and stability of these catalysts still need to be improved and the maximum utilization of the Cu atoms of the developed catalysts is a challenge. Like other metal SACs, Cu SACs can also be developed as an outstanding electrocatalyst for CO<sub>2</sub> reduction. He and his coworkers have designed Cu single atoms supported on through-hole carbon nanofibers (Cu SAs/TCNFs) as an efficient electrocatalyst, which can be directly used as a cathode for methanol production from CO<sub>2</sub> [44]. As shown in Fig. 14D, Cu SACs were synthesized by incorporating Cu into ZIF-8, which was then mixed with PAN in DMF for the electrospinning process. The resulting material was further pyrolyzed at 900 °C to obtain the Cu atoms distributed in the carbon fibers. The synthesized self-supported CuSAs/TCNFs are very flexible, can retain their initial structure under bending stress and can bear 1 MPa tensile strength. Moreover, the size of CuSAs/TCNFs was around 310 cm<sup>2</sup>, indicating that the developed free-standing CuSAs/TCNFs could potentially be synthesized on a large scale. Carbon nanofibers of the developed CuSAs/TCNFs had interconnected network structures with uniformly distributed nanoholes, showing a BET surface area of 618 m<sup>2</sup> g<sup>−1</sup>, which could facilitate a large ECSA and be in favor of high mass transport for CO<sub>2</sub> reduction. The HAADF-STEM image shows the homogeneously distributed white dots on the carbon nanofibers, which are the isolated copper atoms (Fig. 14E), which was further confirmed by XPS measurements. Inductively coupled plasma optical emission spectroscopy (ICP-OES) measurement determined the Cu amounts to be 1.3 wt% (wt% means weight percentages) in CuSAs/TCNFs. The XANES spectra exhibit a distinct line for CuSAs/TCNFs, which is situated between the Cu foil and CuO lines, suggesting that the valence state of Cu in CuSAs/TCNFs is between 0 and +2 (Fig. 14F). The FT-EXAFS spectra of CuSAs/TCNFs show a dominant peak at 1.48 Å (Fig. 14G), which could be assigned to the Cu–N coordination bond. There was no peak around 2.2 Å for Cu–Cu coordination observed in the FT-EXAFS curves, revealing the formation of isolated copper atoms instead of nanoparticles on the carbon supports [192, 193]. The above study suggests that the electrospinning method associated with pyrolysis can widely be used for the synthesis of various



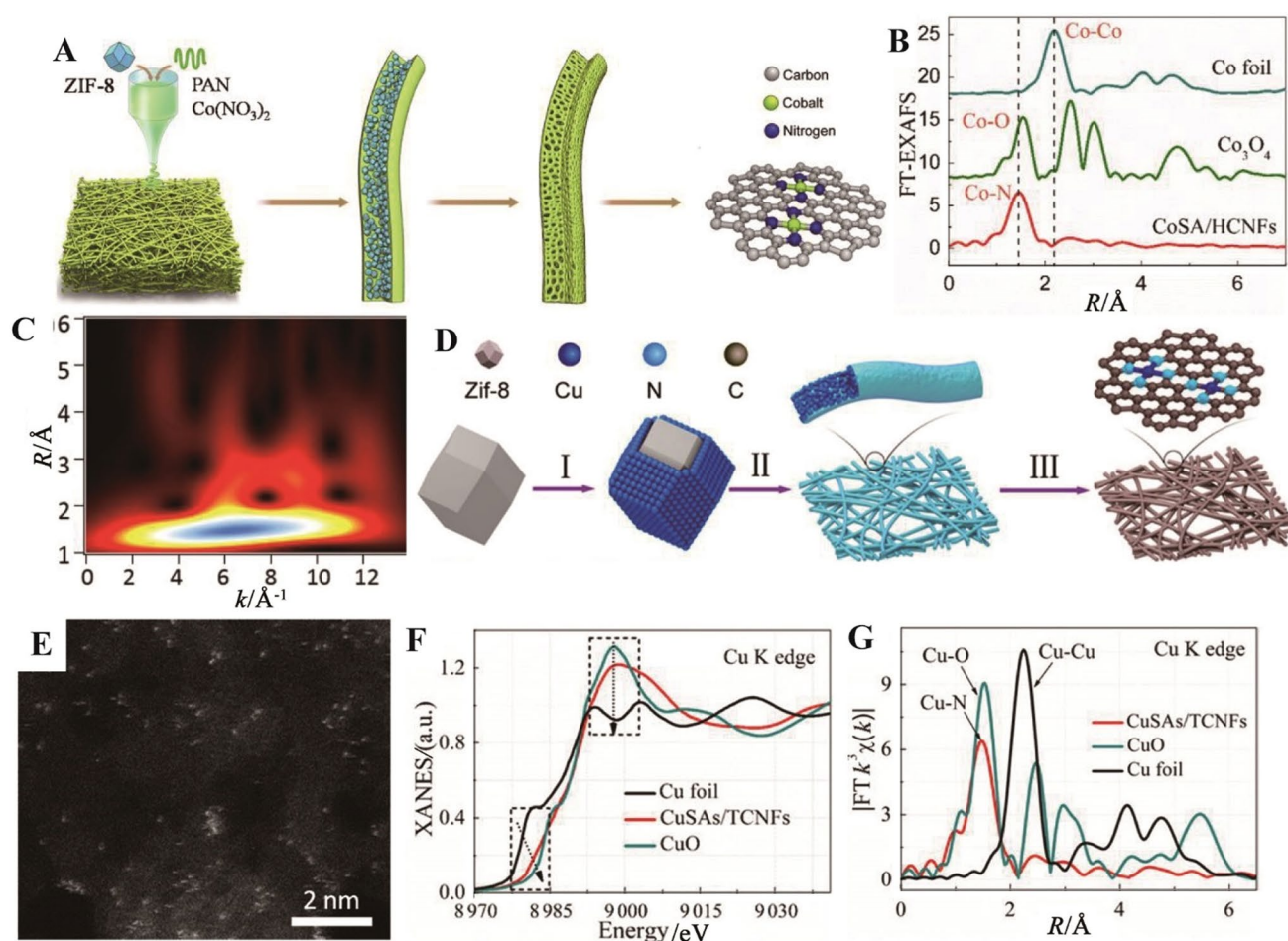


**Fig. 14** **A** Graphic representation of the process for synthesizing CoSA/HCNFs composites. **B** FT at  $R$  space of different samples. **C** WT at  $R$  space of CoSA/HCNFs. Reproduced with permission from Ref. [28]. Copyright 2020, Elsevier. **D** Synthesis procedure for CuSAs/THCF, including adsorption of Cu ions, electrospinning

of polymer fibers and carbonization and etching. **E** HAADF-STEM images of CuSAs/THCFs. **F** XANES spectra at the Cu K-edge of Cu foil, CuO and CuSAs/THCFs. **G** FT at  $R$  space of different samples. Reproduced with permission from Ref. [44]. Copyright 2019, American Chemical Society

metals SACs distributed on the carbon support for energy and environmental applications.

## 4.2 Electrochemical Reduction of CO<sub>2</sub> on FSSACE and Structure-Property Relationship

Powder-based catalysts are being used with binders to attach onto a conductive surface to make a working electrode. Unfortunately, the active sites and mass transport to the pores of the catalysts could be significantly blocked by the binder. It might also lower the electrical conductivity among the catalyst particles and limit the electron transfer at the catalyst/substrate interface. Moreover, catalyst detachment is often seen under high current density during the electrolysis of CO<sub>2</sub> due to the gas evolution [48, 144, 174, 194]. Therefore, powder-based catalysts often exhibit poor performance, which is adverse to industrial application. To overcome these limitations, researchers have focused on

developing binders-free catalysts that can be used as self-standing electrodes. Developing the free-standing single-atom catalysts can achieve much higher performance by maximizing atom or active site utilization. Yang et al. have reported on a self-standing Ni single-atom/porous carbon fiber membrane (NiSA/PCFM) catalyst for efficient reduction of CO<sub>2</sub>, which was synthesized by using the electrospinning technique [46]. The Ni single atoms were stabilized as Ni-N<sub>4</sub>-C moiety and homogeneously dispersed throughout the carbon fiber, which plays a critical role toward the catalytic activity improvement for the electrochemical reduction of CO<sub>2</sub>. The interconnected nanofibers and porous structure of NiSA/PCFM facilitate high electron transport and a large CO<sub>2</sub> diffusion to the electrode surface. The developed self-standing NiSA/PCFM can easily be integrated into the gas diffusion electrodes (GDE) device for high-performance CO<sub>2</sub> reduction. Powder-based catalysts are usually deposited onto a gas diffusion layer (GDL) in a typical GED cell

using conductive binders to determine their catalytic performance. They have also synthesized powder NiSA/PCFM and spray coated on a GDL and tested the performance for CO<sub>2</sub> reduction (Fig. 15B). Under the high current density, a large gas evolution occurred, which caused the detachment of the catalyst particles from the substrate as well as weakened the contacts between the substrate and catalysts, resulting in decreasing the long-term performance of the powder NiSA/PCFM in the GDE system [195]. The performance of the powder NiSA/PCFM electrode significantly decreased after 10 h of electrolysis once it tested in the H-type cell. As NiSA/PCFM possessed a large number of Ni-N<sub>4</sub> sites and interconnected carbon fibers, it can be integrated into GED devices to serve as both the GDL and electrode. Figure 15B shows an interface of the NiSA/PCFM and electrolyte of a GDE cell, where NiSA/PCFM acted as both the GDL and cathode. The integrated structure of NiSA/PCFM could exhibit higher stability under a high current density compared to the deposition of catalysts ink onto a GDL (Fig. 15C). The GDL-supported catalysts could easily be flooded due to the thin catalysts layer, resulting in reducing long-term performance [59, 196]. The designed self-standing NiSA/PCFM GDL could not easily be soaked by the electrolyte as the thickness of NiSA/PCFM membrane is in the micrometer range. The performance of the self-standing NiSA/PCFM catalyst for CO<sub>2</sub> reduction is assessed in both GDE and H-type cells and compared in Fig. 15D and E. The primary product of the NiSA/PCFM membrane was CO at all the applied potentials in both H-type and GDE cells. The CO FEs were higher at the low overpotentials in the H-type cell compared to the GDE cell. However, the CO FEs in the H-type cell decreased significantly once the cathode potential was lower than −1.0 V (vs. RHE), but in the GDE cell, over 80% CO FEs can still be achieved at even −1.2 V (Fig. 15D). The partial current for CO was significantly higher in the GDE cell compared to the H-type cell at all the applied potentials. For instance, CO partial current density was found to be 308.4 mA cm<sup>−2</sup> at −1.0 V in the GDE device which is ~5 times higher than that of the H-type cell (56.1 mA cm<sup>−2</sup>), though both cells achieved the same CO FE (88%). The FE of CO at −1.2 V in the GDE cell was much higher than in the H-type cell, in addition, 336.5 mA cm<sup>−2</sup> current density for CO was obtained in the GDE device, which was remarkably higher than in the H-type cell, suggesting that the NiSA/PCFM membrane efficiently reduced CO<sub>2</sub> in the GDE cell and was comparable to the industrial-relevant current densities. The stability of the NiSA/PCFM membrane was further studied in both cells at −1.0 V (vs. RHE) and achieved stability of more than 100 h, which is comparable with commercial catalyst used in the GDE device [46, 197]. FEs and partial current densities for CO were plotted with time, showing that the H-type cell shows a slow decrease in both FEs and current

densities (Fig. 15E), whereas the GDE cell exhibited only a negligible drop (5%) during 120 h electrolysis (Fig. 15F), revealing that self-standing NiSA/PCFM integrating into the GDE cell could serve as the long-term stable catalyst for CO<sub>2</sub> reduction under high current densities.

Other Ni-based free-standing SACs have also been explored for electrochemical reduction of CO<sub>2</sub>. For example, Zhao et al. have developed self-supported, flexible, binder-free and programmable hierarchical carbon paper containing Ni single atoms (NiSAs/HCP) catalyst using a solid diffusion strategy [49]. A large number of isolated Ni single atoms homogeneously distributed throughout the CNT supported on the carbon substrate and coordinated to N atoms of N-doped CNT were found, where Ni atoms defused from the bulk Ni substrate and hierarchical structure with CNTs were formed during the pyrolysis at high temperature. The electrochemical activity for CO<sub>2</sub> reduction of the developed NiSAs/HCP was much higher compared to the Ni single atoms free hierarchical carbon paper (F-CP) and bulk Ni metal [49]. For instance, the CO partial current density was 60.11 mA cm<sup>−2</sup> at −1.2 V (vs. RHE) at NiSAs/HCP in an H-type cell, which is ~7 times higher than that of Ni-free carbon paper. Figure 16A displays the FEs of both NiSAs/HCP and F-CP at different cathode potentials, showing that NiSAs/HCP obtained higher FEs at all the applied potentials. The NiSAs/HCP exhibited 90% FEs of CO in a wide range of working potentials (from −0.7 to −1.2 V), suggesting that HER was largely suppressed over the Ni sites and played a key role in the activation of CO<sub>2</sub> molecules during electrolysis [198, 199]. The long-term durability of the NiSAs/HCP for CO<sub>2</sub> reduction was also tested at −1.0 V, as shown in Fig. 16B. It maintained a stable current density over the 40 h electrolysis and FEs of CO were found to be around 90% in the entire operation, suggesting that the developed binder-free self-supported NiSAs/HCP electrode is an efficient stable catalyst for CO<sub>2</sub> reduction. Therefore, this solid-state diffusion strategy could be used to synthesize other metal SACs as well and it has great potential to produce hierarchical and atomistic catalysts for CO<sub>2</sub> reduction at the industrial level.

Free-standing Co SACs have also been explored for electrochemical CO<sub>2</sub> reduction to overcome the limitations of nanostructured powder Co-based catalysts. Co SACs show outstanding electrocatalytic performance toward CO<sub>2</sub> reduction, owing to having unique electronic structures. Different Co active sites can be formed in the Co SACs supported on N-doped carbon substrates, such as Co-N<sub>4</sub> and Co-N<sub>5</sub>, and each could route to different reaction pathways during CO<sub>2</sub> reduction, resulting in specific product formation and FEs [34, 39, 109]. Yang et al. have reported on synthesizing of Co-N<sub>4</sub> sites containing self-supported carbon nanofibers (Co SA/HCNFs) for a high generation of CO from CO<sub>2</sub> [28]. It has been derived from the polymer using

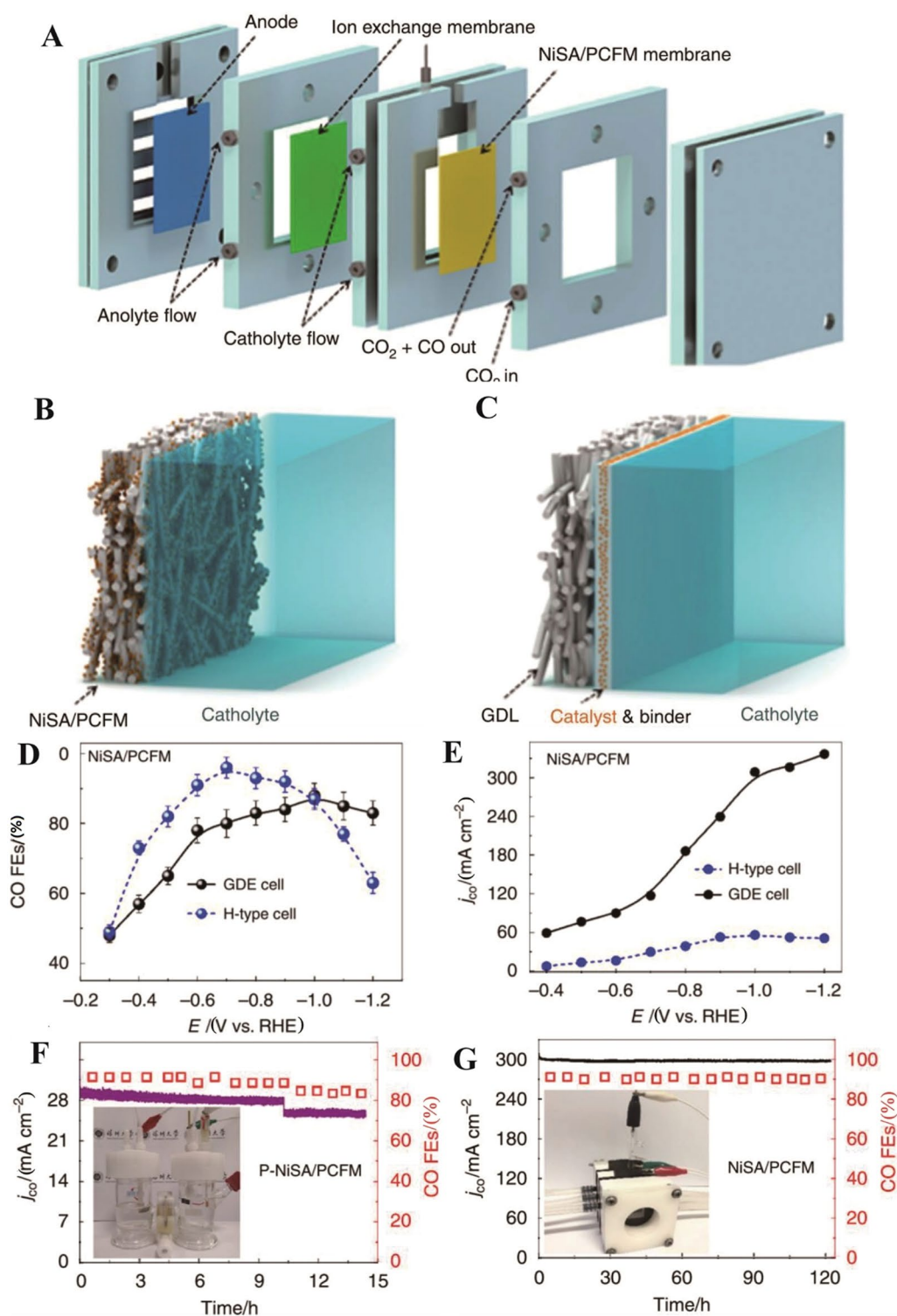


**Fig. 15** **A** Schematic representation of a GDE device. **B** Schematic illustration of NiSA/PCFM membrane directly used as a GDE. **C** A typical GDE cell with catalyst powder loaded onto a gas diffusion layer via a polymer binder for electrocatalytic CO<sub>2</sub> reduction. **D** Faradaic efficiencies CO. **E** Partial current densities of NiSA/PCFM

at various electrode potentials in different cells. Long-term stability tests at -1.0 V (vs. RHE) in a GDE cell (**F**) and an H-type cell (**G**). Reproduced with permission from Ref. [46]. Copyright 2020, Nature Publishing Group



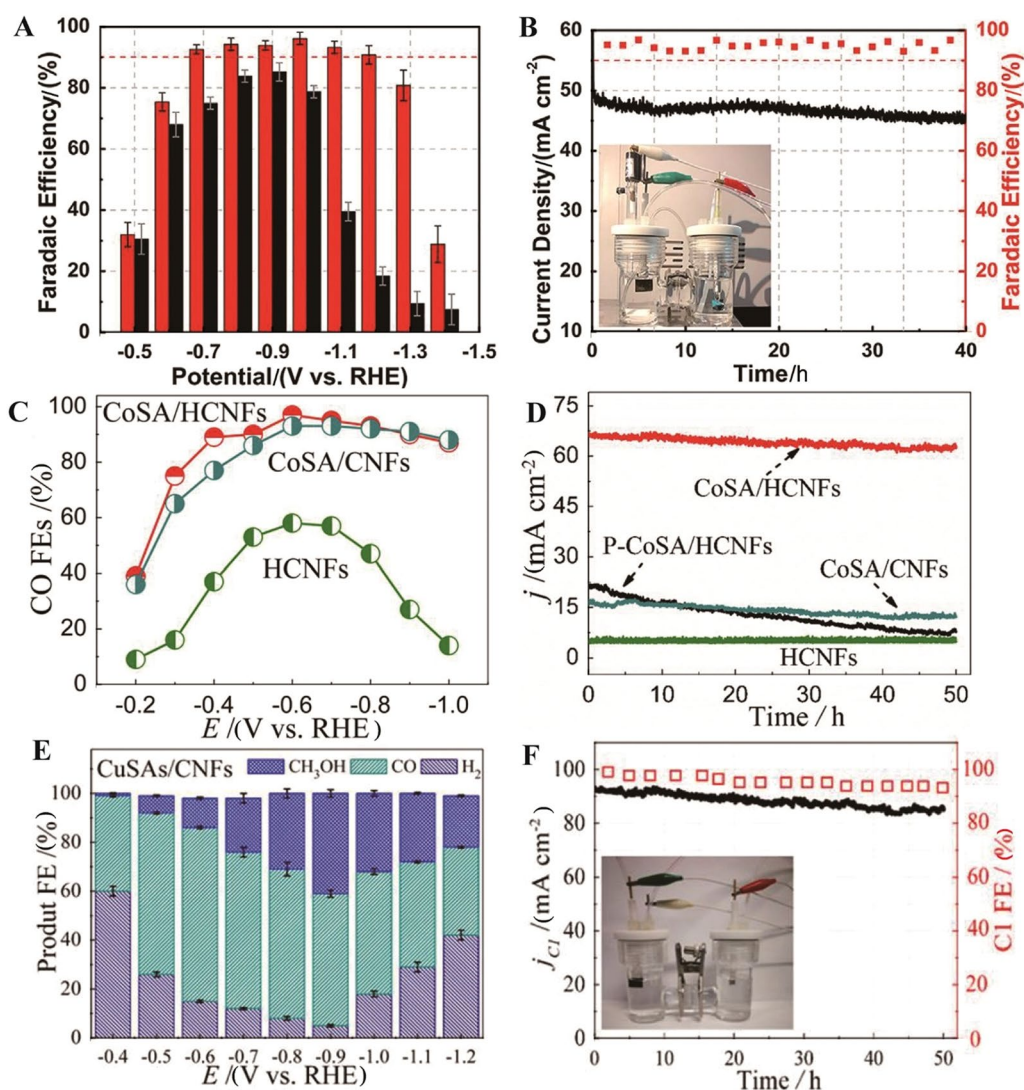


**Fig. 16** **A** Comparative FEs of CO production for H-CPs (red) and F-CPs (black) at different cathodic potentials. **B** Stability test results of H-CPs at a potential of  $-1.0$  V (vs. RHE) over 40 h. Reproduced with permission from Ref. [49]. Copyright 2020, Elsevier. **C** CO FEs of three cathodes at potentials ranging from  $-0.2$  to  $-1.0$  V (vs. RHE). **D** Long-term tests conducted at  $-0.9$  V (vs. RHE). Repro-

duced with permission from Ref. [28]. Copyright 2019, American Chemical Society. **E** FEs of CuSAs/CNFs. **F** Long-term tests results of CuSAs/CNFs performed at  $-0.9$  V (vs. RHE). Reproduced with permission from Ref. [44]. Copyright 2019, American Chemical Society

an electrospinning method following pyrolysis at high temperatures, which obtained a porous structure with interconnected carbon nanofibers, facilitating a high surface area and mass transport channel for  $\text{CO}_2$  reduction. According to XANES studies, the developed Co SA/HCNFs possessed  $\text{Co-N}_4$  sites with a homogeneous distribution throughout the carbon nanofiber matrix. The electrocatalytic activity of Co SA/HCNFs was compared with Co SA distributed on nonporous CNFs (Co SA/CNFs) and Co SA-free porous CNTs (HCNFs) in  $\text{CO}_2$ -saturated  $0.1$  M  $\text{KHCO}_3$  solution and found that Co SA/HCNFs achieved significantly higher current density in linear sweep voltammetry (LSV) studies.

The FE of CO was increasing from  $-0.2$  V to  $-0.6$  V (vs. RHE) for Co SA/HCNFs and Co SA/CNFs as shown in Fig. 16C. The Co SA/HCNFs membrane maintained CO FEs over 90% in the potential windows from  $-0.4$  to  $-0.9$  V, indicating that the  $\text{Co-N}_4$  moiety played a vital role in the high catalytic performance for  $\text{CO}_2$  reduction. The stability of these catalysts was evaluated at  $-0.9$  V (vs. RHE) for 50 h, showing that Co SA/HCNFs exhibited a significantly higher current density compared to other studied catalysts and it maintained a current density of  $\sim 65$   $\text{mA cm}^{-2}$  in the entire electrolysis (Fig. 16D), revealing the superior stability of Co SA/HCNFs. The  $\text{CO}_2$  reduction activity of the Co SA/



HCNFs was further assessed in a GDE device and showed the current density of  $211 \text{ mA cm}^{-2}$  with CO FE of 92% at  $-0.9 \text{ V}$  (vs. RHE), suggesting that the developed free-standing Co SA/HCNFs are an effective catalyst and can be used in the industrial  $\text{CO}_2$  reduction process.

Similar to other self-supported metal SACs, free-standing Cu SACs have also been studied and developed as effective  $\text{CO}_2$  reduction catalysts to mitigate the limitations of powder Cu nanostructured catalysts. Cu is well known for the production of multi-carbon species from  $\text{CO}_2$  reduction [200–203]. Various nanostructured Cu catalysts have been explored to increase production efficiency and stability. Some of these catalysts have also been used in GDE devices to further increase the production rate; however, they suffered from low stability due to high gas evolution at the electrode, resulting in loosening the catalyst particles from the substrate. Zhao et al. have synthesized powder Cu SACs for  $\text{CO}_2$  reduction, which showed moderate current density ( $\sim 17 \text{ mA cm}^{-2}$  at  $-0.76 \text{ V}$  vs. RHE). However, the catalyst obtained low FEs and lost catalytic performance within a few hours of electrolysis [156]. Considering these limitations, Yang et al. have developed free-standing Cu SAC using an electrospinning method for  $\text{CO}_2$  reduction [44]. Polyacrylonitrile has been used for fiber formation and ZIF-8 is used as the pore former during the synthesis. Interconnected through-hole structured carbon nanofibers were formed and isolated Cu single atoms were uniformly distributed throughout the carbon matrix. According to XANES and XPS characterizations, copper atoms have been coordinated with nitrogen atoms as  $\text{Cu-N}_4$  moiety in the developed Cu SACs supported on through-hole carbon nanofibers (CuSAs/TCNFs). The  $\text{CO}_2$  reduction activity of the CuSAs/TCNFs was initially evaluated in a  $\text{CO}_2$ -saturated  $\text{KHCO}_3$  solution in an H-type cell and compared with copper-free TCNFs and CuSAs/CNFs catalysts. The results showed that CuSAs/TCNFs exhibited a low onset potential of  $-0.41 \text{ V}$  (vs. RHE) and a significant high current density compared to those of TCNFs and CuSAs/CNFs. According to gas chromatography (GC),  $^1\text{H}$  NMR and  $^{13}\text{C}$  NMR studies, CO and  $\text{CH}_3\text{OH}$  were the primary products of  $\text{CO}_2$  reduction at CuSAs/TCNFs. Figure 16E displays the corresponding FEs at different applied potentials, which shows that the FE increased from  $-0.4$  to  $-0.9 \text{ V}$  and decreased at high overpotentials, indicating that HER competes with  $\text{CO}_2$  reduction at higher electrode potentials [204, 205]. The developed CuSAs/TCNFs obtained nearly 100% FE at  $-0.9 \text{ V}$  with 44% FE of  $\text{CH}_3\text{OH}$  and 56% FE of CO, whereas TCNFs produced CO as the main product at this potential, indicating that  $\text{Cu-N}_4$  is the active site for the methanol production. The stability of the free-standing CuSAs/TCNFs was performed at  $-0.9 \text{ V}$  for 50 h as shown in Fig. 16F. It maintained a steady-state current density ( $\sim 90 \text{ mA cm}^{-2}$ ) and overall FE of 90% in the entire electrolysis with very low

degradation. The interconnected network of the carbon fibers facilitated high ECSA, and the through-hole structure provided mass transport for  $\text{CO}_2$  onto the Cu active sites for  $\text{CO}_2$  reduction. Moreover, the developed self-standing CuSAs/TCNFs have a good mechanical strength to be used as the working electrode directly, which discards the typical powder binding procedure. Therefore, the development of free-standing metal SACs could benefit the  $\text{CO}_2$  electrocatalysis process by utilizing maximum active sites, resulting in high production rates and excellent stability, which could be used as potential standalone electrodes for  $\text{CO}_2$  reduction on the industrial scale.

### 4.3 DFT Studies of Electrochemical Reduction of $\text{CO}_2$ on FSSACE

DFT has been used to study free energy changes during intermediate formation and adsorption at the active sites and the reaction free energies of primary steps, which provides a clear understanding of the outstanding performance of the free-standing single-atom catalysts for  $\text{CO}_2$  reduction. The HER competes with  $\text{CO}_2$  reduction during the electrocatalysis of  $\text{CO}_2$  in the aqueous system and  $^*\text{H}$  is the well-recognized key intermediate in the former case, whereas  $^*\text{COOH}$  becomes the primary intermediate of  $\text{CO}_2$  reduction to CO [206, 207]. There are multiple steps involved in the  $\text{CO}_2$  to CO conversion on metal active sites. The three main steps are: (1) the  $\text{CO}_2$  molecule as the initial state; (2) the formation of adsorbed intermediate states ( $^*\text{COOH}$ ,  $^*\text{CO}$ ) and (3) the CO molecule as the terminal state [164, 208, 209]. Among these, the formation of adsorbed  $^*\text{COOH}$  from  $\text{CO}_2$  molecule is the rate-limiting step, making it the most important intermediate and free energy change of it reflects the  $\text{CO}_2$  reduction reaction activity. In addition,  $\Delta G$  of the  $^*\text{CO}$ -to-CO gas-phase conversion step also affects the reactivity of  $\text{CO}_2$  reduction. The Ni single atoms uniformly distributed on a porous carbon fiber membrane (Ni SAC/PCFM) were reported as an effective self-supported free-standing catalyst for the reduction of  $\text{CO}_2$  [46]. The developed Ni SAC/PCFM exhibited a partial current density of  $308.4 \text{ mA cm}^{-2}$  for CO with 88% FE for up to 120 h at  $-1.0 \text{ V}$  (vs. RHE). DFT calculation suggests that the rate-determining step requires low free energy at the  $\text{Ni-N}_4\text{-C}$  site of the Ni SAC/PCFM, which eases the  $\text{CO}_2$  to CO conversion. The free energy diagram of different adsorbed intermediates of  $\text{CO}_2$  reduction at N-C and  $\text{Ni-N}_4\text{-C}$  sites is shown in Fig. 17A. It is seen that the formation of  $^*\text{COOH}$  is uphill and it is the first electronic step, which could be the rate-determining step for both systems [89]. For instance,  $\Delta G$  for  $^*\text{COOH}$  is 0.7 eV at the  $\text{Ni-N}_4\text{-C}$  site and 1.3 eV at the N-C site, suggesting that the  $\text{Ni-N}_4\text{-C}$  catalyst has a high reaction rate of  $\text{CO}_2$  reduction than that of the N-C catalyst. Figure 17B displays the Tafel plot of  $\text{CO}_2$  reduction at different catalysts, where Ni SAC/

PCFM obtains a much smaller Tafel slope, suggesting that the CO generation rate is high at Ni SAC/PCFM compared to other catalysts, which is consistent with the DFT calculation as described in Fig. 17A [46, 210]. Rong et al. have developed a vacancy defect Ni SAC (Ni-N<sub>3</sub>-V-SAC) for efficient CO<sub>2</sub> reduction with a high CO FE of 90% and turnover frequency of  $1.35 \times 10^5$  h at  $-0.9$  V (vs. RHE), which was much higher than those of Ni-N<sub>3</sub> and Ni-N<sub>4</sub> catalysts [74]. The free energy change for the adsorbed \*COOH step is calculated to be 1.649 eV at Ni-N<sub>4</sub>, 0.680 eV at Ni-N<sub>3</sub>-V

and  $-0.061$  eV at Ni-N<sub>3</sub>. The adsorbed \*CO step shows 0.870,  $-0.110$  and  $-1.014$  eV free energy changes at Ni-N<sub>4</sub>, Ni-N<sub>3</sub>-V and Ni-N<sub>3</sub>, respectively. However, the conversion of \*CO to CO at the Ni-N<sub>3</sub> site requires 1.264 eV, which is much higher compared to Ni-N<sub>4</sub> and Ni-N<sub>3</sub>-V, suggesting that Ni-N<sub>3</sub> without a vacancy is not an effective catalyst for CO<sub>2</sub> reduction [211]. The  $\Delta G$  value for CO<sub>2</sub>-to-CO conversion is determined to be the lowest at the Ni-N<sub>3</sub>-V site, revealing that the presence of a vacancy defect at the Ni-N<sub>3</sub> site can boost the CO<sub>2</sub> reduction activity. A free-standing

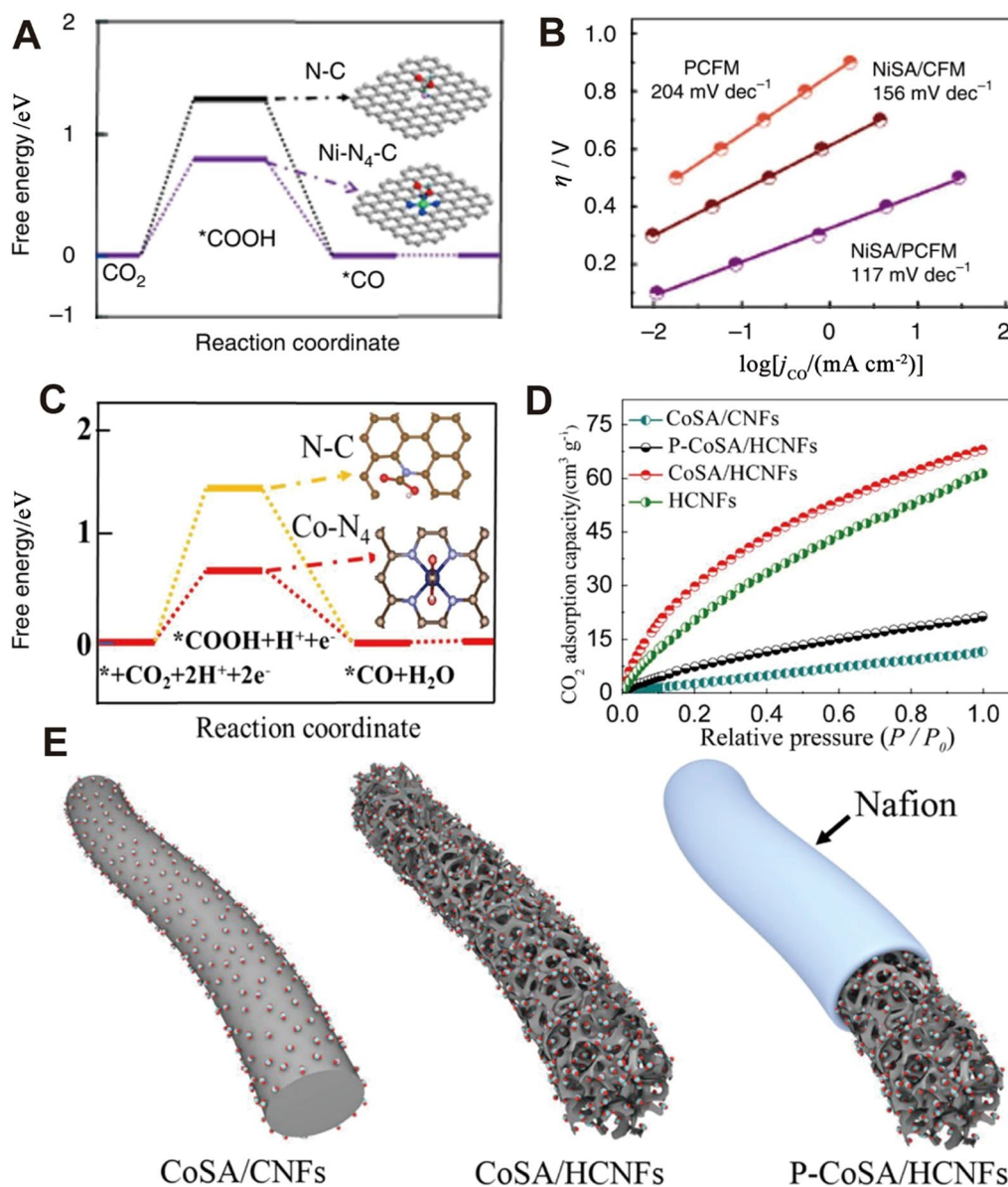


**Fig. 17** Proposed mechanism of NiSA/PCFM for CO<sub>2</sub> reduction. **A** Free energy diagram illustrating the conversion of CO<sub>2</sub> to adsorbed \*COOH intermediate on N-C and Ni-N<sub>4</sub>-C doped graphene structure. **B** Tafel plots for comparison of CO<sub>2</sub> reduction on different electrodes. Reproduced with permission from Ref. [46]. Copyright 2020, Nature

Publishing Group. **C** Free energy diagram of CO<sub>2</sub> reduction to CO on N-C and Co-N<sub>4</sub> graphene. **D** Comparison of CO<sub>2</sub> adsorption amount of various catalysts. **E** Illustration of CO<sub>2</sub> diffusion on different composites materials. Reproduced with permission from Ref. [28]. Copyright 2020, Elsevier

electrode composed of Ni single atoms coordinated with N and S atoms on carbon paper (ACP/S-N/Ni) shows an excellent catalytic activity for CO<sub>2</sub> reduction with FE of 91% for CO production at  $-0.77$  V (vs. RHE) [48]. The N<sub>3</sub>S-Ni site is the active site of the ACP/S-N/Ni SAC, which provides easy pathways for the formation of CO from CO<sub>2</sub>. The DFT calculation shows that the energy barrier for the rate-determining step of the adsorbed \*COOH intermediate is lower (2.03 eV) than the \*H intermediate (2.23 eV) at the N<sub>3</sub>S-Ni site, which justifies the high electrocatalytic activity of ACP/S-N/Ni SAC for CO<sub>2</sub> reduction. Another self-standing Ni SAC consisting of Ni single atoms coordinated with N atoms decorated in hierarchical carbon papers (Ni SAC/H-CP) exhibited superb catalytic performance for CO<sub>2</sub> to CO conversion [49]. The different Ni-N coordination numbers were formed in the Ni SAC/H-CP, such as Ni-N, Ni-N<sub>2</sub>, Ni-N<sub>3</sub> and Ni-N<sub>4</sub>, and each site has different reaction pathways for CO generation from CO<sub>2</sub>. Interestingly, Ni nanoparticles showed lower  $\Delta G$  for the CO<sub>2</sub> to \*COOH conversion than all other N-coordinated Ni sites. Moreover, the reduction of \*COOH to \*CO was endothermic at Ni nanoparticles, whereas it was exothermic at Ni-N<sub>x</sub> sites. However, the \*CO desorption requires a very high  $\Delta G$  at the surface of Ni nanoparticles compared to all other Ni-N<sub>x</sub> sites due to the high binding strength of \*CO to Ni nanoparticles, suggesting that Ni nanoparticles have low catalytic activity for CO<sub>2</sub> reduction than the Ni SACs. It is seen that if Ni dimer or trimer states are considered in Ni SAC/H-CP, the CO desorption steps are not energetically favorable at their surface, indicating that Ni dimer or trimer should not form CO from the reduction of CO<sub>2</sub>. Furthermore,  $\Delta G$  for \*H is calculated to be very high at N-N<sub>x</sub> sites, such as 1.54 eV at Ni-N<sub>4</sub>, whereas Ni nanoparticles exhibit  $-0.37$  eV for \*H formation, implying that Ni SAC consisting of Ni-N<sub>x</sub> sites facilitates CO<sub>2</sub> reduction to CO and Ni nanoparticles are more prone to HER.

Co SACs supported on carbon surfaces have shown outstanding catalytic performance for CO<sub>2</sub> reduction [35, 109, 212]. A recent study has focused on the development of free-standing Co SACs to further improve CO<sub>2</sub> reduction activity and stability [213]. For example, the Co SACs composed of Co-N<sub>4</sub> moieties were uniformly distributed on the cross-linked carbon nanofibers membrane (Co SAs/HCNFs), which was synthesized by using the electrospinning method followed by pyrolysis at high temperature. The developed Co SAs/HCNFs exhibited a high production of CO from CO<sub>2</sub> with 91% FE and CO partial current density of  $67 \text{ mA cm}^{-2}$  at  $-0.6$  V (vs. RHE) in an H-type cell. The CO<sub>2</sub> electrolysis was further evaluated in a GDE cell, which showed  $211 \text{ mA cm}^{-2}$  for CO generation with over 90% FE at  $-0.9$  V, proving its excellent catalytic performance as a potential catalyst for CO<sub>2</sub> to CO conversion on an industrial scale. The DFT calculation has also been used to explain the

outstanding catalytic activity of the self-standing Co SACs. Figure 17C displays the free energy diagram for the formation of intermediates on Co-N<sub>4</sub> and Co-C sites for the conversion of CO<sub>2</sub> to CO. The  $\Delta G$  for the synthesis of adsorbed \*COOH, which is the rate-limiting step for CO<sub>2</sub> reduction, is much higher at the N-C site (1.37 eV) than that at the Co-N<sub>4</sub> site (0.65 eV), which means extra energy is required to overcome the energy barrier at the N-C (pyridine N) site for the CO<sub>2</sub> reduction [34, 35, 87]. The formation of \*CO also shows a low  $\Delta G$  value at the Co-N<sub>4</sub> site compared to that of the N-C site, revealing that the single-atom Co is highly active for CO<sub>2</sub> reduction than the pyridine nitrogen. Moreover, the CO<sub>2</sub> adsorption capacity was performed at different Co SACs at different applied pressure reported by Yang et al. as shown in Fig. 17D [213]. It is seen that Co SAs/HCNFs has higher CO<sub>2</sub> adsorption capacity compared to all other studied catalysts, due to the existence of meso- and microporous structure in Co SAs/HCNFs, which facilitates a large ECSA and high CO<sub>2</sub> transportation to Co active sites, providing a high catalytic activity of CO<sub>2</sub> reduction. However, if the Co SACs do not possess meso and microporous channels or collapse the cross-linking structure and to use a binder to attach the catalysts to the substrate, it would lower the ECSA and block the CO<sub>2</sub> diffusion as well as hinder electron transportation (Fig. 17E). Therefore, the development of free-standing transition metal SACs with hierarchically porous structures and carbon fiber cross-linking would obtain large ECSA and abundant channels for electron and mass transportation, which could be used as effective catalysts for the reduction of CO<sub>2</sub>.

Most of the transition metal SACs, e.g., Fe, Co, Ni-based, produce CO as the primary product from the reduction of CO<sub>2</sub> except Cu-based SACs [41, 86, 92, 109, 156]. Producing multi-carbon products from CO<sub>2</sub> reduction is challenging due to the high energy barriers toward the C-C coupling formation. The linear CO<sub>2</sub> molecule interacts weakly with the Cu surface, which results in a high energy barrier for CO<sub>2</sub> activation [214–216]. However, the bent CO<sub>2</sub> can bond strongly to the Cu surface if formed, lowering the free energy barrier for the initial hydrogenation steps [215–217]. Moreover, Cu can strongly bind the CO intermediate to its surface, making a low free energy pathway for the formation of a C–C bond [218–221]. In terms of catalytic activity and stability, free-standing Cu SACs exhibit better performance than powder Cu SACs, as the binder may block some of the active sites of the powder catalysts [44, 156]. Yang et al. have synthesized Cu SAs dispersed on through-hole carbon nanofiber (Cu SAs/TCNFs) as an effective catalyst for CO<sub>2</sub> reduction with 56% FE of CO and 44% FE of CH<sub>3</sub>OH at  $-0.9$  V (vs. RHE), where Cu-N<sub>4</sub> acted as the active site for CO<sub>2</sub> activation [44]. Their developed catalyst also exhibited a 50 h long-term stability with a current density of  $\sim 90 \text{ mA cm}^{-2}$  at the same potential with almost no loss

of activity during the entire experiment, proving the excellent stability of the catalyst. The high-performance activity of Cu SAs/TCNFs toward  $\text{CO}_2$  reduction was investigated and compared with pyridine N and  $\text{Ni-N}_4$  catalysts by the DFT calculations, as shown in Fig. 18. The Cu- $\text{N}_4$  moieties embedded in graphene nanosheets as the active center of Cu SAs/TCNFs, and  $\text{Ni-N}_4$  and pyridine N-doped graphene were investigated in DFT studies (Fig. 18B). The proposed  $\text{CO}_2$  reduction reaction pathways are manifested in Fig. 18A, and the free energy diagram for  $\text{CO}_2$  to CO conversion is shown in Fig. 18C. The free energy change for the formation of  $\text{COOH}^*$  is uphill at all three catalysts, which is the rate-limiting step of  $\text{CO}_2$  reduction [113, 131, 213, 222–224]. It is seen that the  $\Delta G$  for adsorbed  $\text{COOH}^*$  was lower at the  $\text{Ni-N}_4$  (0.98 eV) system compared to those of pyridine N (1.62 eV) and Cu- $\text{N}_4$  (1.17 eV) systems. The conversion of adsorbed  $\text{COOH}^*$  to  $\text{CO}^*$  was easy at all three configurations. The  $\Delta G$  for desorption of  $\text{CO}^*$  intermediate was found to be negative at both  $\text{Ni-N}_4$  and pyridine N samples, suggesting that  $\text{CO}^*$  can easily be removed from the catalyst surface, generating CO as the product [227]. However,  $\text{CO}^*$  desorption free energy was slightly positive on the Cu- $\text{N}_4$  surface (0.12 eV), indicating that  $\text{CO}^*$  can further be reduced rather than being released as CO [133, 164, 226–231]. The formation of  $\text{C}_2$  products is obtained from the dimerization of the C1 intermediate likely  $\text{CO}^*$  with a large local concentration at the Cu surface [203, 232]. Since Cu is distributed as a single atom in the carbon matrix at Cu SAs/TCNFs, the C-C coupling route of  $\text{CO}^*$  into  $\text{C}_2$  products might be blocked [233]. Figure 18D displays the free energy diagram for the conversion of  $\text{CO}^*$  intermediate to  $\text{CH}_3\text{OH}$  on the Cu- $\text{N}_4$  system. The reduction of  $\text{COH}^*$  intermediate is the key step for the formation of  $\text{CH}_4$  and  $\text{CH}_3\text{OH}$  [185, 215, 216, 233–235]. It is seen that the formation of  $\text{CHOH}^*$  was easier than the  $\text{C}^*$  from  $\text{COH}^*$  on the Cu- $\text{N}_4$  structure (Fig. 18D). For instance,  $\Delta G$  for  $\text{COH}^*$  to  $\text{CHOH}^*$  is calculated to be  $\sim 0.86$  eV, which was much lower compared to the conversion of  $\text{COH}^*$  to  $\text{C}^*$  ( $\sim 1.88$  eV), suggesting that Cu single atoms decorated on the carbon substrate tend to produce  $\text{CH}_3\text{OH}$  instead of CH from  $\text{CO}_2$ .

## 5 Summary and Perspective

This review discusses recent developments in the use of single-atom catalysts (SACs) and their associated electrodes for electrochemical  $\text{CO}_2$  reduction. Metal-based SACs have shown high activity and selectivity for this process, as they efficiently reduce  $\text{CO}_2$  to CO, a valuable chemical intermediate. Free-standing SAC electrodes have the added advantage of being easily separated from the gas diffusion electrode cell after the reaction and can be reused. Researchers are actively exploring SACs as a sustainable and efficient

solution for  $\text{CO}_2$  reduction, a critical step toward carbon capture and utilization. Despite promising results for CO production, challenges and opportunities in the use of SACs for electrochemical  $\text{CO}_2$  reduction must be addressed.

1. Generally, due to the high surface energy, SACs tend to aggregate into larger particles under harsh operational conditions. Therefore, aggregation becomes one of the main challenges for the practical application of SACs. To date, effective methods to overcome the aggregation problem of SACs mainly include pyrolyzed M-N-C catalysts, metal-organic frameworks-derived SACs and graphene-supported SACs. However, there is an urgent need to explore more efficient and universal synthetic routes to increase the loading of active metal atoms, stabilize more SACs and prevent their agglomeration.
2. The number of exposed active sites of SACs is the extrinsic factor affecting the catalytic activity of  $\text{CO}_2$  electrochemical reduction to CO. However, preserving the accessibility and activity of the SACs inside the electrode to maximize the exposure of the active metal moieties is currently the major materials development and electrode design challenges. At present, most attempts to produce SACs have used powder or particle-like carbon supports, hence polymer binders, such as Nafion, were employed to incorporate them into the catalyst layer. The binder and inactive support particles will, inevitably, cover a fraction of the catalysts' active sites, rendering them inactive. The free-standing/self-support binder-free gas diffusion electrode design with hierarchical porous structure has the potential to overcome these issues by simply exposing more catalytic active sites, facilitating mass transport, charge transfer and electrical conductivity due to the interconnectedness of the structure, and enhancing mechanical stability due to the absence of a weak binder-catalyst-support interface. The techniques considered for the development of free-standing SAC electrodes may include the effective synthesis method, support production, electrode chemistry and fabrication and manufacturing process that will generate high form factor nano-sized materials with very good control of morphology, continuous porous structure and high utilization. A successful technology should provide a technically simple, scalable and continuous process toward large-scale production of electrodes using SACs, not only for electrochemical  $\text{CO}_2$  reduction applications but also for a wide range of electrochemical energy storage and conversion applications such as hydrogen production.
3. The development of flow reactors is necessary for practical applications of  $\text{CO}_2$  reduction. Such a cell design facilitates  $\text{CO}_2$  diffusion to catalytic active sites compared to that of H-type cells. In this regard, further study



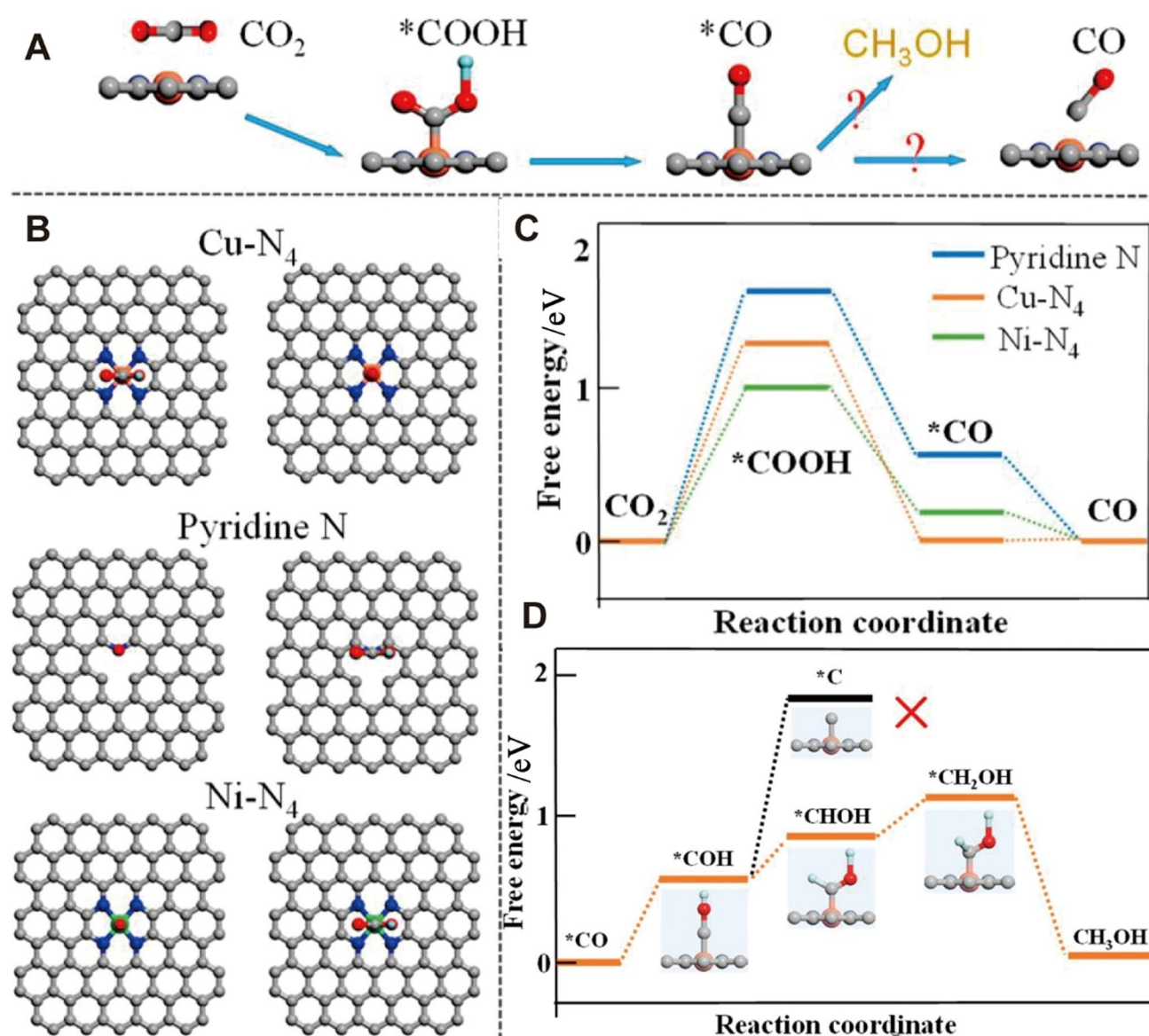


**Fig. 18** **A** Optimized atomic structures of CuSAs/TCNFs and proposed reaction paths for CO<sub>2</sub> electroreduction. **B**, **C** Free energy diagram depicting the conversion of CO<sub>2</sub> to CO on pyridine N, Ni-N<sub>4</sub> and Cu-N<sub>4</sub> structure. **D** Free energies profiles for conversion of \*CO

to CH<sub>3</sub>OH on the Cu-N<sub>4</sub> structure with orange, gray, dark blue, red and light blue spheres representing Cu, C, N, O and H atoms, respectively. **D** Reproduced with permission from Ref. [44]. Copyright 2019, American Chemical Society

is required to optimize the operating conditions such as pH, cations, temperatures and the electrode structure to integrate SACs into flow cells effectively to bring CO<sub>2</sub> reduction technology closer to practical applications, allowing attaining at a relevant industrial standard (current density > 300 mA cm<sup>-2</sup>).

4. The investigation of the correlation between structure and catalytic mechanism will shed light on the optimization and design of SACs for CO<sub>2</sub> reduction process. The well-defined structures and homogeneous active sites of SACs make them a good model for DFT calculations, particularly for the investigation with simple catalytic

pathways such as CO<sub>2</sub> reduction to CO. In addition, combining DFT calculation and advanced characterization techniques, such as XAS and HAADF-STEM, and operando technologies, such as in situ FTIR, Raman and XAS characterizations, are crucial to our deep understanding of the active sites centers, metal valence, metal coordination environment and catalytic mechanism on SACs under realistic working conditions.

**Acknowledgements** The authors acknowledge the National Research Council Canada Materials for Clean Fuels Program, the National

Research Council Canada Postdoctoral Fellowship Program and the Natural Resources Canada Office of Energy Research and Development.

**Funding** Open Access provided by National Research Council Canada.

## Declarations

**Conflict of interest** Lei Zhang is an editorial board member for *Electrochemical Energy Reviews* and was not involved in the editorial review or the decision to publish this article. All authors declare that there are no competing interests.

**Open Access** This article is licensed under a Creative Commons Attribution 4.0 International License, which permits use, sharing, adaptation, distribution and reproduction in any medium or format, as long as you give appropriate credit to the original author(s) and the source, provide a link to the Creative Commons licence, and indicate if changes were made. The images or other third party material in this article are included in the article's Creative Commons licence, unless indicated otherwise in a credit line to the material. If material is not included in the article's Creative Commons licence and your intended use is not permitted by statutory regulation or exceeds the permitted use, you will need to obtain permission directly from the copyright holder. To view a copy of this licence, visit <http://creativecommons.org/licenses/by/4.0/>.

## References

- Spurgeon, J.M., Kumar, B.: A comparative technoeconomic analysis of pathways for commercial electrochemical CO<sub>2</sub> reduction to liquid products. *Energy Environ. Sci.* **11**, 1536–1551 (2018). <https://doi.org/10.1039/c8ee00097b>
- Jouny, M., Luc, W., Jiao, F.: General techno-economic analysis of CO<sub>2</sub> electrolysis systems. *Ind. Eng. Chem. Res.* **57**, 2165–2177 (2018). <https://doi.org/10.1021/acs.iecr.7b03514>
- Li, X.F., Han, S.G., Wu, W.M., et al.: Convergent paired electrosynthesis of dimethyl carbonate from carbon dioxide enabled by designing the superstructure of axial oxygen coordinated nickel single-atom catalysts. *Energy Environ. Sci.* **16**, 502–512 (2023). <https://doi.org/10.1039/d2ee03022e>
- Ju, W.B., Jiang, F.Z., Ma, H., et al.: Electrocatalytic reduction of gaseous CO<sub>2</sub> to CO on Sn/Cu-nanofiber-based gas diffusion electrodes. *Adv. Energy Mater.* **9**, 1901514 (2019). <https://doi.org/10.1002/aenm.201901514>
- Kou, Z.K., Li, X., Wang, T.T., et al.: Fundamentals, on-going advances and challenges of electrochemical carbon dioxide reduction. *Electrochem. Energy Rev.* **5**, 82–111 (2022). <https://doi.org/10.1007/s41918-021-00096-5>
- Ren, S., Cao, X., Jiang, Z.N., et al.: Single-atom catalysts for electrochemical applications. *Chem. Commun.* **59**, 2560–2570 (2023). <https://doi.org/10.1039/d3cc00005b>
- Liu, M.M., Wang, L.L., Zhao, K.N., et al.: Atomically dispersed metal catalysts for the oxygen reduction reaction: synthesis, characterization, reaction mechanisms and electrochemical energy applications. *Energy Environ. Sci.* **12**, 2890–2923 (2019). <https://doi.org/10.1039/c9ee01722d>
- Mitchell, S., Pérez-Ramírez, J.: Single atom catalysis: a decade of stunning progress and the promise for a bright future. *Nat. Commun.* **11**, 4302 (2020). <https://doi.org/10.1038/s41467-020-18182-5>
- Ma, W., Deng, Z., Zhang, X.J., et al.: Regulating the electronic structure of single-atom catalysts for electrochemical energy conversion. *J. Mater. Chem. A* (2023). <https://doi.org/10.1039/d3ta00156c>
- Zhao, C.M., Dai, X.Y., Yao, T., et al.: Ionic exchange of metal-organic frameworks to access single nickel sites for efficient electroreduction of CO<sub>2</sub>. *J. Am. Chem. Soc.* **139**, 8078–8081 (2017). <https://doi.org/10.1021/jacs.7b02736>
- An, B.B., Zhou, J.S., Duan, L.J., et al.: Liquid nitrogen sources assisting gram-scale production of single-atom catalysts for electrochemical carbon dioxide reduction. *Adv. Sci.* **10**, 2205639 (2023). <https://doi.org/10.1002/advs.202205639>
- Cui, X.J., Li, W., Ryabchuk, P., et al.: Bridging homogeneous and heterogeneous catalysis by heterogeneous single-metal-site catalysts. *Nat. Catal.* **1**, 385–397 (2018). <https://doi.org/10.1038/s41929-018-0090-9>
- Chen, Y.Q., Zhang, J.R., Yang, L.J., et al.: Recent advances in non-precious metal-nitrogen-carbon single-site catalysts for CO<sub>2</sub> electroreduction reaction to CO. *Electrochem. Energy Rev.* **5**, 1–31 (2022). <https://doi.org/10.1007/s41918-022-00156-4>
- Fei, H.L., Dong, J.C., Arellano-Jiménez, M.J., et al.: Atomic cobalt on nitrogen-doped graphene for hydrogen generation. *Nat. Commun.* **6**, 8668 (2015). <https://doi.org/10.1038/ncomm59668>
- Yang, H.B., Hung, S.F., Liu, S., et al.: Atomically dispersed Ni(i) as the active site for electrochemical CO<sub>2</sub> reduction. *Nat. Energy* **3**, 140–147 (2018). <https://doi.org/10.1038/s41560-017-0078-8>
- Hai, X., Xi, S.B., Mitchell, S., et al.: Scalable two-step annealing method for preparing ultra-high-density single-atom catalyst libraries. *Nat. Nanotechnol.* **17**, 174–181 (2022). <https://doi.org/10.1038/s41565-021-01022-y>
- Cheng, Y., Zhao, S.Y., Johannessen, B., et al.: Single-atom catalysts: atomically dispersed transition metals on carbon nanotubes with ultrahigh loading for selective electrochemical carbon dioxide reduction. *Adv. Mater.* **30**, 1870088 (2018). <https://doi.org/10.1002/adma.201870088>
- Li, Y., Adli, N.M., Shan, W.T., et al.: Atomically dispersed single Ni site catalysts for high-efficiency CO<sub>2</sub> electroreduction at industrial-level current densities. *Energy Environ. Sci.* **15**, 2108–2119 (2022). <https://doi.org/10.1039/d2ee00318j>
- Yang, H.Z., Shang, L., Zhang, Q.H., et al.: A universal ligand mediated method for large scale synthesis of transition metal single atom catalysts. *Nat. Commun.* **10**, 4585 (2019). <https://doi.org/10.1038/s41467-019-12510-0>
- Nguyen, T.N., Salehi, M., Le, Q.V., et al.: Fundamentals of electrochemical CO<sub>2</sub> reduction on single-metal-atom catalysts. *ACS Catal.* **10**, 10068–10095 (2020). <https://doi.org/10.1021/acscatal.0c02643>
- Cheng, Y., Yang, S., Jiang, S.P., et al.: Supported single atoms as new class of catalysts for electrochemical reduction of carbon dioxide. *Small Methods* **3**, 1800440 (2019)
- Creissen, C.E., Fontecave, M.: Keeping sight of copper in single-atom catalysts for electrochemical carbon dioxide reduction. *Nat. Commun.* **13**, 2280 (2022). <https://doi.org/10.1038/s41467-022-30027-x>
- Zhang, Z.D., Wang, D.S.: Single-atom catalysts: stimulating electrochemical CO<sub>2</sub> reduction reaction in the industrial era. *J. Mater. Chem. A* **10**, 5863–5877 (2022). <https://doi.org/10.1039/d1ta07778c>
- Jhong, H.R.M., Brushett, F.R., Yin, L.L., et al.: Combining structural and electrochemical analysis of electrodes using micro-computed tomography and a microfluidic fuel cell. *J. Electrochem. Soc.* **159**, B292–B298 (2012). <https://doi.org/10.1149/2.033203jes>
- Nwabara, U.O., Cofell, E.R., Verma, S., et al.: Durable cathodes and electrolyzers for the efficient aqueous electrochemical reduction of CO<sub>2</sub>. *Chemsuschem* **13**, 855–875 (2020). <https://doi.org/10.1002/cssc.201902933>

26. Ji, D.X., Fan, L., Li, L.L., et al.: Atomically transition metals on self-supported porous carbon flake arrays as binder-free air cathode for wearable zinc-air batteries. *Adv. Mater.* **31**, 1808267 (2019). <https://doi.org/10.1002/adma.201808267>
27. Xie, W.F., Song, Y.K., Li, S.J., et al.: Single-atomic-Co electrocatalysts with self-supported architecture toward oxygen-involved reaction. *Adv. Funct. Mater.* **29**, 1906477 (2019). <https://doi.org/10.1002/adfm.201906477>
28. Yang, H.P., Lin, Q., Wu, Y., et al.: Highly efficient utilization of single atoms via constructing 3D and free-standing electrodes for CO<sub>2</sub> reduction with ultrahigh current density. *Nano Energy* **70**, 104454 (2020). <https://doi.org/10.1016/j.nanoen.2020.104454>
29. He, Y.H., Liu, S.W., Priest, C., et al.: Atomically dispersed metal-nitrogen-carbon catalysts for fuel cells: advances in catalyst design, electrode performance, and durability improvement. *Chem. Soc. Rev.* **49**, 3484–3524 (2020). <https://doi.org/10.1039/c9cs00903e>
30. Zhang, N.Q., Zhang, X.X., Tao, L., et al.: Silver single-atom catalyst for efficient electrochemical CO<sub>2</sub> reduction synthesized from thermal transformation and surface reconstruction. *Angew. Chem. Int. Ed.* **60**, 6170–6176 (2021). <https://doi.org/10.1002/anie.202014718>
31. Li, Y.F., Chen, C., Cao, R., et al.: Dual-atom Ag<sub>2</sub>/graphene catalyst for efficient electroreduction of CO<sub>2</sub> to CO. *Appl. Catal. B Environ.* **268**, 118747 (2020). <https://doi.org/10.1016/j.apcatb.2020.118747>
32. Jiang, K., Siahrostami, S., Zheng, T.T., et al.: Isolated Ni single atoms in graphene nanosheets for high-performance CO<sub>2</sub> reduction. *Energy Environ. Sci.* **11**, 893–903 (2018). <https://doi.org/10.1039/c7ee03245e>
33. Lu, P.L., Yang, Y.J., Yao, J.N., et al.: Facile synthesis of single-nickel-atomic dispersed N-doped carbon framework for efficient electrochemical CO<sub>2</sub> reduction. *Appl. Catal. B Environ.* **241**, 113–119 (2019). <https://doi.org/10.1016/j.apcatb.2018.09.025>
34. Wang, X.Q., Chen, Z., Zhao, X.Y., et al.: Regulation of coordination number over single Co sites: triggering the efficient electroreduction of CO<sub>2</sub>. *Angew. Chem. Int. Ed.* **57**, 1944–1948 (2018). <https://doi.org/10.1002/anie.201712451>
35. Pan, Y., Lin, R., Chen, Y.J., et al.: Design of single-atom Co-N<sub>5</sub> catalytic site: a robust electrocatalyst for CO<sub>2</sub> reduction with nearly 100% CO selectivity and remarkable stability. *J. Am. Chem. Soc.* **140**, 4218–4221 (2018). <https://doi.org/10.1021/jacs.8b00814>
36. Li, S.M., Zhao, S.Q., Lu, X.Y., et al.: Low-valence Zn<sup>δ+</sup> (0<δ<2) single-atom material as highly efficient electrocatalyst for CO<sub>2</sub> reduction. *Angew. Chem. Int. Ed.* **60**, 22826–22832 (2021). <https://doi.org/10.1002/anie.202107550>
37. Liu, J.J., Yang, D., Zhou, Y., et al.: Tricycloquinazoline-based 2D conductive metal-organic frameworks as promising electrocatalysts for CO<sub>2</sub> reduction. *Angew. Chem. Int. Ed.* **60**, 14473–14479 (2021). <https://doi.org/10.1002/anie.202103398>
38. Wang, X.Y., Sang, X.H., Dong, C.L., et al.: Proton capture strategy for enhancing electrochemical CO<sub>2</sub> reduction on atomically dispersed metal-nitrogen active sites. *Angew. Chem. Int. Ed.* **60**, 11959–11965 (2021). <https://doi.org/10.1002/anie.202100011>
39. Yang, F., Song, P., Liu, X.Z., et al.: Highly efficient CO<sub>2</sub> electroreduction on ZnN<sub>4</sub>-based single-atom catalyst. *Angew. Chem. Int. Ed.* **57**, 12303–12307 (2018). <https://doi.org/10.1002/anie.201805871>
40. Jeong, H.Y., Balamurugan, M., Choutipalli, V.S.K., et al.: Achieving highly efficient CO<sub>2</sub> to CO electroreduction exceeding 300 mA cm<sup>-2</sup> with single-atom nickel electrocatalysts. *J. Mater. Chem. A* **7**, 10651–10661 (2019). <https://doi.org/10.1039/c9ta02405k>
41. Zheng, T.T., Jiang, K., Ta, N., et al.: Large-scale and highly selective CO<sub>2</sub> electrocatalytic reduction on nickel single-atom catalyst. *Joule* **3**, 265–278 (2019). <https://doi.org/10.1016/j.joule.2018.10.015>
42. Wang, Y., Jiang, Z., Zhang, X., et al.: Metal phthalocyanine-derived single-atom catalysts for selective CO<sub>2</sub> electroreduction under high current densities. *ACS Appl. Mater. Interfaces* **12**, 33795–33802 (2020). <https://doi.org/10.1021/acsami.0c08940>
43. Wen, C.F., Mao, F.X., Liu, Y.W., et al.: Nitrogen-stabilized low-valent Ni motifs for efficient CO<sub>2</sub> electrocatalysis. *ACS Catal.* **10**, 1086–1093 (2020). <https://doi.org/10.1021/acscatal.9b02978>
44. Yang, H.P., Wu, Y., Li, G.D., et al.: Scalable production of efficient single-atom copper decorated carbon membranes for CO<sub>2</sub> electroreduction to methanol. *J. Am. Chem. Soc.* **141**, 12717–12723 (2019). <https://doi.org/10.1021/jacs.9b04907>
45. Zhang, H.N., Li, J., Xi, S.B., et al.: A graphene-supported single-atom FeN<sub>5</sub> catalytic site for efficient electrochemical CO<sub>2</sub> reduction. *Angew. Chem. Int. Ed.* **58**, 14871–14876 (2019). <https://doi.org/10.1002/anie.201906079>
46. Yang, H.P., Lin, Q., Zhang, C., et al.: Carbon dioxide electroreduction on single-atom nickel decorated carbon membranes with industry compatible current densities. *Nat. Commun.* **11**, 593 (2020). <https://doi.org/10.1038/s41467-020-14402-0>
47. Rong, X., Wang, H.J., Lu, X.L., et al.: Controlled synthesis of a vacancy-defect single-atom catalyst for boosting CO<sub>2</sub> electroreduction. *Angew. Chem. Int. Ed.* **59**, 1961–1965 (2020). <https://doi.org/10.1002/anie.201912458>
48. Li, S.M., Ceccato, M., Lu, X.Y., et al.: Incorporation of nickel single atoms into carbon paper as self-standing electrocatalyst for CO<sub>2</sub> reduction. *J. Mater. Chem. A* **9**, 1583–1592 (2021). <https://doi.org/10.1039/d0ta08433f>
49. Zhao, C.M., Wang, Y., Li, Z.J., et al.: Solid-diffusion synthesis of single-atom catalysts directly from bulk metal for efficient CO<sub>2</sub> reduction. *Joule* **3**, 584–594 (2019). <https://doi.org/10.1016/j.joule.2018.11.008>
50. Shang, H.S., Wang, T., Pei, J.J., et al.: Design of a single-atom indium<sup>δ+</sup>-N<sub>4</sub> interface for efficient electroreduction of CO<sub>2</sub> to formate. *Angew. Chem. Int. Ed.* **59**, 22465–22469 (2020). <https://doi.org/10.1002/anie.202010903>
51. Chen, D.T., Zhang, L.H., Du, J., et al.: A tandem strategy for enhancing electrochemical CO<sub>2</sub> reduction activity of single-atom Cu-S<sub>3</sub>N<sub>3</sub> catalysts via integration with Cu nanoclusters. *Angew. Chem. Int. Ed.* **60**, 24022–24027 (2021). <https://doi.org/10.1002/anie.202109579>
52. Wu, Y.H., Chen, C.J., Yan, X.P., et al.: Boosting CO<sub>2</sub> electroreduction over a cadmium single-atom catalyst by tuning of the axial coordination structure. *Angew. Chem. Int. Ed.* **60**, 20803–20810 (2021). <https://doi.org/10.1002/anie.202105263>
53. Han, L.L., Song, S.J., Liu, M.J., et al.: Stable and efficient single-atom Zn catalyst for CO<sub>2</sub> reduction to CH<sub>4</sub>. *J. Am. Chem. Soc.* **142**, 12563–12567 (2020). <https://doi.org/10.1021/jacs.9b12111>
54. Sui, R., Pei, J.J., Fang, J.J., et al.: Engineering Ag-N<sub>x</sub> single-atom sites on porous concave N-doped carbon for boosting CO<sub>2</sub> electroreduction. *ACS Appl. Mater. Interfaces* **13**, 17736–17744 (2021). <https://doi.org/10.1021/acscami.1c03638>
55. Wei, S.M., Jiang, X.X., He, C.Y., et al.: Construction of single-atom copper sites with low coordination number for efficient CO<sub>2</sub> electroreduction to CH<sub>4</sub>. *J. Mater. Chem. A* **10**, 6187–6192 (2022). <https://doi.org/10.1039/d1ta08494a>
56. Mou, K.W., Chen, Z.P., Zhang, X.X., et al.: Highly efficient electroreduction of CO<sub>2</sub> on nickel single-atom catalysts: atom trapping and nitrogen anchoring. *Small* **15**, 1903668 (2019). <https://doi.org/10.1002/sml.201903668>
57. Chen, Z.P., Zhang, X.X., Liu, W., et al.: Amination strategy to boost the CO<sub>2</sub> electroreduction current density of M–N/C single-atom catalysts to the industrial application level. *Energy Environ. Sci.* **14**, 2349–2356 (2021). <https://doi.org/10.1039/d0ee04052e>



58. Pan, F.P., Li, B.Y., Sarnello, E., et al.: Pore-edge tailoring of single-atom iron-nitrogen sites on graphene for enhanced CO<sub>2</sub> reduction. *ACS Catal.* **10**, 10803–10811 (2020). <https://doi.org/10.1021/acscatal.0c02499>
59. Hossain, M.N., Choueiri, R.M., Abner, S., et al.: Electrochemical reduction of carbon dioxide at TiO<sub>2</sub>/Au nanocomposites. *ACS Appl. Mater. Interfaces* **14**, 51889–51899 (2022). <https://doi.org/10.1021/acscami.2c14368>
60. Luna, P.D., Hahn, C., Higgins, D., et al.: What would it take for renewably powered electrosynthesis to displace petrochemical processes? *Science* **364**, eaav3506 (2019). <https://doi.org/10.1126/science.aav3506>
61. Abdinejad, M., Ferrag, C., Hossain, M.N., et al.: Capture and electroreduction of CO<sub>2</sub> using highly efficient bimetallic Pd-Ag aerogels paired with carbon nanotubes. *J. Mater. Chem. A* **9**, 12870–12877 (2021). <https://doi.org/10.1039/d1ta01834e>
62. Nur Hossain, M., Chen, S., Chen, A.C.: Thermal-assisted synthesis of unique Cu nanodendrites for the efficient electrochemical reduction of CO<sub>2</sub>. *Appl. Catal. B Environ.* **259**, 118096 (2019). <https://doi.org/10.1016/j.apcatb.2019.118096>
63. Zang, Y.P., Wei, P.F., Li, H.F., et al.: Catalyst design for electrolytic CO<sub>2</sub> reduction toward low-carbon fuels and chemicals. *Electrochem. Energy Rev.* **5**, 1–30 (2022). <https://doi.org/10.1007/s41918-022-00140-y>
64. Hossain, M.N., Liu, Z.G., Wen, J.L., et al.: Enhanced catalytic activity of nanoporous Au for the efficient electrochemical reduction of carbon dioxide. *Appl. Catal. B Environ.* **236**, 483–489 (2018). <https://doi.org/10.1016/j.apcatb.2018.05.053>
65. Li, C.W., Ciston, J., Kanan, M.W.: Electroreduction of carbon monoxide to liquid fuel on oxide-derived nanocrystalline copper. *Nature* **508**, 504–507 (2014). <https://doi.org/10.1038/nature13249>
66. Hossain, M.N., Ahmad, S., Kraatz, H.B.: Synthesis and electrochemical study of coinage metal nanodendrites for hydrogen evolution reaction. *Int. J. Hydrog. Energy* **46**, 2007–2017 (2021). <https://doi.org/10.1016/j.ijhydene.2020.10.057>
67. Abdinejad, M., Hossain, M.N., Kraatz, H.B.: Homogeneous and heterogeneous molecular catalysts for electrochemical reduction of carbon dioxide. *RSC Adv.* **10**, 38013–38023 (2020). <https://doi.org/10.1039/d0ra07973a>
68. Zhu, C.Z., Fu, S.F., Shi, Q.R., et al.: Single-atom electrocatalysts. *Angew. Chem. Int. Ed.* **56**, 13944–13960 (2017). <https://doi.org/10.1002/anie.201703864>
69. Wang, X.D., Hu, Q., Li, G.D., et al.: Recent advances and perspectives of electrochemical CO<sub>2</sub> reduction toward C<sub>2+</sub> products on Cu-based catalysts. *Electrochem. Energy Rev.* **5**, 1–44 (2022). <https://doi.org/10.1007/s41918-022-00171-5>
70. Han, S.T., Jia, S.Q., Xia, W., et al.: A new strategy for mass production of single-atom catalysts for high performance of CO<sub>2</sub> electrochemical reduction. *Chem. Eng. J.* **455**, 140595 (2023). <https://doi.org/10.1016/j.cej.2022.140595>
71. Zhang, Z.D., Zhu, J.X., Chen, S.H., et al.: Liquid fluxional Ga single atom catalysts for efficient electrochemical CO<sub>2</sub> reduction. *Angew. Chem. Int. Ed.* **135**, e202215136 (2023). <https://doi.org/10.1002/ange.202215136>
72. Zhai, S.L., Sun, J.K., Sun, L., et al.: Heteronuclear dual single-atom catalysts for ambient conversion of CO<sub>2</sub> from air to formate. *ACS Catal.* **13**, 3915–3924 (2023). <https://doi.org/10.1021/acscatal.2c06033>
73. Dong, W.F., Zhang, N., Li, S.X., et al.: A Mn single atom catalyst with Mn-N<sub>2</sub>O<sub>2</sub> sites integrated into carbon nanosheets for efficient electrocatalytic CO<sub>2</sub> reduction. *J. Mater. Chem. A* **10**, 10892–10901 (2022). <https://doi.org/10.1039/d2ta01285e>
74. Chen, P.Z., Zhou, T.P., Xing, L.L., et al.: Atomically dispersed iron-nitrogen species as electrocatalysts for bifunctional oxygen evolution and reduction reactions. *Angew. Chem. Int. Ed.* **56**, 610–614 (2017). <https://doi.org/10.1002/anie.201610119>
75. He, Q., Lee, J.H., Liu, D.B., et al.: Accelerating CO<sub>2</sub> electroreduction to CO over Pd single-atom catalyst. *Adv. Funct. Mater.* **30**, 2000407 (2020). <https://doi.org/10.1002/adfm.202000407>
76. Mistry, H., Reske, R., Zeng, Z.H., et al.: Exceptional size-dependent activity enhancement in the electroreduction of CO<sub>2</sub> over Au nanoparticles. *J. Am. Chem. Soc.* **136**, 16473–16476 (2014). <https://doi.org/10.1021/ja508879j>
77. Li, M.H., Wang, H.F., Luo, W., et al.: Heterogeneous single-atom catalysts for electrochemical CO<sub>2</sub> reduction reaction. *Adv. Mater.* **32**, 2001848 (2020). <https://doi.org/10.1002/adma.202001848>
78. Stambula, S., Gauquelin, N., Bugnet, M., et al.: Chemical structure of nitrogen-doped graphene with single platinum atoms and atomic clusters as a platform for the PEMFC electrode. *J. Phys. Chem. C* **118**, 3890–3900 (2014). <https://doi.org/10.1021/jp408979h>
79. Zhang, Z.R., Feng, C., Liu, C.X., et al.: Electrochemical deposition as a universal route for fabricating single-atom catalysts. *Nat. Commun.* **11**, 1215 (2020). <https://doi.org/10.1038/s41467-020-14917-6>
80. Leverett, J., Tran-Phu, T., Yuwono, J.A., et al.: Tuning the coordination structure of Cu-N-C single atom catalysts for simultaneous electrochemical reduction of CO<sub>2</sub> and NO<sub>3</sub><sup>−</sup> to urea. *Adv. Energy Mater.* **12**, 2201500 (2022). <https://doi.org/10.1002/aenm.202201500>
81. Liu, Z.G., Hossain, M.N., Wen, J.L., et al.: Copper decorated with nanoporous gold by galvanic displacement acts as an efficient electrocatalyst for the electrochemical reduction of CO<sub>2</sub>. *Nanoscale* **13**, 1155–1163 (2021). <https://doi.org/10.1039/d0nr08138h>
82. Qiao, J.L., Liu, Y.Y., Hong, F., et al.: A review of catalysts for the electroreduction of carbon dioxide to produce low-carbon fuels. *Chem. Soc. Rev.* **43**, 631–675 (2014). <https://doi.org/10.1039/c3cs60323g>
83. Hossain, M.N., Wen, J.L., Konda, S.K., et al.: Electrochemical and FTIR spectroscopic study of CO<sub>2</sub> reduction at a nanostructured Cu/reduced graphene oxide thin film. *Electrochem. Commun.* **82**, 16–20 (2017). <https://doi.org/10.1016/j.elecom.2017.07.006>
84. Hou, P.F., Huang, Y.H., Ma, F., et al.: S and N coordinated single-atom catalysts for electrochemical CO<sub>2</sub> reduction with superior activity and selectivity. *Appl. Surf. Sci.* **619**, 156747 (2023). <https://doi.org/10.1016/j.apsusc.2023.156747>
85. Chen, X.Y., Liu, W., Sun, Y.X., et al.: KOH-enabled axial-oxygen coordinated Ni single-atom catalyst for efficient electrocatalytic CO<sub>2</sub> reduction. *Small Methods* **7**, 2201311 (2023). <https://doi.org/10.1002/smt.202201311>
86. Yan, C.C., Li, H.B., Ye, Y.F., et al.: Coordinatively unsaturated nickel-nitrogen sites towards selective and high-rate CO<sub>2</sub> electroreduction. *Energy Environ. Sci.* **11**, 1204–1210 (2018). <https://doi.org/10.1039/c8ee00133b>
87. Pan, F.P., Zhang, H.G., Liu, K.X., et al.: Unveiling active sites of CO<sub>2</sub> reduction on nitrogen-coordinated and atomically dispersed iron and cobalt catalysts. *ACS Catal.* **8**, 3116–3122 (2018). <https://doi.org/10.1021/acscatal.8b00398>
88. Li, L., Jiang, Z., Li, Y.Y., et al.: Regulating morphological features of nickel single-atom catalysts for selective and enhanced electroreduction of CO<sub>2</sub>. *Small Methods* **7**, 2201213 (2023). <https://doi.org/10.1002/smt.202201213>
89. Li, X.G., Bi, W.T., Chen, M.L., et al.: Exclusive Ni-N<sub>4</sub> sites realize near-unity CO selectivity for electrochemical CO<sub>2</sub> reduction. *J. Am. Chem. Soc.* **139**, 14889–14892 (2017). <https://doi.org/10.1021/jacs.7b09074>



90. Xu, C.C., Vasileff, A., Wang, D., et al.: Synergistic catalysis between atomically dispersed Fe and a pyrrolic-N-C framework for CO<sub>2</sub> electroreduction. *Nanoscale Horiz.* **4**, 1411–1415 (2019). <https://doi.org/10.1039/c9nh00361d>
91. Lei, C.J., Wang, Y., Hou, Y., et al.: Efficient alkaline hydrogen evolution on atomically dispersed Ni-N<sub>x</sub> Species anchored porous carbon with embedded Ni nanoparticles by accelerating water dissociation kinetics. *Energy Environ. Sci.* **12**, 149–156 (2019). <https://doi.org/10.1039/c8ee01841c>
92. Gu, J., Hsu, C.S., Bai, L.C., et al.: Atomically dispersed Fe<sup>3+</sup> sites catalyze efficient CO<sub>2</sub> electroreduction to CO. *Sci.* **364**, 1091–1094 (2019). <https://doi.org/10.1126/science.aaw7515>
93. Zhang, H.N., Li, J., Xi, S.B., et al.: A graphene-supported single-atom FeN<sub>5</sub> catalytic site for efficient electrochemical CO<sub>2</sub> reduction. *Angew. Chem. Int. Ed.* **131**, 15013–15018 (2019). <https://doi.org/10.1002/ange.201906079>
94. Lakshmanan, K., Huang, W.H., Chala, S.A., et al.: Highly active oxygen coordinated configuration of Fe single-atom catalyst toward electrochemical reduction of CO<sub>2</sub> into multi-carbon products. *Adv. Funct. Mater.* **32**, 2109310 (2022). <https://doi.org/10.1002/adfm.202109310>
95. Guo, Y., Yang, H.J., Zhou, X., et al.: Electrocatalytic reduction of CO<sub>2</sub> to CO with 100% faradaic efficiency by using pyrolyzed zeolitic imidazolate frameworks supported on carbon nanotube networks. *J. Mater. Chem. A* **5**, 24867–24873 (2017). <https://doi.org/10.1039/c7ta08431e>
96. Li, X.N., Yang, X.F., Zhang, J.M., et al.: In situ/operando techniques for characterization of single-atom catalysts. *ACS Catal.* **9**, 2521–2531 (2019). <https://doi.org/10.1021/acscatal.8b04937>
97. Liu, S., Yang, H.B., Hung, S.F., et al.: Inside cover: elucidating the electrocatalytic CO<sub>2</sub> reduction reaction over a model single-atom nickel catalyst. *Angew. Chem. Int. Ed.* **59**, 510 (2020). <https://doi.org/10.1002/anie.201915193>
98. Fei, H.L., Dong, J.C., Feng, Y.X., et al.: General synthesis and definitive structural identification of MN<sub>4</sub>C<sub>4</sub> single-atom catalysts with tunable electrocatalytic activities. *Nat. Catal.* **1**, 63–72 (2018). <https://doi.org/10.1038/s41929-017-0008-y>
99. Xiao, M.L., Zhu, J.B., Ma, L., et al.: Microporous framework induced synthesis of single-atom dispersed Fe-N-C acidic ORR catalyst and its in situ reduced Fe-N<sub>4</sub> active site identification revealed by X-ray absorption spectroscopy. *ACS Catal.* **8**, 2824–2832 (2018). <https://doi.org/10.1021/acscatal.8b00138>
100. Zhao, Y., Liang, J.J., Wang, C.Y., et al.: Tunable and efficient tin modified nitrogen-doped carbon nanofibers for electrochemical reduction of aqueous carbon dioxide. *Adv. Energy Mater.* **8**, 1702524 (2018). <https://doi.org/10.1002/aenm.201702524>
101. Qu, Y.T., Wang, L.G., Li, Z.J., et al.: Single-atom catalysts: ambient synthesis of single-atom catalysts from bulk metal via trapping of atoms by surface dangling bonds. *Adv. Mater.* **31**, 1970316 (2019). <https://doi.org/10.1002/adma.201970316>
102. Li, K., Zhang, S.B., Zhang, X.L., et al.: Atomic tuning of single-atom Fe-N-C catalysts with phosphorus for robust electrochemical CO<sub>2</sub> reduction. *Nano Lett.* **22**, 1557–1565 (2022). <https://doi.org/10.1021/acs.nanolett.1c04382>
103. Pan, F.P., Li, B.Y., Sarnello, E., et al.: Atomically dispersed iron-nitrogen sites on hierarchically mesoporous carbon nanotube and graphene nanoribbon networks for CO<sub>2</sub> reduction. *ACS Nano* **14**, 5506–5516 (2020). <https://doi.org/10.1021/acsnano.9b09658>
104. Chen, Y.B., Zou, L.L., Liu, H., et al.: Fe and N co-doped porous carbon nanospheres with high density of active sites for efficient CO<sub>2</sub> electroreduction. *J. Phys. Chem. C* **123**, 16651–16659 (2019). <https://doi.org/10.1021/acs.jpcc.9b02195>
105. Zhang, Y., Jiao, L., Yang, W.J., et al.: Rational fabrication of low-coordinate single-atom Ni electrocatalysts by MOFs for highly selective CO<sub>2</sub> reduction. *Angew. Chem. Int. Ed.* **60**, 7607–7611 (2021). <https://doi.org/10.1002/anie.202016219>
106. Fan, Q., Hou, P.F., Choi, C., et al.: Activation of Ni particles into single Ni-N atoms for efficient electrochemical reduction of CO<sub>2</sub>. *Adv. Energy Mater.* **10**, 1903068 (2020). <https://doi.org/10.1002/aenm.201903068>
107. Zhu, W.J., Zhang, L., Liu, S.H., et al.: Enhanced CO<sub>2</sub> electroreduction on neighboring Zn/Co monomers by electronic effect. *Angew. Chem. Int. Ed.* **132**, 12764–12768 (2020). <https://doi.org/10.1002/ange.201916218>
108. Hao, Z.J., Chen, J.X., Zhang, D.F., et al.: Coupling effects of Zn single atom and high curvature supports for improved performance of CO<sub>2</sub> reduction. *Sci. Bull.* **66**, 1649–1658 (2021). <https://doi.org/10.1016/j.scib.2021.04.020>
109. Geng, Z.G., Cao, Y.J., Chen, W.X., et al.: Regulating the coordination environment of Co single atoms for achieving efficient electrocatalytic activity in CO<sub>2</sub> reduction. *Appl. Catal. B Environ.* **240**, 234–240 (2019). <https://doi.org/10.1016/j.apcatb.2018.08.075>
110. Zhu, D.D., Liu, J.L., Qiao, S.Z.: Recent advances in inorganic heterogeneous electrocatalysts for reduction of carbon dioxide. *Adv. Mater.* **28**, 3423–3452 (2016). <https://doi.org/10.1002/adma.201504766>
111. Zhang, L., Zhao, Z.J., Gong, J.L.: Nanostructured materials for heterogeneous electrocatalytic CO<sub>2</sub> reduction and their related reaction mechanisms. *Angew. Chem. Int. Ed.* **56**, 11326–11353 (2017). <https://doi.org/10.1002/anie.201612214>
112. Hossain, M.N.: Electrochemical reduction of carbon dioxide on nanostructured catalysts. Lakehead University (2018)
113. Liu, M., Pang, Y.J., Zhang, B., et al.: Enhanced electrocatalytic CO<sub>2</sub> reduction via field-induced reagent concentration. *Nature* **537**, 382–386 (2016). <https://doi.org/10.1038/nature19060>
114. Sheng, W.C., Kattel, S., Yao, S.Y., et al.: Electrochemical reduction of CO<sub>2</sub> to synthesis gas with controlled CO/H<sub>2</sub> ratios. *Energy Environ. Sci.* **10**, 1180–1185 (2017). <https://doi.org/10.1039/c7ee00071e>
115. Xun, W., Yang, X., Jiang, Q.S., et al.: Single-atom-anchored two-dimensional MoSi<sub>2</sub>N<sub>4</sub> monolayers for efficient electroreduction of CO<sub>2</sub> to formic acid and methane. *ACS Appl. Energy Mater.* **6**, 3236–3243 (2023). <https://doi.org/10.1021/acsaem.2c03687>
116. Kim, C., Jeon, H.S., Eom, T., et al.: Achieving selective and efficient electrocatalytic activity for CO<sub>2</sub> reduction using immobilized silver nanoparticles. *J. Am. Chem. Soc.* **137**, 13844–13850 (2015). <https://doi.org/10.1021/jacs.5b06568>
117. Guo, W., Shim, K., Ngome, F.O.O., et al.: Highly active coral-like porous silver for electrochemical reduction of CO<sub>2</sub> to CO. *J. CO<sub>2</sub> Util.* **41**, 101242 (2020). <https://doi.org/10.1016/j.jcou.2020.101242>
118. Fan, T.T., Wu, Q.L., Yang, Z., et al.: Electrochemically driven formation of sponge-like porous silver nanocubes toward efficient CO<sub>2</sub> electroreduction to CO. *ChemSuschem* **13**, 2677–2683 (2020). <https://doi.org/10.1002/cssc.201903558>
119. Liu, S.B., Tao, H.B., Zeng, L., et al.: Shape-dependent electrocatalytic reduction of CO<sub>2</sub> to CO on triangular silver nanoplates. *J. Am. Chem. Soc.* **139**, 2160–2163 (2017). <https://doi.org/10.1021/jacs.6b12103>
120. Ren, W.H., Tan, X., Yang, W.F., et al.: Isolated diatomic Ni-Fe metal-nitrogen sites for synergistic electroreduction of CO<sub>2</sub>. *Angew. Chem. Int. Ed.* **58**, 6972–6976 (2019). <https://doi.org/10.1002/anie.201901575>
121. Dai, L., Qin, Q., Wang, P., et al.: Ultrastable atomic copper nanosheets for selective electrochemical reduction of carbon dioxide. *Sci. Adv.* **3**, e1701069 (2017). <https://doi.org/10.1126/sciadv.1701069>
122. Jiao, J.Q., Lin, R., Liu, S.J., et al.: Copper atom-pair catalyst anchored on alloy nanowires for selective and efficient

- electrochemical reduction of CO<sub>2</sub>. *Nat. Chem.* **11**, 222–228 (2019). <https://doi.org/10.1038/s41557-018-0201-x>
123. Rogers, C., Perkins, W.S., Veber, G., et al.: Synergistic enhancement of electrocatalytic CO<sub>2</sub> reduction with gold nanoparticles embedded in functional graphene nanoribbon composite electrodes. *J. Am. Chem. Soc.* **139**, 4052–4061 (2017). <https://doi.org/10.1021/jacs.6b12217>
124. Kim, D., Xie, C.L., Becknell, N., et al.: Electrochemical activation of CO<sub>2</sub> through atomic ordering transformations of AuCu nanoparticles. *J. Am. Chem. Soc.* **139**, 8329–8336 (2017). <https://doi.org/10.1021/jacs.7b03516>
125. Gao, D.F., Zhang, Y., Zhou, Z.W., et al.: Enhancing CO<sub>2</sub> electroreduction with the metal–oxide interface. *J. Am. Chem. Soc.* **139**, 5652–5655 (2017). <https://doi.org/10.1021/jacs.7b00102>
126. Zhang, X., Wu, Z.S., Zhang, X., et al.: Highly selective and active CO<sub>2</sub> reduction electrocatalysts based on cobalt phthalocyanine/carbon nanotube hybrid structures. *Nat. Commun.* **8**, 14675 (2017). <https://doi.org/10.1038/ncomms14675>
127. Han, N., Wang, Y., Ma, L., et al.: Supported cobalt polyphthalocyanine for high-performance electrocatalytic CO<sub>2</sub> reduction. *Chem* **3**, 652–664 (2017). <https://doi.org/10.1016/j.chempr.2017.08.002>
128. Schreier, M., Héroguel, F., Steier, L., et al.: Solar conversion of CO<sub>2</sub> to CO using earth-abundant electrocatalysts prepared by atomic layer modification of CuO. *Nat. Energy* **2**, 17087 (2017). <https://doi.org/10.1038/nenergy.2017.87>
129. Lin, S., Diercks, C.S., Zhang, Y.B., et al.: Covalent organic frameworks comprising cobalt porphyrins for catalytic CO<sub>2</sub> reduction in water. *Science* **349**, 1208–1213 (2015)
130. Kramer, W.W., McCrory, C.C.L.: Polymer coordination promotes selective CO<sub>2</sub> reduction by cobalt phthalocyanine. *Chem. Sci.* **7**, 2506–2515 (2016). <https://doi.org/10.1039/c5sc04015a>
131. Zhu, W.L., Zhang, Y.J., Zhang, H.Y., et al.: Active and selective conversion of CO<sub>2</sub> to CO on ultrathin Au nanowires. *J. Am. Chem. Soc.* **136**, 16132–16135 (2014). <https://doi.org/10.1021/ja5095099>
132. Lu, M., Zhang, M., Liu, C.G., et al.: Stable dioxin-linked metal-phthalocyanine covalent organic frameworks (COFs) as photo-coupled electrocatalysts for CO<sub>2</sub> reduction. *Angew. Chem. Int. Ed.* **60**, 4864–4871 (2021). <https://doi.org/10.1002/anie.202011722>
133. Zhang, Z., Xiao, J.P., Chen, X.J., et al.: Reaction mechanisms of well-defined metal-N<sub>4</sub> sites in electrocatalytic CO<sub>2</sub> reduction. *Angew. Chem. Int. Ed.* **57**, 16339–16342 (2018). <https://doi.org/10.1002/anie.201808593>
134. Ma, X.M., Shen, Y.L., Yao, S., et al.: Core–shell nanoporous AuCu<sub>3</sub>@Au monolithic electrode for efficient electrochemical CO<sub>2</sub> reduction. *J. Mater. Chem. A* **8**, 3344–3350 (2020). <https://doi.org/10.1039/c9ta09471g>
135. Pei, J.J., Wang, T., Sui, R., et al.: N-Bridged Co–N–Ni: new bimetallic sites for promoting electrochemical CO<sub>2</sub> reduction. *Energy Environ. Sci.* **14**, 3019–3028 (2021). <https://doi.org/10.1039/d0ee03947k>
136. Kim, M.K., Kim, H.J., Lim, H., et al.: Metal-organic framework-mediated strategy for enhanced methane production on copper nanoparticles in electrochemical CO<sub>2</sub> reduction. *Electrochim. Acta* **306**, 28–34 (2019). <https://doi.org/10.1016/j.electacta.2019.03.101>
137. Liu, S.B., Xiao, J., Lou, X.F., et al.: Efficient electrochemical reduction of CO<sub>2</sub> to HCOOH over sub-2 nm SnO<sub>2</sub> quantum wires with exposed grain boundaries. *Angew. Chem. Int. Ed.* **58**, 8499–8503 (2019). <https://doi.org/10.1002/anie.201903613>
138. Zhu, S.Q., Qin, X.P., Wang, Q., et al.: Composition-dependent CO<sub>2</sub> electrochemical reduction activity and selectivity on Au–Pd core–shell nanoparticles. *J. Mater. Chem. A* **7**, 16954–16961 (2019). <https://doi.org/10.1039/c9ta05325e>
139. Wen, G.B., Lee, D.U., Ren, B.H., et al.: Carbon dioxide electroreduction: orbital interactions in Bi–Sn bimetallic electrocatalysts for highly selective electrochemical CO<sub>2</sub> reduction toward formate production. *Adv. Energy Mater.* **8**, 1870138 (2018). <https://doi.org/10.1002/aenm.201870138>
140. Zhang, N.Q., Zhang, X.X., Kang, Y.K., et al.: A supported Pd<sub>2</sub> dual-atom site catalyst for efficient electrochemical CO<sub>2</sub> reduction. *Angew. Chem. Int. Ed.* **60**, 13388–13393 (2021). <https://doi.org/10.1002/anie.202101559>
141. Li, M.R., Tian, X.H., Garg, S., et al.: Modulated Sn oxidation states over a Cu<sub>2</sub>O-derived substrate for selective electrochemical CO<sub>2</sub> reduction. *ACS Appl. Mater. Interfaces* **12**, 22760–22770 (2020). <https://doi.org/10.1021/acsami.0c00412>
142. Yang, H.P., Wu, Y., Lin, Q., et al.: Composition tailoring via N and S co-doping and structure tuning by constructing hierarchical pores: metal-free catalysts for high-performance electrochemical reduction of CO<sub>2</sub>. *Angew. Chem. Int. Ed.* **57**, 15476–15480 (2018). <https://doi.org/10.1002/anie.201809255>
143. Sun, X.F., Lu, L., Zhu, Q.G., et al.: MoP nanoparticles supported on indium-doped porous carbon: outstanding catalysts for highly efficient CO<sub>2</sub> electroreduction. *Angew. Chem. Int. Ed.* **57**, 2427–2431 (2018). <https://doi.org/10.1002/anie.201712221>
144. Wang, H., Jia, J., Song, P.F., et al.: Efficient electrocatalytic reduction of CO<sub>2</sub> by nitrogen-doped nanoporous carbon/carbon nanotube membranes: a step towards the electrochemical CO<sub>2</sub> refinery. *Angew. Chem. Int. Ed.* **56**, 7847–7852 (2017)
145. Wang, H.X., Chen, Y.B., Hou, X.L., et al.: Nitrogen-doped graphenes as efficient electrocatalysts for the selective reduction of carbon dioxide to formate in aqueous solution. *Green Chem.* **18**, 3250–3256 (2016). <https://doi.org/10.1039/c6gc00410e>
146. Natsui, K., Iwakawa, H., Ikemiya, N., et al.: Stable and highly efficient electrochemical production of formic acid from carbon dioxide using diamond electrodes. *Angew. Chem. Int. Ed.* **57**, 2639–2643 (2018). <https://doi.org/10.1002/anie.201712271>
147. Zhang, S., Kang, P., Ubnoske, S., et al.: Polyethylenimine-enhanced electrocatalytic reduction of CO<sub>2</sub> to formate at nitrogen-doped carbon nanomaterials. *J. Am. Chem. Soc.* **136**, 7845–7848 (2014). <https://doi.org/10.1021/ja5031529>
148. Sun, X.F., Kang, X.C., Zhu, Q.G., et al.: Very highly efficient reduction of CO<sub>2</sub> to CH<sub>4</sub> using metal-free N-doped carbon electrodes. *Chem. Sci.* **7**, 2883–2887 (2016). <https://doi.org/10.1039/c5sc04158a>
149. Lu, L., Sun, X.F., Ma, J., et al.: Highly efficient electroreduction of CO<sub>2</sub> to methanol on palladium-copper bimetallic aerogels. *Angew. Chem. Int. Ed.* **57**, 14149–14153 (2018). <https://doi.org/10.1002/anie.201808964>
150. Song, Y.F., Chen, W., Zhao, C.C., et al.: Metal-free nitrogen-doped mesoporous carbon for electroreduction of CO<sub>2</sub> to ethanol. *Angew. Chem. Int. Ed.* **56**, 10840–10844 (2017). <https://doi.org/10.1002/anie.201706777>
151. Song, Y., Peng, R., Hensley, D.K., et al.: High-selectivity electrochemical conversion of CO<sub>2</sub> to ethanol using a copper nanoparticle/N-doped graphene electrode. *ChemistrySelect* **1**, 6055–6061 (2016). <https://doi.org/10.1002/slct.201601169>
152. Hoang, T.T.H., Verma, S., Ma, S.C., et al.: Nanoporous copper–silver alloys by additive-controlled electrodeposition for the selective electroreduction of CO<sub>2</sub> to ethylene and ethanol. *J. Am. Chem. Soc.* **140**, 5791–5797 (2018). <https://doi.org/10.1021/jacs.8b01868>
153. Lin, L., Liu, T.F., Xiao, J.P., et al.: Enhancing CO<sub>2</sub> electroreduction to methane with a cobalt phthalocyanine and zinc-nitrogen-carbon tandem catalyst. *Angew. Chem. Int. Ed.* **59**, 22408–22413 (2020). <https://doi.org/10.1002/anie.202009191>
154. Lin, L., Li, H.B., Yan, C.C., et al.: Synergistic catalysis over iron-nitrogen sites anchored with cobalt phthalocyanine for efficient

- CO<sub>2</sub> electroreduction. *Adv. Mater.* **31**, 1903470 (2019). <https://doi.org/10.1002/adma.201903470>
155. Dinh, C.T., Arquer, F.P.G., Sinton, D., et al.: High rate, selective, and stable electroreduction of CO<sub>2</sub> to CO in basic and neutral media. *ACS Energy Lett.* **3**, 2835–2840 (2018). <https://doi.org/10.1021/acsenenergylett.8b01734>
156. Zhao, K., Nie, X.W., Wang, H.Z., et al.: Selective electroreduction of CO<sub>2</sub> to acetone by single copper atoms anchored on N-doped porous carbon. *Nat. Commun.* **11**, 2455 (2020). <https://doi.org/10.1038/s41467-020-16381-8>
157. Xiong, W.F., Li, H.F., Wang, H.M., et al.: (2020) Hollow mesoporous carbon sphere loaded Ni-N<sub>4</sub> single-atom: support structure study for CO<sub>2</sub> electrocatalytic reduction catalyst. *Small* **16**, e2003943 (2020)
158. Zhou, Y.N., Gao, G.P., Li, Y., et al.: Transition-metal single atoms in nitrogen-doped graphenes as efficient active centers for water splitting: a theoretical study. *Phys. Chem. Chem. Phys.* **21**, 3024–3032 (2019). <https://doi.org/10.1039/c8cp06755d>
159. Wang, X.Y., Wang, Y., Sang, X.H., et al.: Dynamic activation of adsorbed intermediates via axial traction for the promoted electrochemical CO<sub>2</sub> reduction. *Angew. Chem. Int. Ed.* **60**, 4192–4198 (2021). <https://doi.org/10.1002/anie.202013427>
160. Bi, W.T., Li, X.G., You, R., et al.: Surface immobilization of transition metal ions on nitrogen-doped graphene realizing high-efficient and selective CO<sub>2</sub> reduction. *Adv. Mater.* **30**, 1706617 (2018). <https://doi.org/10.1002/adma.201706617>
161. Mohammad, A., Kibum, K., Cong, L., et al.: Nanostructured transition metal dichalcogenide electrocatalysts for CO<sub>2</sub> reduction in ionic liquid. *Science* **353**, 467–470 (2016)
162. Ju, W., Bagger, A., Hao, G.P., et al.: Understanding activity and selectivity of metal-nitrogen-doped carbon catalysts for electrochemical reduction of CO<sub>2</sub>. *Nat. Commun.* **8**, 944 (2017). <https://doi.org/10.1038/s41467-017-01035-z>
163. Otani, M., Sugino, O.: First-principles calculations of charged surfaces and interfaces: a plane-wave nonrepeated slab approach. *Phys. Rev. B* **73**, 115407 (2006). <https://doi.org/10.1103/physrevb.73.115407>
164. Peterson, A.A., Abild-Pedersen, F., Studt, F., et al.: How copper catalyzes the electroreduction of carbon dioxide into hydrocarbon fuels. *Energy Environ. Sci.* **3**, 1311–1315 (2010). <https://doi.org/10.1039/c0ee00071j>
165. Nørskov, J.K., Rossmeisl, J., Logadottir, A., et al.: Origin of the overpotential for oxygen reduction at a fuel-cell cathode. *J. Phys. Chem. B* **108**, 17886–17892 (2004). <https://doi.org/10.1021/jp047349j>
166. Chen, J.X., Chen, Y.T., Li, P., et al.: Energetic span as a rate-determining term for electrocatalytic volcanos. *ACS Catal.* **8**, 10590–10598 (2018). <https://doi.org/10.1021/acscatal.8b03008>
167. Huang, H.W., Jia, H.H., Liu, Z., et al.: Understanding of strain effects in the electrochemical reduction of CO<sub>2</sub>: using Pd nanostructures as an ideal platform. *Angew. Chem. Int. Ed.* **56**, 3594–3598 (2017). <https://doi.org/10.1002/anie.201612617>
168. Wu, J., Sharif, T., Gao, Y., et al.: Emerging carbon-based heterogeneous catalysts for electrochemical reduction of carbon dioxide into value-added chemicals. *Adv. Mater.* **31**, 1804257 (2019)
169. He, J.F., Dettelbach, K.E., Salvatore, D.A., et al.: High-throughput synthesis of mixed-metal electrocatalysts for CO<sub>2</sub> reduction. *Angew. Chem. Int. Ed.* **56**, 6068–6072 (2017). <https://doi.org/10.1002/anie.201612038>
170. Gao, C., Chen, S.M., Wang, Y., et al.: Heterogeneous single-atom catalyst for visible-light-driven high-turnover CO<sub>2</sub> reduction: the role of electron transfer. *Adv. Mater.* **30**, 1704624 (2018). <https://doi.org/10.1002/adma.201704624>
171. Hu, X.M., Rønne, M.H., Pedersen, S.U., et al.: Enhanced catalytic activity of cobalt porphyrin in CO<sub>2</sub> electroreduction upon immobilization on carbon materials. *Angew. Chem. Int. Ed.* **56**, 6468–6472 (2017). <https://doi.org/10.1002/anie.201701104>
172. Smith, P.T., Benke, B.P., Cao, Z., et al.: Iron porphyrins embedded into a supramolecular porous organic cage for electrochemical CO<sub>2</sub> reduction in water. *Angew. Chem. Int. Ed.* **57**, 9684–9688 (2018). <https://doi.org/10.1002/anie.201803873>
173. Zhu, M.H., Chen, J.C., Huang, L.B., et al.: Covalently grafting cobalt porphyrin onto carbon nanotubes for efficient CO<sub>2</sub> electroreduction. *Angew. Chem. Int. Ed.* **58**, 6595–6599 (2019)
174. Xu, S.M., Liang, X., Ren, Z.C., et al.: Free-standing air cathodes based on 3D hierarchically porous carbon membranes: kinetic overpotential of continuous macropores in Li-O<sub>2</sub> batteries. *Angew. Chem. Int. Ed.* **57**, 6825–6829 (2018). <https://doi.org/10.1002/anie.201801399>
175. Chen, S., Hossain, M.N., Chen, A.C.: Significant enhancement of the photoelectrochemical activity of CuWO<sub>4</sub> by using a cobalt phosphate nanoscale thin film. *ChemElectroChem* **5**, 523–530 (2018). <https://doi.org/10.1002/celec.201700991>
176. Hossain, M.N., Chen, S., Chen, A.C.: Fabrication and electrochemical study of ruthenium-ruthenium oxide/activated carbon nanocomposites for enhanced energy storage. *J. Alloy. Compd.* **751**, 138–147 (2018). <https://doi.org/10.1016/j.jallcom.2018.04.104>
177. Sassone, D., Zeng, J.Q., Fontana, M., et al.: Polymer-metal complexes as emerging catalysts for electrochemical reduction of carbon dioxide. *J. Appl. Electrochem.* **51**, 1301–1311 (2021)
178. Qiao, B.T., Wang, A.Q., Yang, X.F., et al.: Single-atom catalysis of CO oxidation using Pt<sub>1</sub>/FeO<sub>x</sub>. *Nat. Chem.* **3**, 634–641 (2011). <https://doi.org/10.1038/nchem.1095>
179. Ding, K., Gulec, A., Johnson, A.M., et al.: Identification of active sites in CO oxidation and water-gas shift over supported Pt catalysts. *Science* **350**, 189–192 (2015)
180. Han, Y.H., Wang, Y.G., Chen, W.X., et al.: Hollow N-doped carbon spheres with isolated cobalt single atomic sites: superior electrocatalysts for oxygen reduction. *J. Am. Chem. Soc.* **139**, 17269–17272 (2017). <https://doi.org/10.1021/jacs.7b10194>
181. Zhu, Y.Q., Sun, W.M., Chen, W.X., et al.: Scale-up biomass pathway to cobalt single-site catalysts anchored on N-doped porous carbon nanobelt with ultrahigh surface area. *Adv. Funct. Mater.* **28**, 1802167 (2018). <https://doi.org/10.1002/adfm.201802167>
182. Han, Y.H., Wang, Z.Y., Xu, R.R., et al.: Ordered porous nitrogen-doped carbon matrix with atomically dispersed cobalt sites as an efficient catalyst for dehydrogenation and transfer hydrogenation of N-heterocycles. *Angew. Chem. Int. Ed.* **57**, 11262–11266 (2018). <https://doi.org/10.1002/anie.201805467>
183. Hossain, M.N., Wen, J.L., Chen, A.C.: Unique copper and reduced graphene oxide nanocomposite toward the efficient electrochemical reduction of carbon dioxide. *Sci. Rep.* **7**, 3184 (2017). <https://doi.org/10.1038/s41598-017-03601-3>
184. Albo, J., Vallejo, D., Beobide, G., et al.: Copper-based metal-organic porous materials for CO<sub>2</sub> electrocatalytic reduction to alcohols. *Chemsuschem* **10**, 1100–1109 (2017). <https://doi.org/10.1002/cssc.201600693>
185. Albo, J., Alvarez-Guerra, M., Castaño, P., et al.: Towards the electrochemical conversion of carbon dioxide into methanol. *Green Chem.* **17**, 2304–2324 (2015). <https://doi.org/10.1039/c4gc02453b>
186. Hossain, M.N., Ahmad, S., Silva, I.S., et al.: Electrochemical reduction of CO<sub>2</sub> at coinage metal nanodendrites in aqueous ethanalamine. *Chem. Eur. J.* **27**, 1346–1355 (2021). <https://doi.org/10.1002/chem.202003039>
187. Keerthiga, G., Viswanathan, B., Chetty, R.: Electrochemical reduction of CO<sub>2</sub> on electrodeposited Cu electrodes crystalline phase sensitivity on selectivity. *Catal. Today* **245**, 68–73 (2015). <https://doi.org/10.1016/j.cattod.2014.08.008>

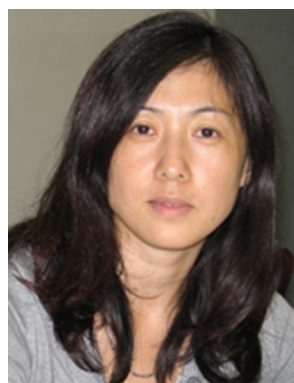


188. Zhai, Q.G., Xie, S.J., Fan, W.Q., et al.: Photocatalytic conversion of carbon dioxide with water into methane: platinum and copper(I) oxide co-catalysts with a core-shell structure. *Angew. Chem.* **125**, 5888–5891 (2013). <https://doi.org/10.1002/ange.201301473>
189. Manthiram, K., Beberwyck, B.J., Alivisatos, A.P.: Enhanced electrochemical methanation of carbon dioxide with a dispersible nanoscale copper catalyst. *J. Am. Chem. Soc.* **136**, 13319–13325 (2014). <https://doi.org/10.1021/ja5065284>
190. Xie, J.F., Huang, Y.X., Li, W.W., et al.: Efficient electrochemical CO<sub>2</sub> reduction on a unique chrysanthemum-like Cu nanoflower electrode and direct observation of carbon deposit. *Electrochim. Acta* **139**, 137–144 (2014). <https://doi.org/10.1016/j.electacta.2014.06.034>
191. Kim, D., Resasco, J., Yu, Y., et al.: Synergistic geometric and electronic effects for electrochemical reduction of carbon dioxide using gold-copper bimetallic nanoparticles. *Nat. Commun.* **5**, 4948 (2014). <https://doi.org/10.1038/ncomms5948>
192. Li, F., Han, G.F., Noh, H.J., et al.: Boosting oxygen reduction catalysis with abundant copper single atom active sites. *Energy Environ. Sci.* **11**, 2263–2269 (2018). <https://doi.org/10.1039/c8ee01169a>
193. Qu, Y.T., Li, Z.J., Chen, W.X., et al.: Direct transformation of bulk copper into copper single sites via emitting and trapping of atoms. *Nat. Catal.* **1**, 781–786 (2018). <https://doi.org/10.1038/s41929-018-0146-x>
194. Andronesco, C., Barwe, S., Ventosa, E., et al.: Powder catalyst fixation for post-electrolysis structural characterization of NiFe layered double hydroxide based oxygen evolution reaction electrocatalysts. *Angew. Chem. Int. Ed.* **56**, 11258–11262 (2017). <https://doi.org/10.1002/anie.201705385>
195. Liu, K., Smith, W.A., Burdyny, T.: Introductory guide to assembling and operating gas diffusion electrodes for electrochemical CO<sub>2</sub> reduction. *ACS Energy Lett.* **4**, 639–643 (2019). <https://doi.org/10.1021/acsenerylett.9b00137>
196. Burdyny, T., Smith, W.A.: CO<sub>2</sub> reduction on gas-diffusion electrodes and why catalytic performance must be assessed at commercially-relevant conditions. *Energy Environ. Sci.* **12**, 1442–1453 (2019). <https://doi.org/10.1039/c8ee03134g>
197. Ren, S., Joulie, D., Salvatore, D., et al.: Molecular electrocatalysts can mediate fast, selective CO<sub>2</sub> reduction in a flow cell. *Science* **365**, 367–369 (2019)
198. Jiang, K., Siahrostami, S., Akey, A.J., et al.: Transition-metal single atoms in a graphene shell as active centers for highly efficient artificial photosynthesis. *Chem* **3**, 950–960 (2017). <https://doi.org/10.1016/j.chempr.2017.09.014>
199. Back, S., Lim, J., Kim, N.Y., et al.: Single-atom catalysts for CO<sub>2</sub> electroreduction with significant activity and selectivity improvements. *Chem. Sci.* **8**, 1090–1096 (2017). <https://doi.org/10.1039/c6sc03911a>
200. Benson, E.E., Kubiak, C.P., Sathrum, A.J., et al.: Electrocatalytic and homogeneous approaches to conversion of CO<sub>2</sub> to liquid fuels. *Chem. Soc. Rev.* **38**, 89–99 (2009). <https://doi.org/10.1039/b804323j>
201. Choi, J., Kim, J., Wagner, P., et al.: Energy efficient electrochemical reduction of CO<sub>2</sub> to CO using a three-dimensional porphyrin/graphene hydrogel. *Energy Environ. Sci.* **12**, 747–755 (2019). <https://doi.org/10.1039/c8ee03403f>
202. Fan, Q., Zhang, M.L., Jia, M.W., et al.: Electrochemical CO<sub>2</sub> reduction to C<sub>2+</sub> species: heterogeneous electrocatalysts, reaction pathways, and optimization strategies. *Mater. Today Energy* **10**, 280–301 (2018). <https://doi.org/10.1016/j.mtener.2018.10.003>
203. Jiang, K., Sandberg, R.B., Akey, A.J., et al.: Metal ion cycling of Cu foil for selective C-C coupling in electrochemical CO<sub>2</sub> reduction. *Nat. Catal.* **1**, 111–119 (2018). <https://doi.org/10.1038/s41929-017-0009-x>
204. Huang, J.F., Mensi, M., Oveisi, E., et al.: Structural sensitivities in bimetallic catalysts for electrochemical CO<sub>2</sub> reduction revealed by Ag-Cu nanodimers. *J. Am. Chem. Soc.* **141**, 2490–2499 (2019). <https://doi.org/10.1021/jacs.8b12381>
205. Sung, S., Li, X.H., Wolf, L.M., et al.: Synergistic effects of imidazolium-functionalization on fac-Mn(CO)<sub>3</sub> bipyridine catalyst platforms for electrocatalytic carbon dioxide reduction. *J. Am. Chem. Soc.* **141**, 6569–6582 (2019). <https://doi.org/10.1021/jacs.8b13657>
206. Sanchez, F., Motta, D., Roldan, A., et al.: Hydrogen generation from additive-free formic acid decomposition under mild conditions by Pd/C: experimental and DFT studies. *Top. Catal.* **61**, 254–266 (2018). <https://doi.org/10.1007/s11244-018-0894-5>
207. Lei, Y.P., Wang, Y.C., Liu, Y., et al.: Designing atomic active centers for hydrogen evolution electrocatalysts. *Angew. Chem. Int. Ed.* **59**, 20794–20812 (2020). <https://doi.org/10.1002/anie.201914647>
208. Liu, X.Y., Xiao, J.P., Peng, H.J., et al.: Understanding trends in electrochemical carbon dioxide reduction rates. *Nat. Commun.* **8**, 15438 (2017). <https://doi.org/10.1038/ncomms15438>
209. Guo, Y.B., Yao, S., Xue, Y.Y., et al.: Nickel single-atom catalysts intrinsically promoted by fast pyrolysis for selective electroreduction of CO<sub>2</sub> into CO. *Appl. Catal. B Environ.* **304**, 120997 (2022). <https://doi.org/10.1016/j.apcatb.2021.120997>
210. Wu, J.J., Ma, S.C., Sun, J., et al.: A metal-free electrocatalyst for carbon dioxide reduction to multi-carbon hydrocarbons and oxygenates. *Nat. Commun.* **7**, 13869 (2016). <https://doi.org/10.1038/ncomms13869>
211. Jiao, Y., Zheng, Y., Chen, P., et al.: Molecular scaffolding strategy with synergistic active centers to facilitate electrocatalytic CO<sub>2</sub> reduction to hydrocarbon/alcohol. *J. Am. Chem. Soc.* **139**, 18093–18100 (2017). <https://doi.org/10.1021/jacs.7b10817>
212. Di, J., Chen, C., Yang, S.Z., et al.: Isolated single atom cobalt in Bi<sub>2</sub>O<sub>4</sub>Br atomic layers to trigger efficient CO<sub>2</sub> photoreduction. *Nat. Commun.* **10**, 2840 (2019). <https://doi.org/10.1038/s41467-019-10392-w>
213. Xie, J.F., Zhao, X.T., Wu, M.X., et al.: Inside back cover: metal-free fluorine-doped carbon electrocatalyst for CO<sub>2</sub> reduction outcompeting hydrogen evolution. *Angew. Chem. Int. Ed.* **57**, 9981–9981 (2018). <https://doi.org/10.1002/anie.201805218>
214. Favaro, M., Xiao, H., Cheng, T., et al.: Subsurface oxide plays a critical role in CO<sub>2</sub> activation by Cu(111) surfaces to form chemisorbed CO<sub>2</sub>, the first step in reduction of CO<sub>2</sub>. *Proc. Natl. Acad. Sci.* **114**, 6706–6711 (2017). <https://doi.org/10.1073/pnas.1701405114>
215. Nie, X.W., Esopi, M.R., Janik, M.J., et al.: Selectivity of CO<sub>2</sub> reduction on copper electrodes: the role of the kinetics of elementary steps. *Angew. Chem. Int. Ed.* **52**, 2459–2462 (2013). <https://doi.org/10.1002/anie.201208320>
216. Nie, X.W., Luo, W.J., Janik, M.J., et al.: Reaction mechanisms of CO<sub>2</sub> electrochemical reduction on Cu(111) determined with density functional theory. *J. Catal.* **312**, 108–122 (2014). <https://doi.org/10.1016/j.jcat.2014.01.013>
217. Greiner, M.T., Jones, T.E., Beeg, S., et al.: Free-atom-like d states in single-atom alloy catalysts. *Nat. Chem.* **10**, 1008–1015 (2018). <https://doi.org/10.1038/s41557-018-0125-5>
218. Ren, D., Deng, Y.L., Handoko, A.D., et al.: Selective electrochemical reduction of carbon dioxide to ethylene and ethanol on copper(I) oxide catalysts. *ACS Catal.* **5**, 2814–2821 (2015). <https://doi.org/10.1021/cs502128q>
219. Handoko, A.D., Chan, K.W., Yeo, B.S.: –CH<sub>3</sub> mediated pathway for the electroreduction of CO<sub>2</sub> to ethane and ethanol on thick oxide-derived copper catalysts at low overpotentials. *ACS Energy Lett.* **2**, 2103–2109 (2017). <https://doi.org/10.1021/acsenerylett.7b00514>

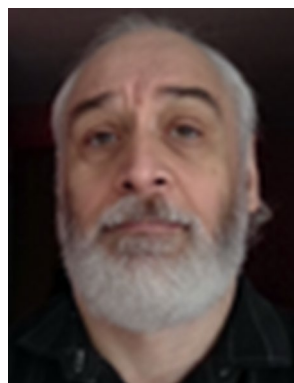
220. Lee, S., Park, G., Lee, J.: Importance of Ag-Cu biphasic boundaries for selective electrochemical reduction of CO<sub>2</sub> to ethanol. *ACS Catal.* **7**, 8594–8604 (2017). <https://doi.org/10.1021/acscatal.7b02822>
221. Hori, Y., Takahashi, I., Koga, O., et al.: Selective formation of C<sub>2</sub> compounds from electrochemical reduction of CO<sub>2</sub> at a series of copper single crystal electrodes. *J. Phys. Chem. B* **106**, 15–17 (2002). <https://doi.org/10.1021/jp013478d>
222. Zou, X.L., Liu, M.J., Wu, J.J., et al.: How nitrogen-doped graphene quantum dots catalyze electroreduction of CO<sub>2</sub> to hydrocarbons and oxygenates. *ACS Catal.* **7**, 6245–6250 (2017). <https://doi.org/10.1021/acscatal.7b01839>
223. Duan, X.C., Xu, J.T., Wei, Z.X., et al.: Metal-free carbon materials for CO<sub>2</sub> electrochemical reduction. *Adv. Mater.* **29**, 1701784–1701803 (2017). <https://doi.org/10.1002/adma.201701784>
224. Gao, D.F., Zhou, H., Wang, J., et al.: Size-dependent electrocatalytic reduction of CO<sub>2</sub> over Pd nanoparticles. *J. Am. Chem. Soc.* **137**, 4288–4291 (2015). <https://doi.org/10.1021/jacs.5b00046>
225. Gattrell, M., Gupta, N., Co, A.: A review of the aqueous electrochemical reduction of CO<sub>2</sub> to hydrocarbons at copper. *J. Electroanal. Chem.* **594**, 1–19 (2006). <https://doi.org/10.1016/j.jelechem.2006.05.013>
226. Kuhl, K.P., Hatsukade, T., Cave, E.R., et al.: Electrocatalytic conversion of carbon dioxide to methane and methanol on transition metal surfaces. *J. Am. Chem. Soc.* **136**, 14107–14113 (2014). <https://doi.org/10.1021/ja505791r>
227. Zhou, Y.S., Che, F.L., Liu, M., et al.: Dopant-induced electron localization drives CO<sub>2</sub> reduction to C<sub>2</sub> hydrocarbons. *Nat. Chem.* **10**, 974–980 (2018). <https://doi.org/10.1038/s41557-018-0092-x>
228. Wang, J., Zheng, M.Y., Zhao, X., et al.: Structure-performance descriptors and the role of the axial oxygen atom on M-N<sub>4</sub>-C single-atom catalysts for electrochemical CO<sub>2</sub> reduction. *ACS Catal.* **12**, 5441–5454 (2022). <https://doi.org/10.1021/acscatal.2c00429>
229. Peterson, A.A., Nørskov, J.K.: Activity descriptors for CO<sub>2</sub> electroreduction to methane on transition-metal catalysts. *J. Phys. Chem. Lett.* **3**, 251–258 (2012). <https://doi.org/10.1021/jz201461p>
230. Cao, H., Zhang, Z.S., Chen, J.W., et al.: Potential-dependent free energy relationship in interpreting the electrochemical performance of CO<sub>2</sub> reduction on single atom catalysts. *ACS Catal.* **12**, 6606–6617 (2022). <https://doi.org/10.1021/acscatal.2c01470>
231. Lum, Y., Ager, J.W.: Evidence for product-specific active sites on oxide-derived Cu catalysts for electrochemical CO<sub>2</sub> reduction. *Nat. Catal.* **2**, 86–93 (2018). <https://doi.org/10.1038/s41929-018-0201-7>
232. Morales-Guio, C.G., Cave, E.R., Nitopi, S.A., et al.: Improved CO<sub>2</sub> reduction activity towards C<sub>2+</sub> alcohols on a tandem gold on copper electrocatalyst. *Nat. Catal.* **1**, 764–771 (2018). <https://doi.org/10.1038/s41929-018-0139-9>
233. Zhao, Z.L., Lu, G.: Cu-based single-atom catalysts boost electroreduction of CO<sub>2</sub> to CH<sub>3</sub>OH: first-principles predictions. *J. Phys. Chem. C* **123**, 4380–4387 (2019). <https://doi.org/10.1021/acs.jpcc.8b12449>
234. Wang, Y.F., Chen, Z., Han, P., et al.: Single-atomic Cu with multiple oxygen vacancies on ceria for electrocatalytic CO<sub>2</sub> reduction to CH<sub>4</sub>. *ACS Catal.* **8**, 7113–7119 (2018). <https://doi.org/10.1021/acscatal.8b01014>
235. Cheng, M.J., Clark, E.L., Pham, H.H., et al.: Quantum mechanical screening of single-atom bimetallic alloys for the selective reduction of CO<sub>2</sub> to C<sub>1</sub> hydrocarbons. *ACS Catal.* **6**, 7769–7777 (2016). <https://doi.org/10.1021/acscatal.6b01393>



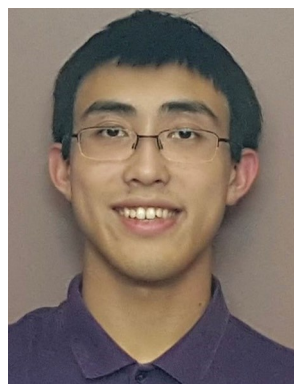
**M. Nur Hossain** is a Postdoctoral Fellow of the National Research Council Canada. He earned his Ph.D. degree in chemistry and materials science from Lakehead University in 2018. Nur's research interests span the areas of electrochemistry, catalysis, materials science and nanotechnology.



**Lei Zhang** is a Senior Research Officer at the National Research Council Canada. Lei's main research interests include electrocatalysis, nanostructured catalysts and electrode materials for energy conversion and storage, including PEM fuel cells, supercapacitors, batteries and CO<sub>2</sub> reduction to valuable chemicals and fuels. She is a Fellow of the Royal Society of Chemistry (FRSC).



**Roberto Neagu** is a senior researcher with the National Research Council of Canada's Energy, Mining and Environment Research Centre in Vancouver, British Columbia. He has an MSc degree in chemical processes engineering from the Polytechnic University of Bucharest and a Ph.D. degree in electrochemistry from the National Polytechnic Institute in Grenoble. He works on additive manufacturing of electrochemical devices and leads the redox flow battery development at NRC.



**Enoch Rassachack** is a student at the University of British Columbia currently studying for his BSc degree in Honours Chemistry. He worked on CO<sub>2</sub>RR single-atom catalyst electrode synthesis as an intern at the National Research Council Canada in the winter term of 2022.